EFFECT OF NON-EQUILIBRIUM PROCESSING CONDITIONS ON THE

MICROSTRUCTURAL AND PHYSICAL PROPERTIES

OF ADVANCED MATERIALS

by

Madelyn Fabiola Madrigal Camacho

A thesis submitted to the Faculty and the Board of Trustees of the Colorado School of Mines in partial fulfillment of the requirements for the degree of Doctor of Philosophy (Metallurgical and Materials Engineering).

Golden, Colorado

Date _____

Signed: _____

_____
Madelyn Fabiola Madrigal Camacho

Signed: _____

_____
Dr. Suveen N. Mathaudhu
Thesis Advisor

Golden, Colorado

Date _____

Signed: _____

_____
Dr. Ivar Reimanis
Professor and Department Head
Metallurgical and Materials Engineering

ABSTRACT

It is now well recognized that the structure and constitution of advanced materials can be better controlled by processing them under non-equilibrium conditions that result in non-equilibrium, persistently metastable states. These methods include rapid solidification, condensation, irradiation, and mechanical cold working. These methods allow for the formation of fine-grained structures, metastable phases, and solid-state reactions that would be otherwise inaccessible by equilibrium processing conditions. By harnessing non-equilibrium process conditions, metallurgists can push the boundaries of materials science, enabling the development of advanced alloys with superior mechanical performance.

Nevertheless, non-equilibrium process conditions in physical metallurgy pose several significant challenges to understanding and predicting complex microstructural evolution. Additionally, advanced experimental techniques and theoretical models are required to characterize and control these processes. Based on these knowledge gaps, this work focused on the revealing of processing-structure-properties-performance interrelationships of three non-equilibrium processing conditions: mechanical alloying, laser ablation, and laser melting. Each technique was evaluated with different material systems. In the case of mechanical alloying, MoC-graphite composite and CoCr-based alloy were synthesized. For laser ablation, MoC-graphite core-shell nanoparticles were studied. Lastly, for laser melting, CoCr-based alloys and 316 L stainless steel alloy were 3D printed. Although no in situ experiments were performed, several characterization techniques were implemented to analyze the materials.

The study of these three techniques was aimed at understanding the energization and recovery mechanisms responsible for the solidification, nucleation, grain growth, defect formation, crystallography, and composition of the materials. The parameters of each process were thoroughly explored to develop a more comprehensive knowledge of material-process correlations. Other contributions of these studies are the synthesis of complex carbide heterostructures, alternatives for powder feedstock production for selective laser additive manufacturing (SLM), microstructure control for SLM, and new insights into power reusability for powder bed fusion-laser bed (PBF-LB) processes.

TABLE OF CONTENTS

LIST OF FIGURES

ix

LIST OF TABLES

LIST OF SYMBOLS

Ambient temperature…………………………………………………………….	T_0
Average particle spacing…………………………………………………………	λ_p
Burger's vector………………………………………………………………...	b
Bragg angle……………………………………………………………………	θ_B
Contrast factor……………………………………………………………….....	$\bar{C}$
Contrast factors………………………………………………………………....	C
Crystallite size……………………………………………………………….....	D
Crystallite strain………………………………………………………………..	β_{strain}
Dislocation density……………………………………………………………..	ρ
Dislocation strengthening………………………………………………………..	σ_ρ
Electron temperature……………………………………………………….......…	T_e
Equilibrium temperature………………………………………………………....	T_E
Front Velocity…………………………………………………………………	V
Grain boundary strengthening……………………………………………………	σ_{GB}
Grain size………………………………………………………........................…	d
HAGBs fraction…………………………………………………………………	X_{HAGBs}
LAGBs fraction……………………………………………………….…………	X_{LAGBs}
Lattice constant………………………………………………………………..	α
Lattice temperature……………………………………………………….………	T_i
Mean Orientation factor……………………………………………………….…	M
Mean radius of inclusions………………………………………………………....	r
Nucleation temperature…………………………………………………………	Tn
Particle strengthening…………………………………………………………..	σ_P
Poisson ratio…………………………………………………………………....	ν
Restriction factor………………………………………………………………	Q
Shear modulus…………………………………………………………………	G
Solid solution strengthening……………………………………………………....	σ_{SS}
Strengthening coefficient………………………………………………….……...	K
Thermal gradient………………………………………………………………	G
Volume fraction……………………………………………………………….	f
Wavelength……………………………………………………………………..	λ

LIST OF ABBREVIATIONS

Additive manufacturing…………………………………………………… AM

Atomic emission spectroscopy………………………………………….. AES

Constitutional supercooling…………………………………………….. CS

Continuous wavelength…………………………………………….. CW

Direct energy deposition………………………………………………... DED

Electron backscatter diffraction system……………………………………… EBSD

End of life of powder…………………………………………………… EoL

Energy dispersive X-ray spectroscopy………………………………………… EDS

Face centered cubic………………………………………………….. FCC

Femtosecond…………………………………………………….. fs

Focused ion beam…………………………………………………… FIB

Hexagonal close-packed…………………………………………………… HCP

High angle grain boundaries……………………………………………….. HAGBs

High carbon…………………………………………………... HC

High resolution transmission electron microscopy……………………………... HRTEM

Laser ablation in liquid……………………………………………………… LAL

Low angle grain boundaries………………………………………………… LAGBs

Low carbon…………………………………………………………... LC

Modified Williamson-Hall……………………………………………… mW-H

Nanoparticles………………………………………………………….. NPs

Nucleation-free zone………………………………………………………. NFZ

Onion-like carbon………………………………………………………. OLC

Particle control agent…………………………………………………… PCA

Particle size distribution……………………...…………………………… PSD

Picosecond……………………………………………………………… ps

Powder bed fusion-laser bed…..………………………………………... PBF-LB

Scanning electron microscopy……………………………………………… SEM

Selective laser additive manufacturing…………………………………………… SLM

Spark plasma sintering…………………………………………………… SPS

Stacking fault probability………………………………………………… SFP

Stacking faults…………………………………………………... SFs

Stainless steel……………………………………………………… SS

ACKNOWLEDGMENTS

CHAPTER 1   INTRODUCTION

Non-equilibrium processing conditions play a pivotal role in metallurgy by enabling the manipulation and optimization of material properties beyond what is achievable through conditions resulting in microstructural equilibrium. These processing conditions can be defined as systems that are not in mechanical or thermal equilibrium with their surroundings. Some of the techniques in this area include mechanical alloying (ball milling), rapid solidification, laser processing, plasma processing, spray forming, physical and chemical vapor deposition, and ion mixing.

It is well recognized that the structure and constitution of advanced materials can be better controlled by modifying the conditions that bring them in and out of equilibrium [1]. These conditions involve a range of complex physical phenomena and interactions, mainly because they are part of an inherently interdisciplinary field that includes physics, mathematics, thermodynamics, kinetics, and chemistry. This results in several challenges in the research field. For example, understanding the complex kinetics and mechanisms involved in non-equilibrium transformations is inherently difficult. The rapid nature of these processes makes it challenging to capture and analyze the dynamic changes occurring at the atomic and microstructural levels. Additionally, the lack of thermodynamic equilibrium makes predicting and controlling the resulting material properties more challenging. The intricate interplay between processing parameters, such as cooling rates, alloy composition, and deformation conditions, adds further complexity to the experimental and computational investigations. Moreover, developing robust and scalable processing techniques for achieving non-equilibrium states in large-scale industrial settings remains a significant challenge. Overcoming these hurdles requires interdisciplinary collaborations, advanced characterization techniques, and innovative approaches to modeling and simulation, ultimately paving the way for the utilization of non-equilibrium processes in producing advanced metallurgical materials.

To address these challenges, several authors have explained the main governing mechanisms based on thermodynamic forces, the kinetics of phase transformations, the kinetics of defects, and diffusion [1-5]. However, the approach developed by Turnbull [6] addressed these mechanisms more broadly and can be applied to any non-equilibrium process.

In the 80s, Turnbull presented that the principal purpose of all these techniques is to synthesize a material by energizing it (taking it out of equilibrium) and then quenching it (obtention of a configurationally frozen state). Energization can take place due to external forces, including heating (phase change can occur), pressure, irradiation, plastic deformation, and evaporation. When the material is quenched, this experiences a restoration of local equilibrium. An intermediate metastable state is attained; however, it can evolve into a desired microstructure or chemical composition after post-

processing. The energization and the restoration of local equilibrium resulting from all these non-equilibrium processes can be achieved by manipulating cooling rates, deformation techniques, and processing parameters. This will further enable better control in the obtainment of nanocrystalline, ultrafine-grain, or metastable states.

This approach was selected for this dissertation to explain the three techniques under investigation, *mechanical alloying* and laser processes, including *laser ablation* and *laser melting*. In this work, the distinctive operational mechanisms for each method were evaluated to describe the driving forces to achieve the energization and quenching steps.

When evaluating these processes individually, ball milling stands out because it allows the development of new alloys and composites, as almost any composition of powder mixtures can be mechanically activated to induce mechanochemical reactions. Additionally, other attributes correspond to the production of second phases, grain size refinement, synthesis of metastable phases, and scale-up powder production. On the other hand, laser ablation in liquid and solid is a powerful technique for producing nanoparticles (NPs) or thin films. For the synthesis of NPs, this technique provides high production rates, high purity, suitable particle size distribution, and, most importantly, has the power to achieve complex chemical reactions due to its high temperature and pressure conditions. Beyond the nanoscale, laser melting is a process leading the laser additive manufacturing field to produce micro and macro components. These laser processes allow studying complex processing-structure-properties relationships of various alloy systems.

More fundamental research is needed to predict and control these non-equilibrium process conditions. We have therefore selected systematic studies to generate fundamental relationships on how specific operating parameters of each technique contribute to synthesizing new materials and lead to microstructure evolution, defect formation, solidification behavior, changes in properties, and mechanical behavior.

1.1   Research objectives

The following sections of this dissertation detail the processing-structure-properties-performance relationships of three processes that have non-equilibrium conditions: mechanical alloying, laser ablation, and laser melting. The feasibility of each technique to synthesize alloys and composites that conventional methods cannot obtain is explored.

Three studies were included as written for publication that, together, address the following objectives:

1. Develop an understanding of the distinctive operational mechanisms that cause materials to depart from and restore their equilibrium during mechanical alloying, laser ablation, and laser melting processes.

2. Evaluate the effect of process parameters on the microstructural evolution of materials synthesized by mechanical alloying, laser ablation, and laser melting processes.

   Moreover, the specific objectives of each study are the following:

   MoC@C core-shell nanoparticles synthesized by laser ablation in liquid.

1. Investigate the effect of pulse duration and irradiation on the synthesis of MoC core-shell nanoparticles.

2. Determine the influence of multistep laser ablation on the resultant microstructure and composition of the carbide nanoparticles.

   Effect of processing, chemical composition, and annealing temperature on the mechanochemical synthesis of Mo_xC-graphite composite.

1. Investigate the effect of ball milling parameters on the microstructure, particle size, and composition of the Mo_xC-graphite composite.

2. Study the evolution of the microstructure and composition of the composite when using different graphite molar content and annealing temperatures.

   CoCr alloy processed by selective laser melting: comparison of atomized and milled powder feedstocks.

1. Evaluate the effect of continuous and pulsed lasers in the melting behavior of CoCr-based alloys for additive manufacturing processes.

2. Study mechanical alloying as an alternative for powder feedstock production for selective laser melting processes.

3. Determine if adding nanoparticles can induce heterogeneous nucleation and facilitate equiaxed grain growth for selective laser melting processes.

   Elucidating the effect of powder reusability of 316L stainless steel on the as-printed parts for laser.

1. Evaluate the evolution of particle size distribution, crystallography, composition, and microstructure of powder as a function of the number of reuses.

2. Determine the primary source of anomalies in reused 316L stainless steel powder that contribute to changes in the microstructure and tensile properties of the 3D printed components.

1.2 Proposed materials and techniques

The following chapters include laser ablation, mechanical alloying, and laser melting as single study subjects. Each method has distinctive operational mechanisms that are similar to methods for the rapid synthesis of various materials families such as ceramics, alloys, and metal or ceramic matrix composites.

In the case of laser ablation, we reported a controllable synthesis of a heterophase of molybdenum carbide with graphite obtaining an MoC-graphite nanocomposite. The interest in studying this carbide has recently grown due to its catalytic properties similar to noble metals in many organic chemical reactions. However, its synthesis is challenging as high temperatures, and high purity is required. Laser ablation was demonstrated to be a powerful technique to synthesize these complex structures, and in only two steps, a molybdenum carbide coated with graphitic layers was formed. With this processing method, 1) each parameter can be controlled independently, 2) there is no need to add surfactants or binders to stabilize the nanoparticles, 3) low reactions times are possible due to its high temperature and pressure conditions, and 4) high purity of NPs and low chemical waste are possible. Our approach evaluated the effect of pulse duration, beam diameter, power, frequency, solvents, and the gas medium to understand the fundamental laser-matter relationships of this non-equilibrium technique that led to the formation of stable NPs. This further explains the importance of laser ablation, its dominating mechanisms, and issues. This work can lead to functional guidance for the future design and fabrication of innovative nanomaterials for advanced catalysis applications and beyond. This topic will be covered in more detail in Chapter 3.

The projects involving mechanical alloying were focused on the synthesis of two systems 1) MoC-graphite composites and 2) CoCr+X (X=SiC or WC) alloy powders. The first system (covered in Chapter 4) was developed to scale-up the exact composition of powders synthesized by laser ablation. The second system (covered in Chapter 5) was inspired by the need to develop alloys for laser additive manufacturing that can achieve crack-free, fine-grained, and equiaxed microstructures. Mechanical alloying is a viable alternative to overcome the challenge of synthesizing metal carbides and adding a second phase in a metallic or ceramic matrix. Despite being a well-known process, simultaneous progress in fundamental science and optimization of the process variables is still needed. Mechanical alloying involves optimizing several variables to achieve the desired microstructures and composition. Therefore, several operating parameters were used in this study (milling time, type of mill, milling container, speed, ball-to-powder weight ratio, temperature, and particle control agent) to achieve the desired materials. By refining the

process parameters, we could investigate their effect on the morphology, microstructure, composition, and in the case of the second system, its consequent properties after laser melting.

Laser additive manufacturing was previously mentioned as an application that uses CoCr powders system, therefore laser melting is the non-equilibrium technique investigated. The material systems studied correspond to 1) CoCr+X (X=SiC or WC) and 2) 316L stainless steel powders. Both topics will be covered in Chapter 5 and Chapter 6, respectively. For the former system, various laser techniques were studied to determine the effect of laser type and parameters on the final microstructure, density, and composition of the printed parts. With the second system, only one laser source was used, and the powder feedstock changes were the object of study. Research and industry are mainly focused on the optimization of process parameters, the design of printable alloys, and the achieved properties. In this investigation, we contributed to each of these areas of study in different ways. In the case of CoCr alloy, we developed a laboratory-scale system to predominantly study the fundamentals of laser melting. However, in the case of 316L stainless steel, we scaled up the study by using an industrial 3D printer that allowed us to evaluate the impact of the powder and process conditions on the properties and mechanical performance of the parts. In both selected material studies, the melting modes were considered to explain the printed materials' composition, microstructure, defects, and properties.

1.3   References

1. Baricco, M. (1995) Key Engineering Materials, 103, 1

2. Cahn, R. (1999). Non-equilibrium Processing of Materials (Vol. 2). (C. Suryanarayana, Ed.) Pergamon Materials Series

3. Lorazo, P., Lewis, L. J., & Meunier, M. (2006). Thermodynamic pathways to melting, ablation, and solidification in absorbing solids under pulsed laser irradiation. Physical Review B - Condensed Matter and Materials Physics, 73(13), 1–22. https://doi.org/10.1103/PhysRevB.73.134108

4. Suryanarayana, C. (2001). Mechanical alloying and milling. Progress in Materials Science, 46(1–2), 1–184. https://doi.org/10.1016/S0079-6425(99)00010-9

5. National Academies of Sciences, Engineering, and Medicine. (1999). Condensed-Matter and Materials Physics: Basic Research for Tomorrow's Technology. Washington, DC: The National Academies Press. https://doi.org/10.17226/6407.

6. Turnbull, D. (1981) Metastable structures in metallurgy. Metallurgical Transactions B, 12 A, 695–708

CHAPTER 2   BACKGROUND

2.1   Non-equilibrium processing of materials

Non-equilibrium processes conditions play a crucial role in physical metallurgy, as they govern the microstructural evolution and properties of metallic materials. These processing conditions occur when materials are subjected to external forces, such as temperature gradients, mechanical deformation, rapid solidification, and phase transformations. Understanding and controlling non-equilibrium phenomena are essential for tailoring material properties to meet specific industrial requirements. The most studied non-equilibrium techniques are rapid solidification, phase transformations, laser processes, mechanical alloying, solid-state amorphization, and severe plastic deformation [1].

Only two techniques mentioned above were selected for this work: *mechanical alloying* and laser processing, including *laser ablation* and *laser melting*. Each of these methods has distinctive operational mechanisms which require different energies to achieve the energization and quenching steps. For the three processing approaches selected, mechanical alloying has the largest departure from equilibrium compared to the laser processes, showing great potential in developing non-equilibrium materials [1,2].

The calculations of the energetic states in each process are out of scope for this dissertation, however, the fundamental mechanisms governing each method are discussed to reveal the main physical phenomena and interactions. Some of the critical mechanisms subjected to non-equilibrium conditions that will be covered in the following sections are:

1. Diffusion: this is the process of atomic or molecular species moving through a material. It plays a central role in non-equilibrium processes by facilitating mass transport and influencing the evolution of microstructures. Non-equilibrium conditions, such as rapid cooling or high deformation rates, can affect diffusion kinetics and lead to deviations from equilibrium diffusion paths, resulting in unique microstructural features and non-equilibrium phase transformations.

2. Nucleation and growth: Nucleation is the formation of small, stable clusters of atoms or molecules that act as the building blocks for new phases or microstructural features. In non-equilibrium processing, the nucleation and growth of phases occur under conditions that deviate from equilibrium, forming metastable phases or unique microstructures. The kinetics of nucleation and growth determine the final microstructure and its characteristics.

3. Kinetics of phase transformations: Phase transformations involve the change of one phase into another, and their kinetics strongly influence the resulting microstructure and properties. The kinetics

of nucleation, growth, and diffusion during phase transformations dictate the development of non-equilibrium phases and microstructural features.

4. Metastability: Non-equilibrium processing can lead to the formation of metastable phases, which are thermodynamically unstable but kinetically trapped. The formation and stabilization of metastable phases depend on factors like cooling rates, deformation rates, and the presence of nucleation sites. Metastable phases exhibit unique properties compared to their equilibrium counterparts, such as higher hardness, increased solid solubility, or improved mechanical strength.

5. Interface and grain boundary effects: Interfaces, such as phase boundaries, grain boundaries, and surfaces, have a significant influence on material behavior during non-equilibrium processes. Interfaces act as sites for nucleation, diffusion, and energy dissipation, affecting the growth of new phases, microstructural evolution, and mechanical properties. The atomic and electronic structure of interfaces plays a crucial role in determining their properties and behavior.

6. Thermodynamic driving forces: Non-equilibrium processes are driven by thermodynamic imbalances or driving forces. These imbalances can result from temperature gradients, mechanical stresses, concentration gradients, or external fields. The non-equilibrium conditions induce energy and entropy flows within the system, leading to changes in microstructure, phase transformations, and material properties.

7. Kinetics of defects: Defects, such as dislocations, vacancies, or grain boundaries, play a vital role in non-equilibrium processing. High deformation rates or rapid cooling rates can generate or annihilate defects, influencing the microstructural evolution and mechanical behavior of materials. The kinetics of defect generation, migration, and interaction affect the material response during non-equilibrium processes.

2.1.1 Mechanical alloying

Materials synthesized by mechanical alloying experience severe plastic deformation due to shear, torsional forces, and high impact. The basic steps are cold welding (solid-state welding), fracturing, and rewelding of powder particles [1]. In this technique, a mixture of alloys, metals, ceramics, or composite is milled together by the interaction of the powder along with the grinding medium. As a result, supersaturated solid solutions, composites, nanocrystalline materials, high-entropy alloys, and others can be obtained [2].

By adjusting the weight of the grinding medium (often metallic balls), the addition of particle control agent (PCA), and milling time, the morphology, particle size distribution, and phase fraction of the powder can be controlled. Several more variables are involved in this technique that directly contributes

to the powder's properties. This includes the type of mill, milling container (size and composition), atmosphere, temperature, milling time (on and off time), and speed. The effect of each variable varies for each material. For simplicity, a general mechanism will be explained in section 2.1.1.1.

Following Turnbull's criteria, in mechanical alloying, the system is taken out of equilibrium due to the introduction of high energy. This will cause the material to be susceptible to forming non-equilibrium or equilibrium phases based on the free energy available. When this occurs, the system is brought back to equilibrium leading to the synthesis of a wide variety of materials. Metallic glasses, quasicrystalline materials, nanostructured materials, high-entropy alloys, and others can be obtained [2].

2.1.1.1   Alloying mechanism

Mechanical alloying occurs due to the energy transferred from the collisions of the grinding balls with the powder, see Figure 2.1. During this process, the powder experiences repeated deformation, cold welding, and fracture leading to strain-enhancing diffusion, progressively homogenizing the powders, and eventually forming an alloy [3]. This is a dry process which means it is carried out entirely in the solid state that occurs. The process occurs inside a sealed container with an ambient or inert atmosphere.
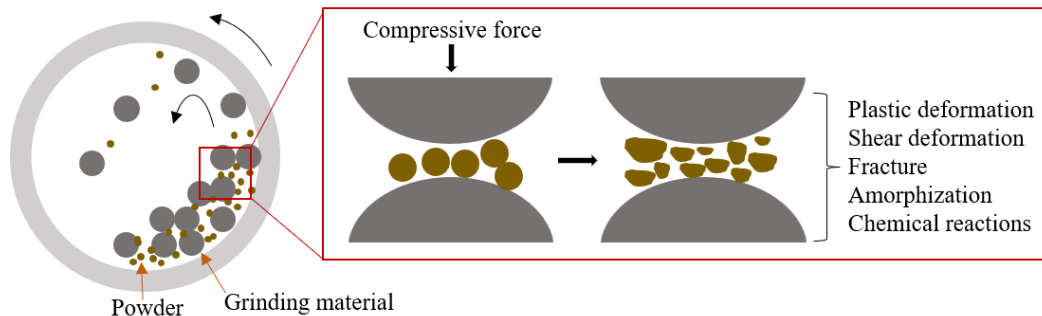
Figure 2.1 Sequences of main steps during the ball milling process.

Before the material reaches a steady state in which the size does not change and the composition is homogeneous [1], the powder has several sizes and morphologies as well as various combinations of the starting constituents. Before steady state, the fracture of particles predominates over cold welding as the deformation continues with a high occurrence of fatigue failures. This means the powder continues reducing its size (fracture), and no agglomeration occurs (cold welding) [3]. Once the steady state is reached, there is a balance between the fracture and the cold welding. At this point, the size distribution is narrower than at the beginning of the process [2]. Additionally, the composition of every particle is the same, and there is saturation in residual strain. The time necessary for each stage to occur depends on the chemical composition of ingredients, initial particle size, and the energy input during the process.

A general description of how the alloying of different constituents occurs can be explained in terms of the deformation they undergo. The material is deformed due to the high energy introduced. When severe plastic deformation occurs, the particles experience an increase in grain boundaries, vacancies, dislocation density, stacking faults, and several other defects. Combining all these defects and the local rise in temperature facilitates the diffusion of solute into the matrix. This results in the formation of equilibrium (solid solutions and stable phases) and non-equilibrium (metastable, quasicrystalline phases, and amorphous) alloy phases. Whether the equilibrium or non-equilibrium phase is formed is determined by their relative free energy values with respect to the energy stored. Thermodynamic principles suggest that the phase with lower free energy will form preferentially because it will have more stability. The composition must also be considered, although this is independent of each material system. For a more general and simplified explanation, this can be clarified in terms of forming a solid solution, amorphous, and crystalline phase. Each of these includes both equilibrium and nonequilibrium phases.

The sequence of formation of phases is the following. Intermetallics are formed first, then an amorphous phase, and lastly, a crystalline phase is formed. The steps for forming each phase will be explained using the example from [2] in which a Fe-based alloy with 58% of solute is evaluated. When the mill process begins, only an elemental blending of powder mixtures is present (stage 1). As the mechanical alloying progresses, energy is added to the material, causing an increase in the free energy of the powder by introducing crystal defects. As a result, an α-Fe solid solution, or a mixture of solid solution with intermetallics, is formed (stage 2) because it is the closest option with the lowest free energy. As the milling time increases, more defects are introduced in the material, causing this phase to increase its internal energy. Consequently, a homogeneous amorphous phase is formed (stage 3). Following the same logic that, at higher milling time, more excess energy is added to the system, stage 3 will no longer have the lowest free energy. Therefore, the next phase is formed (stage 4). This phase is a mixture of the original α-Fe solid solution + intermetallics + amorphous phase. Finally, when the last phase is achieved, the crystalline phase (stage 5), it will be an equilibrium mixture of a α-Fe solid solution + intermetallics.

2.1.1.2 Mechanochemical synthesis of composites and nanocomposites

Ball milling has been extensively employed to synthesize composites and nanostructures. This technique allows the introduction of reinforcement due to the effective dispersion of fine and nano-size particles. The volume of reinforcing particles in the metal matrix depends on the material composition. Ball milling allows adding various particle types, sizes, morphologies, and volume fractions. However, few limitations have been reported [4-6]. For smaller particle sizes, inhomogeneous dispersion can occur, especially when adding nanoparticles, as the volume fraction is typically limited to about 2–3%. For

particle sizes above ~1 μm, the milling process is more suitable at higher reinforcement volumes, and longer mixing times are recommended.

The synthesis of composites by ball milling is advantageous because no external heat is required to propitiate the diffusion of the elements [7]. This is possible because of the repetitive fracture and cold welding steps between the balls and the particles. When the particles are fragmented, their surface area increases, creating more contact points between the reinforcing material and the metallic particles [8]. As the collisions increase, more energy is accumulated within the powder leading to excess lattice defects (dislocations, lattice strain, etc.), which facilitate the interdiffusion between the particles [9]. As the particles keep reducing in size, the diffusion distances decrease, leading to a homogeneous distribution of the reinforcement into the matrix. This mechanism justifies why elements with low solubility can be alloyed together.

Adding NPs can be challenging in ball milling due to the possible lack of sufficient interfacial bonding [5,8,10]. However, thanks to grain refinement as a function of milling time, the NPs can be easily introduced in the matrix. Grain-refinement mechanisms were explained by Xun et al. [10]. They reported the evolution of plastic deformation and its impact on the microstructure of the powders without the addition of reinforcement particles. As mentioned above, when the milling time increases, more energy is introduced into the systems due to severe plastic deformation. The excess energy can be stored as shear bands containing a high density of dislocations and small grains [7,10]. The dislocation density gradually increases due to the increase in the lattice strain. To achieve a lower energy state, the crystal is disintegrated into sub-grains separated by low-angle boundaries. Specifically, these low-angle boundaries are formed due to the dislocations' aligning, annihilating, and recombining. With the increase in plastic deformation, more dislocations are absorbed into the boundaries, and therefore, the small-angle boundaries are replaced by high-angle grain boundaries among nano-size grains. Finally, when the material reaches a steady state, uniform grain size is obtained. Salur et al. [11] reported a study in which by increasing the milling time up to 10 hours, Y_2O_3 NPs were uniformly distributed into an Al matrix.

2.1.2 Laser ablation

Laser ablation is the thermal or nonthermal process of removing atoms from a solid by irradiating it with an intense continuous wave or pulsed laser beam [12]. This technique has multiple applications, such as laser cutting, modification of materials' surface and physical properties, synthesis of nanoparticles, laser deposition, and several more. Only laser ablation in liquid (LAL) will be considered for this work.

This technique is one of the fastest and most efficient methods to synthesize metallic, ceramic, or composite nanoparticles (NPs). This technique does not require long reaction times, high temperatures, or

multi-step chemical reactions [13-15]. LAL provides the advantage of producing a colloidal suspension, stabilizing the NPs without surfactants or ligands. Additionally, there is no need to add precursors or chemical reagents. This increases the probability of obtaining NPs with high purity and reduces contamination or formation of byproducts. Heterostructures could also be formed by functionalization processes of the pure and bare NPs.

When the solid material is irradiated by a continuous (CW) or pulsed laser above its ablation threshold, it will absorb the energy and will develop different electronic and lattice responses. The beam induces an electronic distribution out of thermodynamic equilibrium that causes thermalization by electron-electron and electron-phonon interactions inside the material [16]. These interactions will depend on the electronic structure of the material, wavelength, and type of laser (CW or pulse). When the interactions subside, electronic recombination is re-established, and equilibrium is attained.

Thermalization can be complex for metals as this phenomenon occurs extremely fast (within a few femtoseconds) and will experience both electro-electron and electron-photon interactions. A basic and simplified mathematical explanation for laser-matter interaction in metals has been explained by P. Allen [17]. Nevertheless, the mathematical models are outside the focus of this work.

2.1.2.1 Pulsed laser technique

A pulsed laser is a type of laser that emits light in the form of discrete pulses. Each pulse delivers a confined amount of energy defined by the pulse's duration and the laser source's energy. There is a wide range of pulse durations, ranging from femtoseconds to microseconds. This technique is driven by a wide range of parameters, including wavelength, beam quality, pulse duration, frequency or repetition rate, recovery time, and power. In contrast to continuous lasers (a topic discussed in section 2.1.3.2), pulsed lasers contain extremely high peak energies. In the case of femtosecond and picosecond lasers, they deliver the highest peak energies, spanning from megajoules or even higher. Nanosecond and microsecond lasers typically have the lowest peak energies. The laser ablation process explored in this work is limited to only picosecond (ultra-short pulses) and nanosecond pulses (short pulses). The differences between each process are described in the following section 2.1.2.2.

A summary of the main steps that take place in the interaction of a pulsed laser with a metal solid are the following:

1. Absorption: The metal surface absorbs the energy from the laser beam. Depending on the pulse duration and the irradiation, absorption can occur in the electrons, lattice, or both. In lattice absorption, the lattice absorbs the phonons causing excitation of the crystal lattices, leading to thermal diffusivity along the microstructure. In electronic absorption, the energy is absorbed by the free

electrons in the conductive bands, and it is subsequently transferred into the lattice. When both occur, an intermediate state occurs.

2. Melting: the absorption of laser energy leads to localized heating and subsequent melting of the solid. The volume of material melted depends on each of the parameters mentioned above. Short pulses tend to reach wider laser penetration, resulting in bigger melt pools due to the higher thermalization effects. Ultra-short lasers reach deeper penetrations due to the highest peak densities. However, fewer heat-affected zones are observed around the focused area.

3. Ablation and vaporization: rapid melting and vaporization can occur due to the high laser intensities. Due to the high temperatures and pressures, a plasma plume is formed when the laser comes in contact with the material's surface. Several reactions occur within this plasma plume, causing the ejection of material.

4. Phase transitions: thanks to the rapid heating and cooling rates, the material can experience the formation of unique microstructures and changes in their properties. Due to the non-equilibrium nature of this process, metastable phases can be retained at ambient conditions due to the rapid solidification of the species formed.

2.1.2.2 Short and ultra-short pulses

Ultra-shorts pulses are defined as pulses that occur within a scale of femtoseconds to a few picoseconds. Short pulses are more in the range of nanoseconds. In the previous section, it was briefly mentioned that the duration of the pulse has a significant contribution to the electronic and lattice responses of the material. If the pulse duration is more prolonged (short pulses) than the interaction time of electron-electron and electron-phonon, the electrons and the lattice of the material will thermalize within the pulse duration and will experience similar temperature evolution. However, for ultra-short pulses, the electron and lattice are decoupled, and only the free electrons will interact with the laser beam. This occurs because the laser pulse length is shorter than required for energy relaxation processes such as heat diffusion and electron-to-lattice energy transfer. Figure 2.2 illustrates the differences between short and ultra-short pulses.
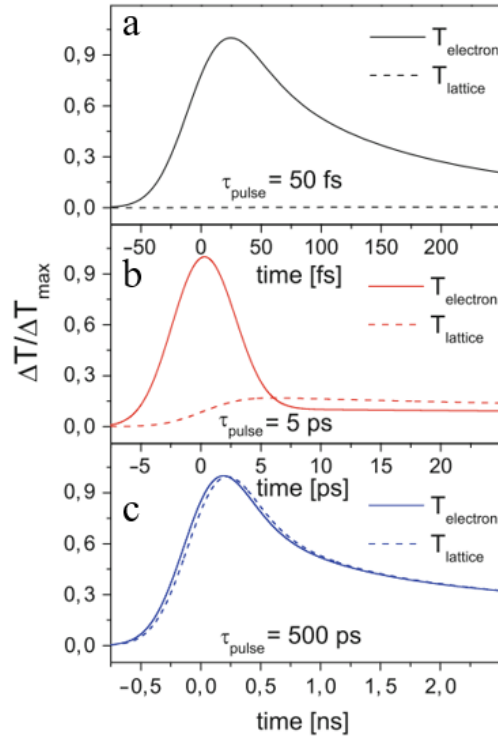
Figure 2.2 Temperature profiles that the electrons and the lattice experience at different pulse duration. a, b) With ultra-short pulses, the electrons and lattice are completely decoupled, and the lattice is unaffected. c) With short pulses, the electron and lattice follow almost identical temperature evolutions. [18].

The differences between short and ultra-short pulses can be explained by describing what mechanisms occur within specific time frames. For simplicity, an example of pure copper's electronic and lattice temperature profiles will be used as a reference [16]. When Cu is irradiated with a pulse of 50 fs, the lattice remains unaffected because the pulse time is insufficient for it to react; thus, no thermalization occurs. However, the electrons are excited and experience thermalization. This is a highly energetic process in which ablation for fragmentation occurs, and the system can be pushed into a metastable state. When the pulse duration increases to tenths of picoseconds, the material can also be ablated by fragmentation and explosive boiling. However, in this case, there is enough time to transfer energy into the lattice. The last case is when the pulse duration is longer (>100 ns), and both electrons and lattice dynamics are similar [18]. The ablation, in this case, occurs via boiling and vaporization.

It is essential to clarify that for ultrashort pulses, laser fluences have a crucial role. At fluences greater than a specific value, the energy penetration into the material is controlled by the depth of penetration of the heat. At lower fluences, the ablation will be dominated by the thermal diffusion of the electrons instead of only by the optical absorption of the beam. This gives rise to a thermal diffusion in which the ablation occurs via fusion and vaporization (similar to short pulses).

13

Another parameter to be considered is the focus of the light beam and its intensity since the particle size distribution and the volume of ablated material depend on it. For example, higher pulse energy is required when the working distance above the target is longer. This will improve the size distribution of the NPs. Regarding the volume of ablated material, the intensity of the laser matters more than the focus. To ablate the same amount of material for different pulse durations, ultra-short pulses require higher intensities than shorter pulses. For example, ablation with 100 fs pulses requires an intensity in the range of 10^{13} to 10^{14} W/cm^2 approximately [18], while for pulses of 30-100 ns, an intensity of the order of 10^8 to 10^9 W/cm^2 is required [19].

2.1.2.3   Mechanism of synthesis of nanoparticles by laser ablation

LAL generally occurs inside an enclosed container with the liquid and solid target material. When the target is irradiated, ablation can occur via different mechanisms, such as vaporization and boiling, explosive boiling, or fragmentation. What determines which mechanism occurs depends on the laser energy and the rate between the pulse duration to the electron-phonon coupling time [13].

To simplify the formation of NPs by LAL, an example of the synthesis of Ag NPs in a polyvinylpyrrolidone solution was used as a reference [20]. A 10 ns pulse duration laser was used and monitored by executing time-resolved shadowgraph imaging. The steps for synthesizing NPs are described below and illustrated in Figure 2.3.

1. When the solid target absorbs the energy from the laser beam, an unbalanced plasma plume is formed. This plume contains material species such as ions, neutral atoms, and clusters. Unlike ablation in gas or air, the liquid medium causes the plasma plume to be more tightly confined under high temperature and pressure conditions. As a result, more nucleants are formed, and NPs can grow at a faster rate. At the plume-liquid interface, the elevated temperature causes ionization and vaporization of the liquid, resulting in the creation of a "liquid plasma."

2. As the plasma plume expands, two shock waves traveling in opposite directions are formed, one through the target and one through the liquid. During this process, chemical reactions occur within the plume, at the plume-liquid interface, or within the liquid. As a result, nucleation and growth of NPs take place. Based on the energy available in the system, NPs could also be expelled directly from the target as droplets.

3. Subsequently, the plume expands and cools adiabatically, releasing its energy to the liquid medium. When this occurs, a cavitation bubble is generated surrounding the ablated material. The bubble reaches its maximum size when the gas within it comes into equilibrium with the surrounding liquid. Then its temperature and pressure decrease until it is finally extinguished.

4. Finally, when the cavitation bubble is extinguished, the species created are stabilized or "frozen" (based on Turnbull's analogy), forming the NPs. These NPs are therefore distributed in the liquid medium.
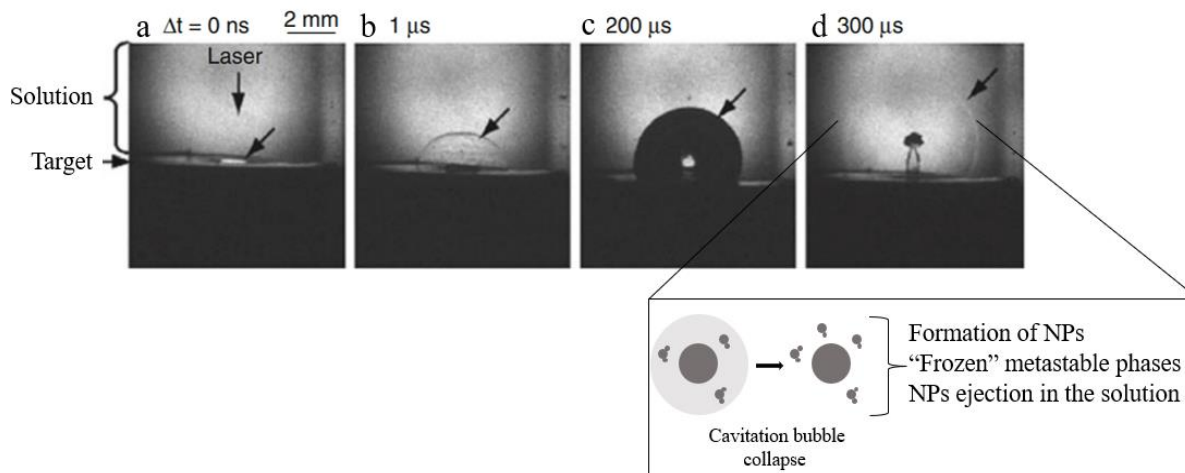
Figure 2.3 Time-resolved shadowgraph images showing the steps that take place during laser ablation in liquid to synthesize nanoparticles. a) Absorption of the laser beam. b) Formation of shock waves. c) Formation of the cavitation bubble. d) Collapse of the cavitation bubble. Figure edited from [13].

2.1.3 Laser melting

A high-intensity laser beam provides energy input faster than a system can achieve thermal equilibrium. This results in a transient state where the material is heated to temperatures well above its melting point. The non-equilibrium conditions lead to the formation of a highly dynamic molten pool on the metal surface, followed by rapid solidification upon laser removal. This process can induce various phenomena, such as the generation of fine-grained or amorphous structures, changes in material properties, and the possibility of achieving complex microstructures with tailored properties. Application fields for laser melting include surface modification (surface cladding, surface annealing), laser welding, and additive manufacturing, well-known as 3D printing. In this dissertation, only laser additive manufacturing will be covered.

2.1.3.1 Laser melting mechanism using ultra-short pulse laser

The interaction between a pulse laser and the solid material is controlled by the absorbed power density and the interaction time (total irradiation time). As discussed in section 2.1.2.2, there are various mechanisms based on the duration of the laser pulse. In this section, the use of an ultra-short laser will be discussed.

When the laser melting starts, there is insufficient time to induce electron-to-lattice energy transfer, see Figure 2.4. That means that the crystal lattice remains undisturbed with no or almost no thermal diffusion, and only the free electrons in the conduction band absorb the photons. It is important to mention that the maximum electron temperature is reached at the end of the laser pulse [21]. However, within multiple consecutive pulses on the 1-100 ps time scale, thermalization effects can occur between the free electrons and the lattice [18]. This leads to the diffusion of thermal energy [21] and, consequently, the melting of the material. For a femtosecond laser, this thermal diffusion is limited to a very small area. Nevertheless, the area affected by the laser is determined by the energy loss and will depend on the strength of the photon-electron coupling of the material [22].
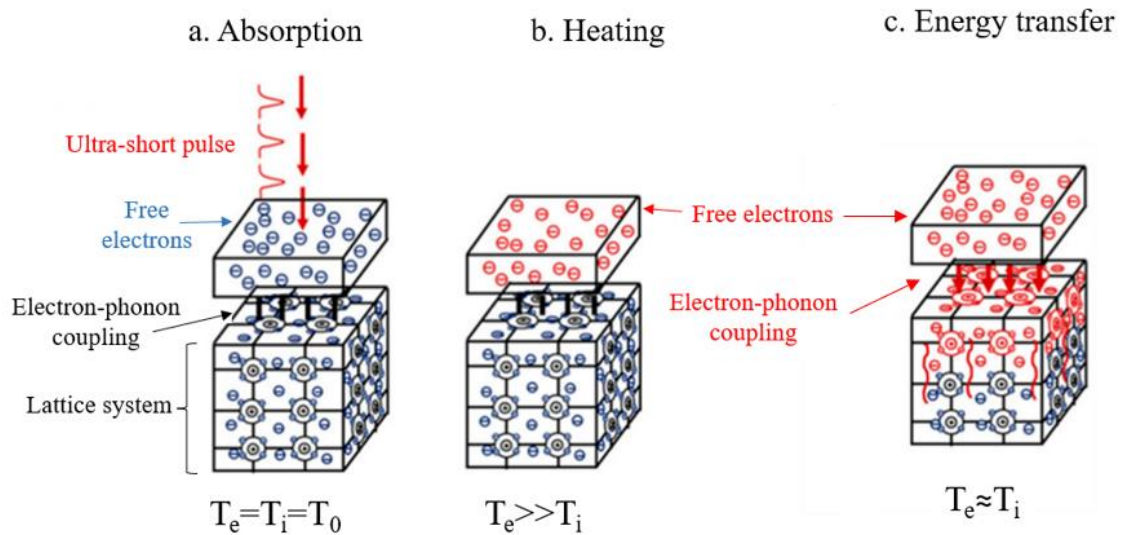
Figure 2.4 Mechanism of interaction between ultra-short pulse laser and the material. T_e is the electron temperature, T_i is the lattice temperature, and T_0 is the ambient temperature [21].

In summary, the sequence of the steps responsible for the melting of the material using an ultra-short pulsed laser is as follows: 1) the laser energy is absorbed by the interaction of free electrons and phonons, 2) electrons become more excited as the number of pulses increases, 3) the energy from the electrons is transferred to the crystal lattice, 4) the lattice systems reach energy similar to the electron temperature leading to the material melting. Equilibrium is finally established when the energy is equally distributed. 5) The molten material experiences very high cooling rates leading to the formation of amorphous, crystalline, or metastable phases.

During the heating and re-heating of the material, phase transformations can occur. These are triggered based on thermal defects (degree of disordering) in the crystal lattice. In ultra-short pulses, the strong electronic excitation is responsible for the lattice overheating to originate the lattice transformations.

Additionally, electrons also contribute to producing significant atomic displacement, thereby changing the entropy of the system and growing point defects [23]. However, the increase in entropy caused only by the excitation of electrons is significantly less than the lattice disorder associated with melting. Other mechanisms related to phase transformations in ultra-fast laser processes are outside the research objectives of this dissertation.

Recent efforts in the study of ultra-fast laser melting have been primarily focused on developing more fundamental science to understand the capabilities of this technology. These investigations have mainly selected advanced materials that are extremely difficult to melt using traditional laser additive manufacturing with continuous lasers. Some examples include refractory materials, glass, multi-material layered structures, and high-conductive materials. Further research is still necessary to reveal the physical mechanisms of each group of materials and improve the process to extend the application range. Regarding process improvement, additional guidance is needed to develop more refined process windows. This will significantly reduce the extensive range of parameters available. Despite the vast potential and recent advances of ultrafast-laser additive manufacturing, this technology is considerably behind and less explored than traditional industrial techniques using continuous wavelength lasers.

2.1.3.2   Laser melting mechanism using a continuous wave (CW) laser

In contrast with a pulsed laser, a CW laser emits a continuous beam with constant power for as long as the laser source is on. The melting mechanisms of a metallic material due to interactions with a CW laser are slightly less complex than a pulsed laser. However, it is still a process that requires precise control of each of the parameters involved, e.g., wavelength, power, beam diameter, beam shape, beam scanning (speed and direction), and dwell time (exposure time). Regardless of the laser technology used, material properties also play a crucial role in melting. The most important factors are thermal conductivity, reflectivity, melting point, and heat capacity.

The steps in the melting process for a CW laser are similar to those described in the pulsed laser. However, the thermodynamic and kinetics mechanisms differ as both techniques have specific spatial and temporal time scales. The main differences between pulsed and continuous lasers during the melting are the following:

1. Energy delivery: With a continuous laser, the heating occurs over a more extended period, and the increase in temperature is steadier and more gradual. However, with pulsed lasers, the heat input is more localized. This leads to better control over the temperature profile due to the rapid delivery of energy.

2. Heat transfer: with a pulsed laser, the heat input is more localized (higher heat control), leading to a more limited heat diffusion around the focus area. With a continuous laser, the exposure time is longer, causing the material to experience more heat diffusion, leading to larger heat-affected zones.

3. Melting efficiency: If the efficiency is defined by the control of the temperature profile and the control of the thermal effects on the surrounding area, pulsed lasers govern the melting process. Nevertheless, if efficiency is defined by the volume of molten material, continuous lasers will dominate.

4. Operation scale: due to the lower heat damage in the material when using a pulsed laser, working at micro and even nanoscales is possible. Compared to a CW laser, the higher thermal stress effects limit the scale at which it can be performed.

2.1.3.3 Laser melting in laser powder bed fusion additive manufacturing

Laser powder bed fusion is an additive manufacturing technique for fabricating complex 3D components. Roughly speaking, this process consists in using thermal energy from a laser beam to selectively melt powder located in a powder bed [24]. The general steps involved in producing 3D components start with spreading a layer of powder on a powder bed, which is a smooth metallic stage. The layer of the powder is determined by a scraper/roller that inserts a specific force to compact the powder and regulate the particular height of the layer. Then, the laser beam focuses on specific areas in the powder bed to melt the powders. Once the first layer of powder is melted, another layer of powder is added to the powder bed with the same height as the previous one. Finally, all these steps are repeated until the component is printed.

The melting of the material depends on a combination of multiple factors such as powder feedstock (size distribution, morphology, composition, and properties), laser powder and speed, powder thickness layer, and laser scanning strategy (hatching space (distance between two adjacent laser scan paths), pattern, and rotation). As described by Narasimharaju et al. [25], the most critical thermophysical phenomena that occur in powder bed fusion-laser bed (PBF-LB) can be explained in relation to 1) laser-powder interaction, 2) melt pool dynamics, and 3) solidification dynamics. Figure 2.5 summarizes these three phenomena.

In the first case, radiation, convection, and conduction dominate the heat transfer between the laser beam and the powder. During the absorption, the photon energy will be converted into thermal energy thanks to the multiple reflections within the powder layer. This absorbed energy is converted into thermal energy leading to powder melting and reheating the already printed layers. The melting mode in this process depends on the power and travel speed of the laser. The ideal case could be defined as the

conduction mode governing the melting [26]. This is because less defect formation is possible, especially lack of fusion and keyhole porosity, due to the better overlapping of the melt pools. To make this possible for each material, experimental process windows and simulations are developed to confirm and predict the regions in which this mode is dominant. It is well known that at higher laser power intensities and lower speeds, the keyhole mode becomes dominant. A keyhole refers to forming a vapor-filled cavity due to rapid heating and localized vaporization. In this mode, the laser energy is primarily absorbed within the cavity instead of the solid material. Key-hole mode is not desired in PBF-LB due to the formation of defects. These defects are caused by the melt pool instabilities that occur due to the recoil pressures that affect the surface tension of the molten metal, thereby altering the Marangoni flow in the melt pool [27]. It is important to mention that both modes can occur simultaneously during PBF-LB. This mode is known as the transition mode, and it can happen without the formation of defects.

For the second case, the control of melt pool dynamics is critical to avoid defect formation in the printed components. Understanding the melt pool behavior is challenging due to the rapid heating and solidification rates of the material. The melt pool undergoes a combination of various complex forces such as gravity, surface tension, buoyancy, and capillary. Each of these forces has a specific predominance and influence on the kinetics and thermodynamics of molten material. For example, capillary, buoyancy, and surface tension are considered the primary driving forces [28]. On the other hand, gravity and viscosity are regarded as secondary driving forces. The interaction of all these factors is highly challenging, especially because in-situ experiments with ultra-high resolutions and speeds are required to reveal the melt pool dynamics. However, as explained by Narasimharaju et al. [25], the shape and stability of the melt pool are usually controlled by the capillary flow and surface tension. The success of printing multi-layers will also depend on these factors and the wettability of the molten material in the previously solidified material.

Lastly, solidification starts with the formation of the melt pool, specifically at the boundary of the pool, and then is directed toward the center [29]. If the melt pool experiences instabilities, the solidification will be affected. Some of the most common defects reported as a cause of rapid solidification, whether or not the melt pool experienced instabilities include porosity, residual stresses, warping, and surface roughness. The solidified microstructure of the material depends on the thermal gradients (G), the front velocity (V) of the solid/liquid interface, and cooling rates. In PBF-LB, the solidification is governed by heterogeneous nucleation because of the fast cooling rates. As a result, the grains grow in random directions along the temperature gradient (build direction). Since this process creates consecutive layers, the grains experience an epitaxial growth, commonly with a columnar solidification front. However, depending on the material composition and laser parameters, the

solidification could lead to equiaxed grain formation instead of columnar grain growth. More information about the solidification mechanisms is described in Chapter 5 and Chapter 6.
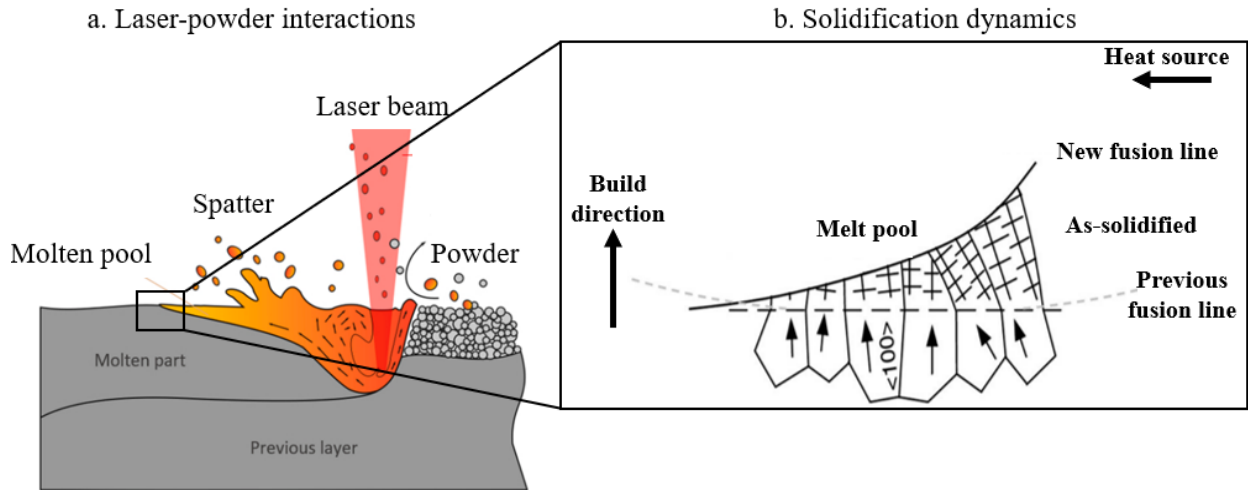
Figure 2.5 Illustration of the thermophysical phenomena in PBF-LB. a) Laser-powder interaction. b) Epitaxial growth leads to the formation of columnar grains [25].

2.2 Material systems studied for laser ablation, mechanical alloying, and laser melting

2.2.1 MoC-graphite synthesis by ball milling

Transition metal carbides have received considerable attention as advanced materials for their attractive physical and chemical properties. Some of these properties are high hardness, thermal stability, superconductivity, reasonably high chemical inertness, and especially catalytic performance [30-32]. In recent years, molybdenum carbides have been extensively utilized in hydrogen evolution reactions (HER), especially heterostructured MoC/Mo_2C.

Molybdenum carbide is a complex system composed of various stable and metastable phases. The most common are MoC, $\alpha\text{-}Mo_2C$, and $\beta\text{-}Mo_2C$. The cubic $\delta\text{-}MoC$ has recently been reported more in catalysis. Finally, the most complex phases are $\gamma\text{-}MoC$, $\gamma'\text{-}MoC$, and $\eta\text{-}MoC$. When this composite is synthesized, some methods form a supersaturated solid solution of carbon in the carbide matrix. It has been found that the excess carbon encapsulates the carbide leading to advantages such as control of particle size, functionalization of heterostructures, better catalytic performance when the coating is graphite [33], and higher resistance to hostile environments.

Graphite-Metal Carbides composites have been studied since the 1960s [34-36]. When combined, the undesirable poor thermal shock resistance and reactivity with oxygen are minimized [37], and properties

such as electrical conductivity, energy absorption, and mechanical resistance are also improved [38,39]. Nevertheless, further investigations are still required to develop more efficient methods for its synthesis and to generate more fundamental information about the metastable phases.

For the production of this composite in bulk, liquid phase sintering, exceeding temperatures of 2584 °C, has been the most used technique [19]. For powder production, the typical route for powder production involves wet chemistry followed by heat treatments above 700 °C [40]. More processes are implemented; however, most require very complex methodologies and are not economically preferable. Mechanical alloying has also been utilized [41,42]. This technique is considered one of the most feasible methods based on production yield, low cost, and versatility to produce various chemical compositions. A general overview of the mechanism to make this composite by mechanical alloying is described as follows.

A critical aspect of carbon-metal interactions is the high-temperature diffusion between carbon and metallic materials [43]. Mechanical alloying is a viable alternative to overcome the challenge in the synthesis since the plastic deformation refines the particle and grain sizes and increases the grain boundary area [2]. The decreased particle size reduces the diffusion distances between C and Mo [41,42]. The diffusion is further aided by the increased defect density and a local rise in temperature. The combination of these effects permits sufficient diffusion to occur in the interfacial regions of the nanocrystalline grains to form molybdenum carbide and also facilitates the dispersion of graphite as a second phase to effectively strengthen the carbide matrix creating an intimate bond at the interface between the two phases [41, 44]. Up to this point, different heterostructures can be obtained. For example, molybdenum carbides embedded in amorphous carbon, molybdenum carbides coated with amorphous or graphitic structures, or a combination of both [41]. The composition of the carbides is variable depending on the stoichiometries used and if other precursors are utilized [42,44].

An additional heat treatment might be required to conclude the formation and stabilization of the MoC-carbon system. This treatment is usually shorter than the ones implemented in the other methods. In this study, a temperature of 1000 °C in inert gas. This step causes the formation of a polyaromatic carbon matrix or improves the crystallinity of the graphite coating. Additionally, better stability of the carbide and homogeneity of the phases can be achieved. In summary, the most important steps can be represented with the following analogy described by Bokhonov et al. [44]:

1. Mo + C (graphite, coal, amorphous C) → mechanical activation → Mo_xC_y (metastable compound)

2. Mo_xC_y → annealing → Mo_2C + Polyaromatic carbon or Mo_2C + graphitic coatings

It is important to clarify that for step 2, instead of Mo_2C, heterostructures of Mo_2C/MoC could be obtained.

2.2.2 MoC-graphite synthesized by laser ablation

Laser ablation is another alternative for the synthesis of MoC-graphite nanoparticles. With this technique is possible to synthesize molybdenum carbide and carbides composite reinforced with carbonaceous structures. However, this nano-scale system has not been synthesized by the laser ablation method. Therefore, the present study can serve as a guideline for developing the methodology required to synthesize this nanocomposite. Additionally, this work aims to inform the community about the capabilities of this technique.

To date, few studies have reported on the synthesis of carbide nanoparticles [42,43]. The possible methods that can be implemented are chemical vapor deposition processes, carbothermal reduction, the reaction in solution, and sonochemical synthesis [45]. However, these methods have limitations due to working conditions (high temperatures or pressures), very long synthesis times, and the presence of precursors and other chemicals that generate residues in the final product, among others. Laser ablation avoids these disadvantages because the reaction times are fast (even if multiple steps are needed), no surfactants or ligands are needed, and no external temperatures and pressures are required. The latter is possible due to the primary formation mechanism of nucleation occurring within the plasma plume, which has extremely high temperatures and pressures.

Similar to mechanical alloying, a molybdenum carbide coated with carbon structures is possible from laser ablation. The main difference with this technique is that due to the high temperature and pressures available, a different graphitic coating, named onion-like carbon (OLC), can be obtained [46]. Compared with amorphous carbon, OLC has excellent electronic conductivity, better thermal and chemical stability, and higher efficiency for catalytic applications [46,47].

The OLC structures are concentric sheets of graphitic carbon interacting by Van der Waals forces [47]. They belong to the fullerene family and are spherical or polyhedral, although their shape changes depending on the number of defects in their structure. The innermost layer is made up of 60 carbon atoms with a diameter of 0.7 nm, and the number of carbon atoms in the other layers increases in the order of $60n^2$ [46]. The space between each sheet measures approximately 0.34 nm, which is very close to the distance of graphite [47]. Generally, these structures have a size between 5 and 100 nm [47], either hollow or with metallic elements inside them. Among the most common techniques used for their synthesis are the arc discharge method, electron beam irradiation, catalytic decomposition, heat treatment methods to convert amorphous carbon or graphite into OLC, radio frequency plasma, combustion

synthesis, and laser ablation [46]. Despite the numerous processes available, their synthesis still has difficulties, including low purity, structural defects, low yield, and high synthesis costs. With laser ablation, there is better processing control; therefore, most of these challenges (except low yield) can be overcome. However, as a relatively new synthesis method, many ablation parameters must be evaluated to determine the optimal process window.

The formation of these shell structures takes place at the interface between the cavitation bubble and the liquid. The saturated carbon particles will precipitate and grow as a carbon coating around the NPs during the following rapid quenching process during laser ablation. Figure 2.6 illustrates how these nanoparticles are formed. More specific details on the steps involved in forming these structures and the carbide are provided in Chapter 3.
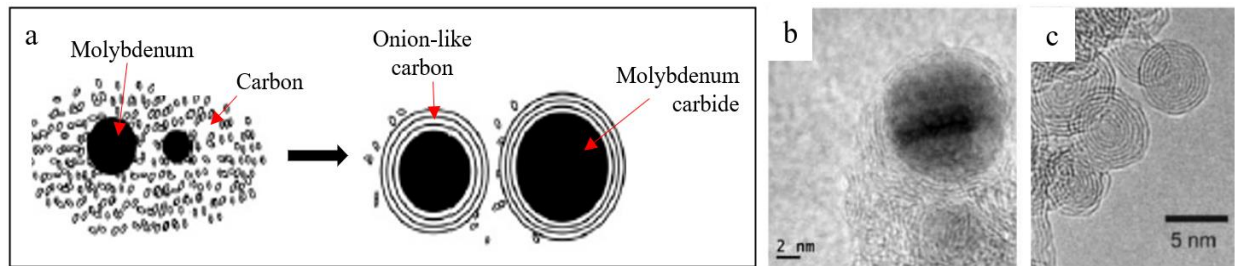
Figure 2.6 a) Formation of MoC-graphite core-shell NPs. Carbon reacts with Mo to form the carbide and OLC. b) Example of MoC-OLC NPs. c) Example of only OLC structures.

2.2.3   The use of CoCr+X (X=SiC or WC) for selective laser additive manufacturing

CoCr-based alloys or Stellite are broadly used as high-temperature alloys, such as aerospace engines and land-based turbines, due to excellent resistance to corrosion and wear [48,49]. Additionally, this alloy has high biocompatibility. Besides titanium, this alloy is one of the most widely used metals in knee implants [50]. Other common fields in which this alloy is used are automotive, marine, and petrochemical industries.

In addition to biocompatibility for medical devices and implants, this alloy must meet other requirements, including long fatigue life, good fracture resistance, and mechanical strength. Meeting these requisites can be complicated since this alloy is strongly influenced by the processing parameter and post-processing treatments. In contrast to stainless steel alloys (AM of 316L will be discussed in section 2.2.3), it is observed that abrupt changes in microstructures are obtained when using different PBF-LB techniques. In general, varying thermal histories during fusion-based AM processing results in microstructural anisotropy and variations in γ-Co FCC and ε-Co HCP phase formation [51].

The two types of CoCr alloys most commonly used in selective laser melting (SLM) technologies are Co-Cr-Mo and Co-Cr-W alloys. The main alloying element in both alloys is chromium within 28-35 at. %. The matrix of the Co-Cr alloys is usually composed of two solid solutions, the face-centered cubic (FCC) γ-Co phase, together with the hexagonal close-packed (HCP) ε-Co phase [52,53]. Both phases can be stable at room temperature; therefore, a dual phase is commonly reported. The γ-Co FCC reported in Co-Cr-Mo alloys tend to be present in a higher volume fraction as this phase is formed during rapid solidification from a liquid with temperature ~1400 °C to room temperature [51]. However, the formation of the ε-Co HCP is predominant when the cooling rate is slow or when the alloy is heat-treated above 800 °C [54]. Another strategy to induce martensitic transformation (γ-ε) is plastic deformation [54], although this alternative is not ideal for AM parts.

Recent advances in SLM focus on manufacturing microstructures rich in the ε-Co HCP phase due to its higher wear resistance, higher strength, and excellent ductility compared to the γ phase [55]. SLM offers advantages in forming internal defects (dislocations and stacking faults). These defects can act as nucleation sites of martensite, therefore researchers are developing parameter optimization to establish proper process-property correlations.

Another phase observed in low carbon CoCr alloys AM printed parts is the σ-CoCr phase [51]. This phase is present as precipitates along the grain boundaries and within the grains. For higher carbon content, the precipitation of globular $M_{23}C_6$-type carbides can be obtained [58]. There is another less commonly reported HCP Co_3W_2Si phase [56], which was observed only in the Co-Cr-W alloys. The formation of these non-equilibrium precipitates in AM CoCr parts is still not well understood, however, it is known that they can provide an increase in yield strength and wear resistance.

Some approaches to strengthening this alloy are the addition of secondary phases to form precipitates, grain refinement, and ε-Co HCP phase by heat treatment. As mentioned before, the latter is extremely challenging due to the high stability of the γ-Co FCC. Nevertheless, Mengucci et al. [56] found that after applying heat treatment, the volume fraction of the ε-Co HCP increased, conserving its original lamellar structure inside the FCC matrix, thereby resulting in improvements in ultimate tensile strength (UTS) and hardness.

Regarding the addition of a secondary phase, up to 1 wt.% in Si and Mn have been introduced [57]. Due to the higher affinity with oxygen compared to Co and Cr, these elements introduce fine oxide inclusions into the CoCr matrix, causing additional strengthening. Carbide precipitation is also expected to occur alongside the formation of these nano-oxide inclusions. The strength contributions of these inclusions are acknowledged to depend on factors such as their volume fraction, size, and distribution

[59]. Two additional advantages related to these in-situ formed precipitates are that they can act as Zenner-pinning particles, thus enabling the grain refinement and the potential formation of equiaxed grains. The formation of ε-Co HCP can be possible during tensile formation leading to higher strength [58]. High residual stresses are concentrated at the interface of the precipitate and the matrix. During deformation, the precipitates interact with the approaching stacking faults (SFs) and with the residual stress available, the SFs will be activated, increasing strain at the interface due to the accumulation of dislocations [58]. As the deformation advances, the strain increases, causing changes in the staking sequence, leading to a transformation of the FFC to the HCP phase.

Among all these possible approaches to modify the microstructure of this alloy, we have only focused on grain refinement by adding SiC and WC nanoparticles. SiC and WC are hypothesized to act as grain refiners that control the solidification microstructure by promoting the nucleation of new grains. What is expected to occur is that since the melting point of the carbides (2730 °C) is higher than the CoCr alloy (1330 °C), the nanoparticles will be transported by the convection and Marangoni flow of the melt pool. Consequently, the carbides can be dispersed homogenously and solidified in the matrix as precipitates. So far, CoCr alloy has not been reported to be reinforced or decorated with nanoparticles; however, these have been achieved using the approach carried out by Martin et al. [59], Li et al. [60], and Chao et al. [61] on Al-based and Ni-based alloys. More details about this mechanism are discussed in Chapter 5.

2.2.3.1 Formation of finer, equiaxed grains during selective laser additive manufacturing

SLM parts are characteristically of presenting epitaxial growth of columnar grains. This is attributed to many reasons:

1. The rapid cooling rates (10^3 - 10^6 K/s) and thermal gradients (~10^6 K/m) can lead to temperature gradients within the material [62].

2. The temperature gradients cause directional solidification. Therefore, the grains grow along the direction of heat flow, forming elongated columns perpendicular to the build plate.

3. Due to the multilayer nature of this process, the previously solidified layer acts as a template for subsequent grain growth. This behavior is enhanced by a low nucleation barrier causing the grains of the next layer to grow with the same crystal orientation.

There are two common options to avoid the formation of long columnar grains in SLM parts: the addition of inoculants or solutes [59] (see Figure 2.7). What dictates their success in forming finer and equiaxed grains is a high value of the growth restriction factor (Q), a uniform distribution of fine particles within the melt, a high nucleation potency, and the control of the solidification dynamics [63]. To satisfy these conditions, the particles must have specific requirements, i.e., low nucleation undercooling, low

diffusion rate, small atomic mismatch, and low interfacial energy [63,64]. When all these conditions are met, heterogeneous nucleation can occur. However, to guarantee the formation of equiaxed grains in SLM, another critical factor must be considered: the generation of constitutional supercooling (CS) at the solid/liquid front (Figure 2.8b).
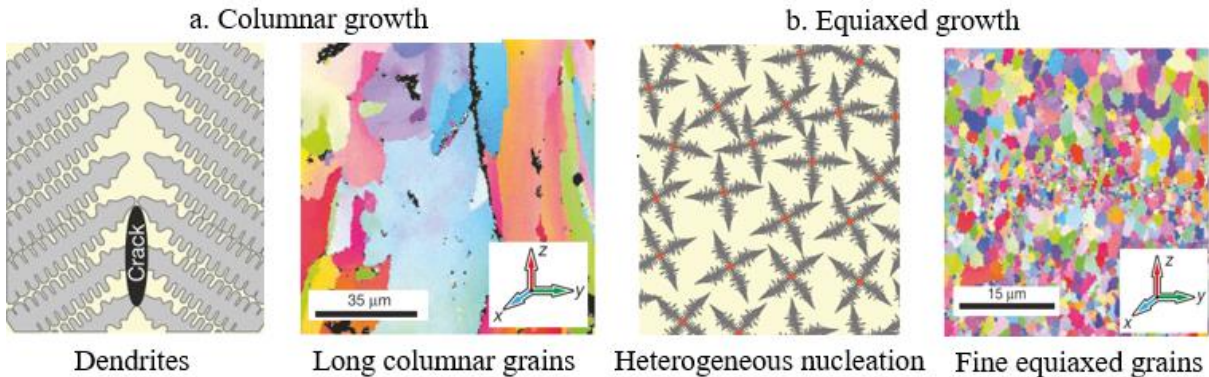
Figure 2.7 a) Conventional columnar grains obtained in PBF-LB. b) Finer-equiaxed grains obtained in PBF-LB after adding inoculants [59].

Before explaining the mechanism for the formation of equiaxed grains during SLM it is important to mention a few more basic concepts. For nucleation to occur, the CS must reach or exceed the undercooling needed to trigger nucleation (ΔT_n). Conventionally, the higher its potency, the lower its ΔT_n. Another important analogy is that at lower nucleation temperatures (T_n), ΔT_n increases, and more ΔT_{CS} is needed to equal or exceed the ΔT_n to develop equiaxed grains. Another term is the nucleation-free zone (NFZ). This zone is characteristic of having insufficient supercooling inhibiting nucleation to occur. The size of the NFZ could be reduced at high growth velocities and high restriction factors [64]. For simplicity, Figure 2.8 illustrates these concepts.

In summary, many factors must be modified to form equiaxed grains. This includes the alloy composition, nucleants, cooling rate, and thermal gradient. To explain the mechanism of the formation of finer and equiaxed grains, the following parallel is provided.
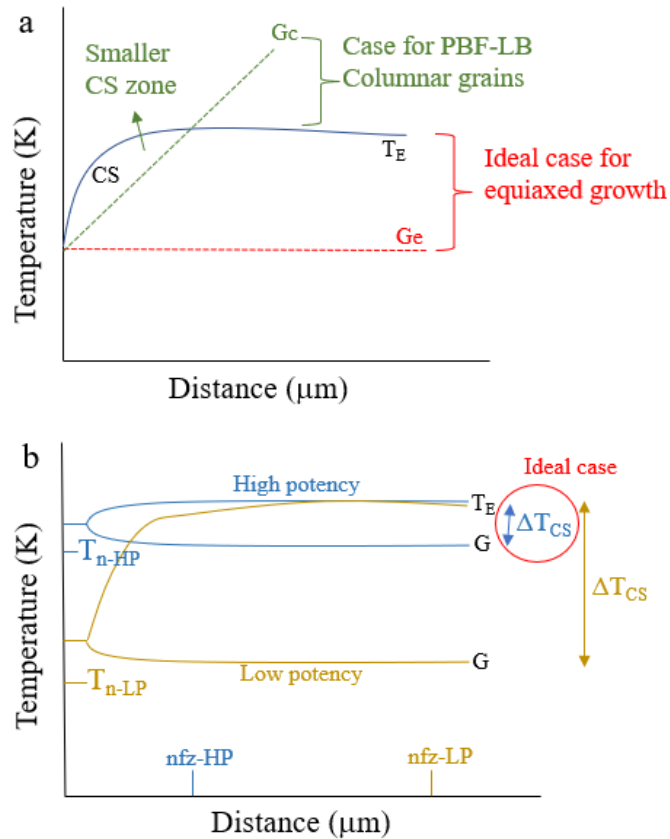
Figure 2.8 a) Effect of constitutional supercooling on the formation of columnar and equiaxed grains. G_e and G_c correspond to the gradients of each solidification mode. b) Effect of the potency of the nucleant particles in the formation of equiaxed grains. Images are not to scale.

In a conventional SLM process, the thermal gradient is very steep (see Figure 2.9a), inhibiting the development of CS. As mentioned before, with no presence of CS, nucleation cannot occur [63]. When this happens, the grains must continue growing until enough CS is achieved. This behavior is the opposite of attaining grain refinement. CS can be obtained when changing the composition at the S/L front by adding or forming a secondary phase [59,65]. The ideal case is to obtain a CS equal to or higher than the amount of undercooling needed to trigger nucleation. To accomplish this, the nucleation temperature must be above the actual temperature gradient (G) (Figure 2.9b). When this occurs, the CS is enough to activate nucleation ahead of the epitaxially growing S/L interface, which leads to equiaxed growth [66]. It is important to mention that the sooner nucleation occurs ahead of the interface, the higher the efficiency is in suppressing the formation of the columnar grains [65]. When the subsequent layer is built, the solidification mode is repeated. However, in case the remelting of the previous layer is not very pronounced to allow sufficient undercooling, the remainder grains can serve as nuclei for the subsequent layer. Thus, enabling epitaxial growth.
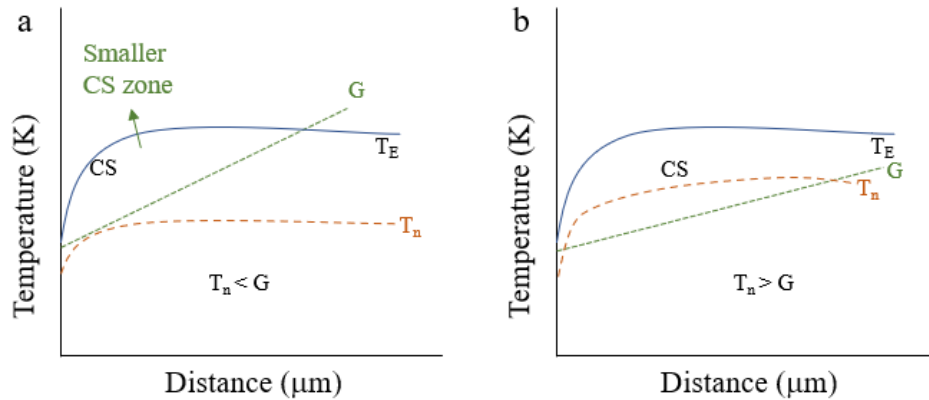
Figure 2.9 a) Steep thermal gradients lead to the formation of columnar grains due to the small CS zone. b) nucleation may occur when the temperature gradient is below the nucleation temperature. Images are not to scale.

Some of the challenges related to this mechanism are due to how complex the SLM process is. For example, solidification is very dynamic along the build direction. This is because the thermal gradients fluctuate as the number of layers increases and depend directly on the geometries of the parts printed. The thermal gradients generally decrease as the number of layers increases due to heat accumulation. Another challenge is related to the rapid solidification rate. Due to this, the incubation period to establish the nucleation might not be enough, thus facilitating the formation of columnar grains [66]. There are also complexities related to the inoculants. It is challenging to achieve a fine distribution of particles as the methods to add these second phases are not well developed yet. Additionally, powder feedstock for SLM requires a multitude of requirements that make it even harder to promote the addition of a second phase. More details about powder feedstock will be provided in section 2.2.4.3. The lack of a good distribution of the particles can be caused during the melting as the melting pool instabilities could affect their flow, thereby causing the evaporation or agglomeration of particles.

2.2.4 Laser powder bed fusion of 316L stainless steel

The thermophysical phenomena that occur during the laser powder bed fusion process are explained in section 2.1.3.3. The 3D-printed 316L alloys follow the same principles and exhibit microstructure with certain characteristics influenced by the specific processing conditions. Some typical microstructure features are described below and summarized in Figure 2.10.

1. Columnar Grain Structure: The solidification starts from the liquid melt pool and progresses upwards as the material cools. This directional solidification process often forms columnar grains aligned along the build direction.

2. Fine Dendritic Structure: Within each columnar grain, a fine dendritic structure is obtained due to the rapid solidification rates. As the material solidifies, dendritic arms grow within the liquid melt pool that nucleates and grows during solidification.

3. Solidification Segregation: During solidification, the distribution of alloying elements can vary within the microstructure due to solidification segregation. Elements such as chromium, nickel, and molybdenum tend to partition differently between the solid and liquid phases, resulting in varying concentrations along the grain boundaries and within the dendritic structure. This segregation can influence the material's mechanical and corrosion properties.

4. Cellular/Subcellular Structure: A cellular or subcellular structure may be observed in some areas of the microstructure, particularly at the surface or near thermal gradients. This structure consists of small, irregularly shaped cells with boundaries formed by dendritic arms or subgrain boundaries. The cellular structures arise from i) constitutional stresses, ii) misorientation between dendrites, and iii) coherency strains due to precipitation networks [67].

5. Presence of Grain Boundaries: Grain boundaries act as interfaces between adjacent grains and play a significant role in determining the material's mechanical properties. In PBF-LB 316L stainless steel, grain boundaries can exhibit various characteristics, including low-angle, high-angle, and twin boundaries. The nature and density of grain boundaries depend on the specific processing conditions and the resulting thermal history.
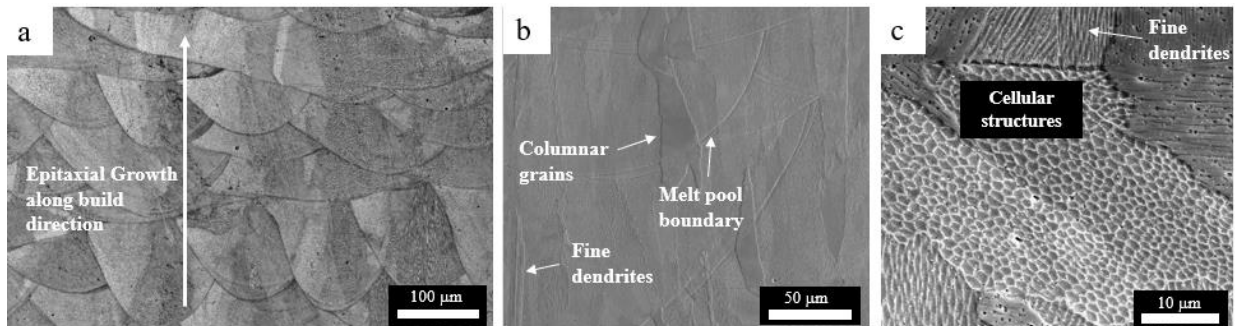
Figure 2.10 Typical features of the microstructure for 316L stainless steel 3D printed with PBF-LB.

These characteristic features vary depending on the laser parameters, powder feedstock, and heat treatment conditions. For this dissertation, only changes related to powder feedstock were considered. To evaluate the powder conditions, powder reusability studies were performed. As the powder is reused multiple times, it can undergo various forms of degradation due to the continual interaction with the laser

beam, powder storage, and oxidation, amongst other interactions. Consequently, the build quality and material properties can be detrimentally affected. The most common defects reported to be related to powder reusability are anomalies in powder spreadability, lack of fusion defects, microstructural inhomogeneities, loss of alloying elements, geometric defects, and surface roughness. More details about the effect of powder reusability are discussed in section 2.2.4.1.

2.2.4.1   Powder reusability in PBF-LB processes

The increasing adoption of Additive Manufacturing (AM) techniques, especially Laser Powder Bed Fusion (PBF-LB), has pushed new efforts to look for improvements in the efficiency and cost of the process. Powder reuse is an approach that could make this technique more economically preferable and environmentally more attractive. Despite the potential cost savings by using reused powder, this strategy has encountered challenges in standardizing reusability guidelines. The most common AM alloys, such as Inconel, AlSi10Mg, Ti6Al4V, and stainless steel (316L, 304, 17-4PH), deteriorate at different rates, making it challenging to predict powder changes and standardize the effect of powder reusability in the final properties of the as-built parts [68]. Consequently, new measures need to be taken to ensure that the quality of the remaining powder is acceptable for further use.

The critical physical and chemical changes in the powders are reflected in changes in circularity, aspect ratio, chemical composition (surface oxides, impurities, and segregates), microstructure (grain size, residual stress, crystallography), packing density, flowability, spreadability, and absorption [27]. These changes are caused by extreme conditions experienced within the melt pool and its surroundings, the sieving conditions, the inert atmosphere, gas flow inside the build chamber, and handling conditions [69]. With many properties changing after each powder use, identifying which specific powder property affects the component quality is extremely difficult [70]. Additionally, the reuse process plays an essential role in forming defects. Therefore, part anomalies and failures cannot yet be assigned solely because of reused powder conditions.

An in-depth understanding of powder reuse studies and degradation mechanisms still needs to be realized. There are still no standardized powder reuse methods for the most used alloys in PBF-LB, and limited insight is available regarding the reused powder properties–part properties relationships. The study of these knowledge deficits is essential to overcome to advance our understanding of PBF-LB systems.

Powder reuse methods vary depending on specific needs and available resources in industry and research. Researchers and manufacturers commonly reuse the leftovers from the build plate and overflow tank and blend them with the remanent virgin powder in feed supplier chambers [69]. However, this

method may not be the most representative to study how only reused powder affects built components. Derimow et al. [71] summarized four of the most common methods currently implemented to study powder reuse. The fourth method corresponds to the case in which only the used powder is separated from the remnant virgin powder and placed in quarantine. When all the starting powder has been depleted, the quarantined powder will be used as feedstock powder. This method is the most relevant for powder reuse as the volume of virgin powder is lower than that of the other methods. Therefore, the quality of the printed components will be dictated by the properties of reused powder instead of virgin.

2.2.4.2   Required characteristics of virgin powder for PBF-LB processes

The quality of powder feedstock is key for the process performance and end part properties. Despite numerous investigations of powder characteristics, there is still a lack of standardization for powder requirements to define physical characteristics such as particle size distribution (PSD), flowability, and tap/apparent density. However, standards for powder characterization techniques such as ASTM F3049 and ISO/ASTM 52907 can normalize the data obtained to simplify their fluctuation.

It is important to mention that powder sampling volume has not been determined in powder reuse studies, but ASTM B215 is commonly used for this purpose. On the other hand, the specific standards for the chemical composition of the reused alloys dictate when the powder shall not be further used in an AM machine (end of life). The reused powder can present contaminants from the chamber (soot, residual powders from previous builds, wear debris, tools, and oxygen during the sieving and storage) [68]. Therefore, in the case of 316L, ASTM F3184 should be followed to guarantee that the alloy is within the chemical composition specifications.

To achieve consistency in the quality of the manufactured components, the properties of the feedstock should also be consistent [72]. Unfortunately, AM powder feedstock can be produced with different characteristics. Gas atomized powder, for example, is most used since it is possible to attain higher packing density, better flow, and less oxygen content at an affordable cost. For this proposal, gas atomization powder will be the only production method considered for comparison purposes from virgin powder to reused powder. Physical, chemical, morphological, and microstructural characteristics of gas-atomized virgin powder for the PBF-LB process will be discussed in section 2.2.4.3. with a comparison with reused powder.

2.2.4.3   Characteristics of 316L stainless steel reused powder

Laser radiation includes complex physical phenomena that modify the powder conditions, e.g., melt pool flow, chemical reactions, and phase transformations of the powder. The high temperature of the laser causes melting, powder ejection, and condensation of the material. The last two phenomena are critical

for powder reuse as both tend to cause more chemical, physical, and microstructural variation in the powder feedstock.

Particle size distribution, chemistry, spatter, condensate formation, and microstructure are among the most significant changes in 316L stainless steel reused powder that affect the build quality. These factors have been evaluated quantitatively and qualitatively from many reuse studies from a range of 5 up to 30 reuses [73,74]. Figure 2.11 illustrates a comparison between virgin and reused powder. Each of these changes is explained in more detail below.
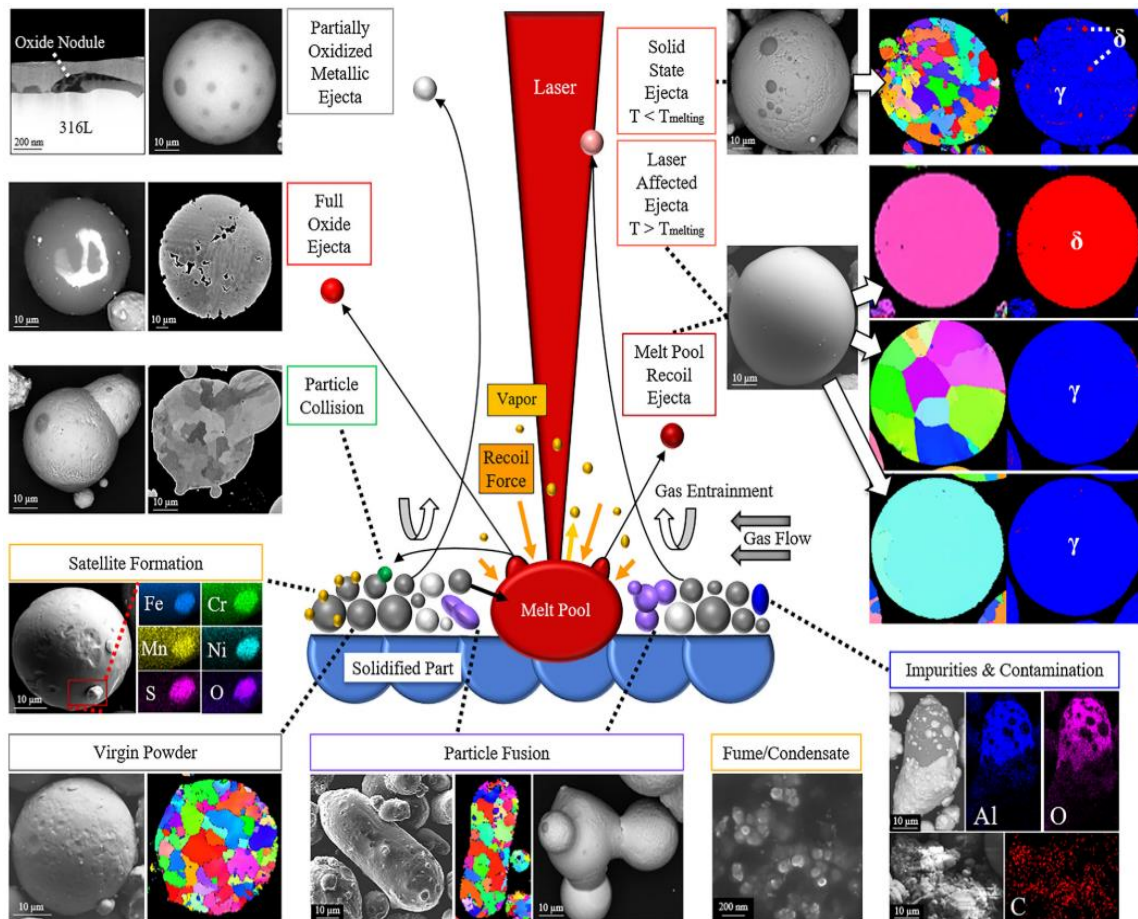
Figure 2.11 Summary of powder changes that 316L stainless steel experiences after being reused [74].

Particle size distribution (PSD)

The particle size distribution of 316L stainless steel changes at a rate that has not been reported as the number of reuses increases. It was commonly observed that the number of fine particles decreases at a higher number of reuses, but this change is not linear [73]. The Gaussian distribution curves tend to shift

to the bigger particle sizes. Heiden et al. [74] reported a study with 30 reuses obtaining a particle size distribution (PSD) D_{50} of 16.9 μm and 15.4 μm for virgin powder and reuse powder, respectively. PSD variations are reported to be below 80 μm as ≤ 200 mesh is commonly used in sieving.

Slight changes in particle size are challenging to associate with properties of the final components. Some of the repercussions of this variation may be easier to associate with defects during the laser process. For example, changes in the size and morphology of reused powder led to changes in flowability and spreadability. Consequently, these changes can influence the density and continuity of the layers deposited on the build plate. More specifically, finer particles in the feedstock will cause lower packing density within the layer and, therefore, lower bulk density in the final part, causing possible variations in the tensile strength, surface roughness, and fatigue life [75,76]. Discontinuous layers can also be caused by increased agglomerated and elongated powder that passes through a mesh. Defects reported by this powder condition include balling, porosity, and lack of fusion [70,72,74].

Chemical composition

During PBF-LB, powder can be contaminated during sieving when humidity conditions and oxygen atmosphere are not adequately regulated. When the powder is exposed to oxygen during the process, the oxygen tends to be entrapped inside the porosity of the particles [77] and/or coat the surface of the powder particles. In the case of spatter and condensate powder, a higher concentration of Si, Mn, Mo, and Cr oxides have been observed on the surface. During laser melting of particles with thick surface oxides, these oxides are not easily stirred into the melt pool. Oppositely, the oxide residues affect the surface tension destabilizing the melt pool. This can decrease surface wettability which favors the formation of defects such as porosity, lack of fusion, and balling due to improper layer fusion.

The maximum oxygen concentration observed in the powder reported in the literature after powder reuse using an inductively coupled plasma-mass-spectrometry technique was 0.095 wt.%, corresponding to a 28% increase to virgin powder [78]. Loss of alloying elements is also expected due to the vaporization caused in the plasma plume. The intensity of vapor pressure at the molten melt pool surface is higher than the surrounding environment pressure; thus, the surplus pressure drives vapor containing alloying elements to eject away from the surface [25]. For 316L stainless steel, nickel, manganese, and chromium concentrations tend to decrease, while silicon and molybdenum concentrations increase due to their higher boiling temperatures. However, powder reuse studies have shown that the amount of loss of alloying elements over a high number of reuse times does not cause the powder to be out of specification [74].

Spatter and Condensate powder

The heat-affected powder is known as spatter and condensate as they are formed under high-temperature conditions from the melt pool. Spatter is caused by (1) ejected particles from the powder bed by the vapor jet, (2) liquid metal ejected from the melt pool due to recoil pressure, and (3) metal vapor ejected (condensate powder). In the first case, solid particles blow away due to the heated cover gas that moves the powder out of the way [79]. In the second case, the melt pool experiences a high degree of superheating due to the strong laser beam density of $10^6 – 10^7$ W/cm^2. In addition to the high temperatures, the high vapor surface flux exerts a pressure force that ejects molten material from the surface, known as spatter. Moreover, the vaporized materials rapidly solidify, causing the formation of condensate powder.

The agglomerated powder is characteristic of reused powder, and this is related to the fusion of particles near the vicinity of the melt pool and spatter formation mechanisms. In the second case, when the metal droplets are ejected, they collide with each other or with cold particles from the regions with lower temperature gradients in the melt pool and its surroundings. Therefore, more significant, and irregular clusters are formed via coalescence or sintering [79]. The condensed powder can also be deposited on the surface of spatter and virgin powder, changing their surface chemical composition, and affecting the surface free energy leading to changes in spreadability and laser absorption. Gunenthiram et al. [80] reported ejection fractions between 10 % and 20%; however, further investigation is needed to prove the deleterious defects of such concentration. Overall, powder reuse studies lack quantitative data for the total volume of spatter and ejected material due to the challenge of delineating the irregular virgin powder from the heat-affected powder. In the case of 316L, the aspect ratio, particle size distribution, and chemical composition does not change significantly, which limits the quantification of the final volume of reused powder.

Spatter is an important feature as these particles can be deposited in the powder bed and remelted by the laser or reused in the subsequent builds if the spatter is small enough to pass through the sieving process. Spatter particles will affect the recoating stability, leading to uneven surfaces that affect the density of components, their microstructure, and, consequently, their mechanical properties [81].

Microstructure

Heat-affected powder differs chemically and microstructurally from virgin powder due to oxidation on the outer surfaces, remelting, and rapid solidification. However, microstructural changes in powder reusability are less described in the literature. The few reported sources [78,79] include internal porosity

34

measurements, a description of crystal structure (austenite to ferrite transformations), and the grain size of 316L stainless steel powder.

Internal porosity is present in virgin powder as gas is entrapped during solidification. In reused powder, it has been observed that internal porosity increases over time as the particles experience several cycles of remelting. However, Heiden et al. [74] reported the opposite in reused 316L powder in which the pore size and volume decreased. Thus, suggesting that pores collapse into smaller ones with thermal treatment or acquire lower porosity with reuse.

An increase in ferrite content has been observed when compared to virgin powder. Delacroix et al. reported that 316L presented almost 4% more ferrite content after 15 reuses [73]. Due to the low ferrite volume, phase transformation in powder reuse is not a major concern. However, it is recommended to monitor the powder as ferrite particles tend to have different microstructure (single phase) and magnetism that could cause agglomeration on the build plate, leading to voids in the printed parts [78]. Finally, average grain size is usually not commonly reported in reuse studies. However, Heiden et al. [74] reported a slight decrease in the average grain size of 316L from 4 μm in the virgin state to 3.3 μm in the reused state. The dissertation work herein will provide further quantitative grain size measurements in heat-affected particles.

2.2.4.4   Impact of reused powder on the manufactured components

The properties of reused powder can lead to the formation of defects through poor spreadability on the build plate, changes in the chemical composition and microstructure, and instabilities in the melt pool. Unfortunately, the powder feedstock always has a range of multiple properties that contribute simultaneously as possible sources of defects, which results in the understanding of the exact cause of failures to be limited. Additionally, the process plays an important role in forming defects; therefore, part anomalies and failures cannot yet be assigned solely based on reused powder conditions.

Powder-induced defects are not fully classified yet; however, it can be established that lack of fusion, gas porosity, surface roughness, balling, spatter, and metallurgical defects such as impurities, segregation, and loss of alloy elements can be categorized as the most critical defects caused by reused powder. Mostafaei et al. [79] explains each of these defects not in relation to the conditions of powder reuse but rather to the process. Other studies [73,82] reveal changes in the manufactured components after powder reuse for 316L stainless steel. The comparison of both process-defect and powder-defect studies is helpful to have a deeper understanding of the process-powder trends responsible for the defect and anomaly formation.

Moving forward in the study of powder reuse, process-structure-property correlations have been evaluated for different alloy systems. In the case of 316 L stainless steel, such correlations need further study as no statistically significant changes are reported in mechanical properties. Heiden et al. [74] reported that the ultimate tensile strength (UTS) and yield strength of 25 samples remained relatively constant within the standard deviation. However, a slight increase in elongation to failure was observed, from 43% in the virgin condition to 52% after thirty reuses. This minor change in ductility was attributed to the powder's particle size distribution, leading to improved spreadability over time and a better surface finish. The results are not enough evidence to confirm this statement; however, the variability in the data obtained at different build plate locations is suggested to be a more important factor than the powder characteristics. Delacroix et al. [73] also presented steady values for uniaxial tensile tests and microhardness regardless of the differences observed in the microstructures of the parts obtained across 15 reuses. Liu et al. [83] observed that the tensile properties of samples printed with reused powder are inferior as they showed a decrease of 25% in the UTS and a decrease of 53% in the elongation. In this case, similar to Delacroix's study, only three samples per build were tested. In contrast to the Delacroix and Heiden studies, the reused powder was not sieved, presenting more spatter and affecting the particle size distribution of the powder feedstock, which caused inhomogeneous melting conditions.

An alternate approach to clarify the impact of reused powder is to evaluate a large dataset of mechanical tests for any given condition. Considerations such as constant part geometry, laser parameters, and powder handling may need to be unchanged for validation purposes. The importance of this approach lies in the need for statistically validated data, as most prior studies rely on a small number of samples (less than 25 samples [73,74,83]) for tensile testing. Efficient high-throughput methods can be more accurate when integrating vision systems and software that allow for the acquisition of the temperature distribution in each layer, as well as the analysis of the data and the defect identification. With this approach, variation data between builds and powder qualification may be more reliable. Additionally, anomalous events can be statistically documented and less probable to be ignored, providing an easier path to link the impact of the powder condition as the number of powder reuse cycles progresses regardless of the exact powder characteristic that causes the defects is unknown.

Boyce et al. [84] developed a high-throughput tensile test method for additive manufactured 17-4 PH stainless steel components. Approximately 1000 tensile stress-strain curves were collected under nominally identical conditions and successfully linked to the 2% of the population that experienced premature failures due to lack of fusion. Further fractography analysis revealed a rare defect interconnected with the lack-of-fusion network. They observed a collection of overlapping pores responsible for forming a brittle interior coating, most likely contributing to premature failures. While this

36

study does not focus on the powder reuse effect, preliminary attempts to find correlations between property variation and underlying structure were performed more efficiently compared to the current powder reuse studies that selected small populations of samples.

2.3   References

1. Suryanarayana, C. (2001). Mechanical alloying and milling. Progress in Materials Science, 46(1–2), 1–184. https://doi.org/10.1016/S0079-6425(99)00010-9

2. Suryanarayana, C. (2022). Mechanical alloying: a critical review. Materials Research Letters, 10(10), 619–647. https://doi.org/10.1080/21663831.2022.2075243

3. Huang, M., Jiang, J., Wang, Y., Liu, Y., Zhang, Y. (2022). Effects of milling process parameters and PCAs on the synthesis of Al0.8Co0.5Cr1.5CuFeNi high entropy alloy powder by mechanical alloying. Materials & Design, 217, 10637. https://doi.org/10.1016/j.matdes.2022.110637.

4. AlMangour, B., Grzesiak, D., & Yang, J.-M. (2017). Selective laser melting of TiB2/316L stainless steel composites: The roles of powder preparation and hot isostatic pressing post-treatment. Powder Technology, 309, 37–48. https://doi.org/10.1016/j.powtec.2016.12.073

5. Toozandehjani, M., Matori, K. A., Ostovan, F., Aziz, S. A., & Mamat, M. S. (2017). Effect of milling time on the microstructure, physical and mechanical properties of Al-Al2O3 nanocomposite synthesized by ball milling and powder metallurgy. Materials, 10(11). https://doi.org/10.3390/ma10111232

6. Zhai, W., Zhou, W., Nai, S. M. L., & Wei, J. (2020). Characterization of nanoparticle mixed 316 L powder for additive manufacturing. Journal of Materials Science and Technology, 47, 162–168.

7. Suryanarayana, C. (2019). Mechanical Alloying: A Novel Technique to Synthesize Advanced Materials. Research, 2019, 4219812. https://doi.org/10.34133/2019/4219812

8. Joy, J., Krishnamoorthy, A., Tanna, A., Kamathe, V., Nagar, R., Srinivasan, S. (2022). Recent Developments on the Synthesis of Nanocomposite Materials via Ball Milling Approach for Energy Storage Applications. Applied Sciences, 12(18), 9312. https://doi.org/10.3390/app1218931

9. Banerjee, S., Mukhopadhyay, P. (2007). Solidification, Vitrification, Crystallization and Formation of Quasicrystalline and Nanocrystalline Structures. Pergamon Materials Series, 12, 125-255. https://doi.org/10.1016/S1470-1804(07)80056-3.

10. Xun, Y., Mohamed, F. A., & Lavernia, E. J. (2004). Synthesis of nanocrystalline Zn-22 Pct Al using cryo milling. Metallurgical and Materials Transactions A, 35(2), 573–581. doi:10.1007/s1661-004-0368-1

11. Salur, E., Aslan, A., Kuntoğlu, M., & Acarer, M. (2021). Effect of ball milling time on the structural characteristics and mechanical properties of nano-sized Y2O3 particle reinforced aluminum matrix composites produced by powder metallurgy route. Advanced Powder Technology, 32(10), 3826–3844. doi:10.1016/j.apt.2021.08.031

12. Zhang, D., Guan, L. (2014). Laser Ablation. Editor(s): Hashmi, S., Ferreira G., Van Tyne, C., Yilbas, B. Comprehensive Materials Processing, Elsevier, 125-169. https://doi.org/10.1016/B978-0-08-096532-1.00406-4.

13. Semaltianos, N.G. (2016). Nanoparticles by Laser Ablation of Bulk Target Materials in Liquids. In: Aliofkhazraei, M. (eds) Handbook of Nanoparticles. Springer, Cham. https://doi.org/10.1007/978-3-319-15338-4_1

14. F. Mafuné, K. Miyajima, Sobhan M. Ahmed. (2013). Physical preparation of nanoalloys. Editor: Calvo, F. Nanoalloys From Fundamentals to Emergent Applications, Elsevier, Waltham, 39–74.

15. Xiao, J., Liu, P., Wang, P., & Yang, G. (2017). External field-assisted laser ablation in liquid: an efficient strategy for nanocrystal synthesis and nanostructure assembly. Progress in Materials Science. 140–220.

16. Carpene, E., Höche, D., & Schaaf, P. (2010). Fundamental of Laser-Materials Interactions. Laser Processing of Materials, 21-47. doi:10.1007/978-3-642-13281-0

17. Philip, A. (1987). Theory of thermal relaxation of electrons in metals. Physics Review Letter, 59, 1460. https://doi.org/10.1103/PhysRevLett.59.1460

18. Carpene, E., Höche, D., Schaaf, P. (2010). Fundamentals of Laser-Material Interactions. In: Schaaf, P. (eds) Laser Processing of Materials. Springer Series in Materials Science, vol 139. Springer, Berlin, Heidelberg. https://doi.org/10.1007/978-3-642-13281-0_3

19. Gamaly, E., Rode, A., & Luther-Davis, B. (2002). Ablation of solids by femtosecond lasers: Ablation mechanism and ablation thresholds for metals and dielectrics. Physics of Plasmas, 949– 957.

20. Tsuji, T., Okazaki, Y., Tsuboi, Y., & Tsuji, M. (2007). Nanosecond time-resolved observations of laser ablation of silver in water. Japanese Journal of Applied Physics, 46, 1533

21. Kiran, K., Samuel, G.L., & Shunmugam, M.S. (2019). Theoretical and experimental investigations of ultra-short pulse laser interaction on Ti6Al4V alloy. Journal of Materials Processing Technology, 263, 266-275.https://doi.org/10.1016/j.jmatprotec.2018.08.028

22. Li, X.; & Guan, Y. (2020). Theoretical fundamentals of short pulse laser–metal interaction: A review. Nanotechnology and Precision Engineering, 3, 105–125

23. Gamaly, E. G., & Rode, A. V. (2013). Physics of ultra-short laser interaction with matter: From phonon excitation to ultimate transformations. Progress in Quantum Electronics, 37(5), 215–323. https://doi.org/10.1016/j.pquantelec.2013.05.001

24. ASTM International. (2015). ISO/ASTM52900-15 Standard Terminology for Additive Manufacturing - General Principles – Terminology.

25. Narasimharaju, S. R., Zeng, W., See, T. L., Zhu, Z., Scott, P., Jiang, X., & Lou, S. (2022). A comprehensive review on laser powder bed fusion of steels: Processing, microstructure, defects and control methods, mechanical properties, current challenges and future trends. Journal of Manufacturing Processes, 75, 375–414. https://doi.org/10.1016/J.JMAPRO.2021.12.033

26. Tang, M., Pistorius, P.C., & Beuth, J.L. (2017). Prediction of lack-of-fusion porosity for powder bed fusion. Additive Manufacturing, 14, 39–48. https://doi.org/10.1016/j. addma.2016.12.001.

27. Mostafaei, A., Zhao, C., He, Y., Reza Ghiaasiaan, S., Shi, B., Shao, S., Shamsaei, N., Wu, Z., Kouraytem, N., Sun, T., et al. (2022). Defects and anomalies in powder bed fusion metal additive manufacturing. In Current Opinion in Solid State and Materials Science (Vol. 26, Issue 2).

28. Korner, C., Bauereiß, A., & Attar, E. (2013). Fundamental consolidation mechanisms during selective beam melting of powders, 21(8), 85011.

29. Kurz, W., % Fisher. DJ. (1998). Fundamentals of solidification. Switzerland: CRC Press, 4, 1998.

30. Wang, H., Wang X. H, Zhang, H., Du, X., Li, W., & Tao, K. (2007). Synthesis of Bulk and Supported Molybdenum Carbide by a Single-Step Thermal Carburization Method. Chemistry of Materials, 1801-1807. 7

31. Du, J., Wu, J., Guo, T., Zhao, R., & Li, J. (2014). Catalytic performance of Mo2C supported on onion-like carbon for dehydrogenation of cyclohexane. RSC advances, 4, 53950–53953. 8.

32. Hugosson, H., Eriksson, O., & Lars, N. (1999). Theory of phase stabilities and bonding mechanisms in stoichiometric and substoichiometric molybdenum carbide. J. Appl. Phys., 86(7), 3758-3767.

33. Zhang, S., Wang, C., Qiu, H., Bao, H., Long, T., et al. (2020). Highly graphitic carbon shell on molybdenum carbide nanosheets by iron doping for stable hydrogen evolution. International Journal of Hydrogen Energy, 45 (28), 14368-14374.

34. White, J., & Pontelandolfo, J. (966). Graphite-Carbide Materials Prepared by Hot-Working with the Carbide Phase in the Liquid State. Nature, 209, 1018-1019.

35. White, J., & Pontelandolfo, J. (1966). Graphite-Carbide Materials Prepared by Hot Working with a Dispersed Liquid-Carbide Phase. Carbon, 4, 305-314.

36. Harada, Y. (1966). Feasibility of fabricating graphite-metal carbide composites of high density and strength by hot pressing. Website: NASA Technical Reports Server: https://ntrs.nasa.gov/search.jsp?R=19660019930

37. John, D., & Jenkins, G. (1986). Hot-working and strengthening in metal carbide-graphite composites. J. Mater. Sci., 21, 2941 2958

38. Bertarelli, A. (2015). Innovative MoC-graphite composite for thermal management and thermal shock applications. 31st Thermal Measurement, Modeling & Management Symposium (SEMI-THERM), San Jose, CA, 56-59.

39. Simos, N., Zhong, Z., Ghose, S., Kirk, H., Trung, L.-P., McDonald, K., et al. (2016). Radiation damage and thermal shock response of carbon-fiber-reinforced materials to intense high-energy proton beams. Phys. Rev. Accel. Beams, 19, 111002.

40. Liang, J., Chen, S., Xie, M., Wang, Y., Guo, X., Guo, X., $ Ding, W. (2014). Expeditious fabrication of flower-like hierarchical mesoporous carbon superstructures as supercapacitor electrode materials. Journal of Materials Chemistry A, 2, 16884−16891

41. Xia, Z., Shen, Y., Shen, J., & Li, Z. (2008). Mechanosynthesis of molybdenum carbides by ball milling at room temperature. J. Alloys. Compd., 453, 185-190.

42. Cheng, P., Ouyang, L., Lang, C., Zhong, H., Liu, J., Wang, H., et al. (2023). All-pH Hydrogen Evolution by Heterophase Molybdenum Carbides Prepared via Mechanochemical Synthesis. ACS Sustainable Chem. Eng

43. Quiroz, J., Frigini Mai, E., & Teixeira da Silva, V. (2016). Synthesis of Nanostructured Molybdenum Carbide as Catalyst for the Hydrogenation of Levulinic Acid to y-Valerolactone. Topics in Catalysis, 148-158. doi:10.1007/s11244-015-0433

44. Bokhonov, B., Borisova, Y., & Korchagin, M. (2004). Formation of encapsulated molybdenum carbide particles by annealing mechanically activated mixtures of amorphous carbon with molybdenum. Carbon, 42, 2067-2071.

45. Sarathi, R., Reddy, R., Tavarmani, R., Okamoto, A., Suematsu, H., Selvam, P., et al. (2015). Investigation of Nano-Molybdenum Carbide Particle Produced by WireExplosion Process. IEEE Transactions on Plasma Science, 3470-3475. Doi:10.1109/tps.2015.2426019

46. Zou, Q., Wang, M., Li, Y., & Zhao, Y. (2010). HRTEM and Raman characterization of the onion-like carbon synthesized by annealing detonation nanodiamond at lower temperature and vacuum. Journal of Experimental Nanoscience, 473–487. doi:10.1080/17458081003646982

47. Krüger, A. (2010). Carbon Onions and Related Materials. En A. Krüger, Carbon Materials and Nanotechnology (pag. 284). Weinheim: WILEY-VCH.

48. Omori, T., Sato, J., Shinagawa, K., Ohnuma, I., Oikawa, K., Kainuma, R., & Ishida, K. (2014). Experimental determination of phase equilibria in the Co-Cr-Ni system. Journal of Phase Equilibria Diffusion ,35, 178-185.

49. Yamanaka, K., Mori, M., Ohmura, K., & Chiba, A. (2016). Preventing high-temperature oxidation of Co-Cr-based dental alloys by boron doping. Journal of Materials Chemistry B, 4, 309-317

50. Sahoo, P., Das, S. K., & Paulo Davim, J. (2019). Tribology of materials for biomedical applications. Mechanical Behavior of Biomaterials, 1–45

51. Mostafaei, A., Gordon, J. V., & Rollett, A. D. (2020). Additive Manufacturing of Cobalt Alloys. Additive Manufacturing Processes, 24(Ref 32), 374–379.

52. Kashani, H., Amadeh, A., & Ohadizadeh, A. (2006). Effect of temperature on the strain induced phase transformation in Stellite during wear test. Materials Science Engineering A, 435-436

53. Crook, P. (2012). Co-Based alloys. ASM Handbook.

54. Matsumoto, H., Koizumi, Y., Ohashi, T., Lee, B.S., Li, Y., & Chiba, A. (2014). Microscopic mechanism of plastic deformation in a polycrystalline Co-Cr-Mo alloy with a single hcp phase. Acta Materialia, 64, 1–11, https://doi.org/10.1016/j. actamat.2013.11.005.

55. Matsumoto, H., Kurosu, S., Lee, B.S., Li, Y., & Chiba, A. (2010). Deformation mode in biomedical Co–27% Cr–5% Mo alloy consisting of a single hexagonal close-packed structure. Scripta Materialia, 63, (11), 1092-1095. https://doi.org/10.1016/j.scriptamat.2010.08.006.

56. Mengucci, P., Barucca, G., Gatto, A., Bassoli, E., Denti, L., Fiori, F., et al. (2016). Effects of thermal treatments on microstructure and mechanical properties of a Co-Cr-Mo-W biomedical alloy produced by laser sintering. Journal Mechanical Behavior of Biomedical Materials, 60, 106–117

57. Kosuke, U., Yuto, K., Shingo, M., Alfirano, K. U., Shigenobu, N., et al. (2016). Changes in Microstructure of Biomedical Co-Cr-Mo Alloys during Aging at 973 to 1373 K. Materials Transactions, 57 (12) 2048-2053. https://doi.org/10.2320/matertrans.MI201507

58. Li, K., Wang, Z., Song, K., Khanlari, K., Yang, X.-S., Shi, Q., Liu, X., & Mao, X. (2022). Additive manufacturing of a Co-Cr-W alloy by selective laser melting: In-situ oxidation, precipitation and the corresponding strengthening effects. Journal of Materials Science & Technology, 125, 171–181.

59. Martin, J., Yahata, B., Hundley, J., et al. (2017). 3D printing of high-strength aluminium alloys. Nature, 549, 365-369.

60. Li, X., Ji, G., Chen, Z, et al. (2017). Selective laser melting of nano-TiB2 decorated AlSi10Mg alloy with high fracture strength and ductility. Acta Materialia, 129, 183-193.

61. Chao, M., Lianyi, C., Chezheng, C., Xiaochun, L. 2016. Nanoparticle-induced unusual melting and solidification behaviours of metals. Nature. 8:14178

62. DebRoy, T., Wei, H.L., Zuback, J.S., Mukherjee, T., Elmer, J.W., et al. (2018). Additive manufacturing of metallic components – process, structure and properties. Progress in Materials Science, 92, 112–224. https://doi.org/10.1016/j.pmatsci.2017.10.001

63. Giacovazzo, C., Monaco, H.L., Artioli, G., Viterbo, D., Ferraris, G., & Giacovazzo, C. (2002). Fundamentals of Crystallography, Oxford University Press.

64. Zhang, D., Prasad, A., Bermingham, M. J., Todaro, C. J., Benoit, M. J., et al. (2020). Grain Refinement of Alloys in Fusion-Based Additive Manufacturing Processes. Metallurgical and Materials Transactions A: Physical Metallurgy and Materials Science, 51(9), 4341–4359.

65. Tan, Q., Yin, Y., Prasad, A., Li, G., Zhu, Q., StJohn, D. H., & Zhang, M. X. (2022). Demonstrating the roles of solute and nucleant in grain refinement of additively manufactured aluminium alloys. Additive Manufacturing, 49(August 2021), 102516.

66. Russell, K.C. (1969). Grain boundary nucleation kinetics, Acta Meterialia, 17, 1123–1131.

67. Sabzi, H. E., Hernandez-Nava, E., Li, X. H., Fu, H., San-Martín, D., & Rivera-Díaz-del-Castillo, P. E. J. (2021). Strengthening control in laser powder bed fusion of austenitic stainless steels via grain boundary engineering. Materials and Design, 212.

68. Moghimian, P., Poirié, T., Habibnejad-Korayem, M., Zavala, J. A., et al. (2021). Metal powders in additive manufacturing: A review on reusability and recyclability of common titanium, nickel, and aluminum alloys. Additive Manufacturing, 43, 102017.

69. Okello, A., Samper, V., & Additive, G. E. (2021). Powder Reuse White Paper Effective Powder Reuse Strategies Effective Powder Reuse Strategies. 1–14.

70. Powell, D., Rennie, A. E. W., Geekie, L., & Burns, N. (2020). Understanding powder degradation in metal additive manufacturing to allow the upcycling of recycled powders. Journal of Cleaner Production, 268, 122077. https://doi.org/10.1016/J.JCLEPRO.2020.122077

71. Derimow, N., & Hrabe, N. (2021). Oxidation in Reused Powder Bed Fusion Additive Manufacturing Ti-6Al-4V Feedstock: A Brief Review. JOM, 73(11), 3618–3638

72. Lu, C., Zhang, R., Xiao, M., Wei, X., Yin, Y., et al. (2022). A comprehensive characterization of virgin and recycled 316L powders during laser powder bed fusion. Journal of Materials Research and Technology, 18, 2292–2309

73. Delacroix, T., Lomello, F., Schuster, F., Maskrot, H., & Garandet, J.-P. (2022). Influence of powder recycling on 316L stainless steel feedstocks and printed parts in laser powder bed fusion. Additive Manufacturing, 50, 102553.

74. Heiden, M. J., Deibler, L. A., Rodelas, J. M., Koepke, J. R., et al. (2019). Evolution of 316L stainless steel feedstock due to laser powder bed fusion process. Additve Manufacturing, 25, 84–103

75. Spierings, A. B., Herres, N., & Levy, G. (2011). Influence of the particle size distribution on surface quality and mechanical properties in AM steel parts. Rapid Prototyping Journal, 17(3), 195–202.

76. Greitemeier, D., Dalle Donne, C., Syassen, F., Eufinger, J., & Melz, T. (2016). Effect of surface roughness on fatigue performance of additive manufactured Ti–6Al–4V. Materials Science and Technology, 32(7), 629–634.

77. Simonelli, M., Tuck, C., Aboulkhair, N. T., Maskery, I., Ashcroft, I., et al. (2015). A Study on the Laser Spatter and the Oxidation Reactions During Selective Laser Melting of 316L Stainless Steel, Al-Si10-Mg, and Ti-6Al-4V. Metallurgical and Materials Transactions A: Physical Metallurgy and Materials Science, 46(9), 3842–3851.

78. Douglas, R., Lancaster, R., Jones, T., Barnard, N., & Adams, J. (2022). The Influence of Powder Reuse on the Properties of Laser Powder Bed-Fused Stainless Steel 316L: A Review. Advanced Engineering Materials, 2200596

79. Mostafaei, A., Zhao, C., He, Y., Reza Ghiaasiaan, S., et al. (2022). Defects and anomalies in powder bed fusion metal additive manufacturing. In Current Opinion in Solid State and Materials Science (Vol. 26, Issue 2). Elsevier Ltd.

80. Gunenthiram, V., Peyre, P., Schneider, M., Dal, M., Gunenthiram, V., et al. (2017). Analysis of laser – melt pool – powder bed interaction during the selective laser melting of a stainless steel To cite this version: HAL Id: hal-01664637.

81. Wang, D., Wu, S., Fu, F., Mai, S., Yang, Y., Liu, Y., & Song, C. (2017). Mechanisms and characteristics of spatter generation in SLM processing and its effect on the properties. Materials & Design, 117, 121–130.

82. Sutton, A. T., Kriewall, C. S., Karnati, S., Leu, M. C., & Newkirk, J. W. (2020). Characterization of AISI 304L stainless steel powder recycled in the laser powder-bed fusion process. Additive Manufacturing, 32, 100981

83. Liu, Y., Yang, Y., Mai, S., Wang, D., & Song, C. (2015). Investigation into spatter behavior during selective laser melting of AISI 316L stainless steel powder. Materials & Design, 87, 797–806.

84. Boyce, B. L., Salzbrenner, B. C., Rodelas, J. M., Swiler, L. P., et al. (2017). Extreme-Value Statistics Reveal Rare Failure-Critical Defects in Additive Manufacturing. Advanced Engineering Materials, 19(8), 1700102.

CHAPTER 3
MoC@C CORE-SHELL NANOPARTICLES SYNTHESIZED BY
LASER ABLATION IN LIQUID

3.1   Abstract

Laser ablation of metal in liquid is an efficient technique to synthesize metal or metal carbide core−shell nanoparticles. Due to the high complexity of synthesizing transition metal carbide nanoparticles, we attempted to produce MoC via one-step synthesis by irradiating a Mo target in toluene as an effective method, however, no core-shell structures were observed. To form core-shell structures extra carbon was created via the ablation of a graphite target prior to ablation of the Mo target, and as a result, onion-like carbon structures (OLC) were obtained. The applied laser energy densities were observed to affect the properties of these heterostructures, and therefore the effects of different pulse durations on heterostructure formation were evaluated. The findings reveal the fundamental mechanisms involved in the formation of the core-shell MoC nanoparticles.

3.2   Introduction

Laser ablation in liquid (LAL) is one of the fastest and most efficient techniques for the synthesis of nanoparticles (NPs). This method does not require long reaction times, high temperatures, pressures, or multi-step chemical procedures compared to chemical synthesis, vapor deposition, and wet chemistry [1]. Precursors or stabilizers such as ligands or surfactants are unnecessary since it is possible to control the particle size distribution using only the liquid medium. As a result, high purity and low or negligible chemical waste can be achieved.

LAL facilitates the synthesis of nanoparticles with complex stoichiometries and heterostructures. The latter is possible as in situ functionalization is allowed due to the easy addition of ligands and interaction among the reactive species from the solvent with the material ablated [2]. Functionalizing the NPs can also be implemented as a solution to avoid their oxidation or reaction in aggressive environments. Another alternative to prevent oxidation is encapsulating the NPs in situ during the ablation process [3]. Carbon coatings have been reported to be a viable and efficient option when using hydrocarbon liquids [4,5]. Due to the elevated temperatures and pressures within the plasma plume, it is possible to form different carbon allotropes. The most reported structures are onion-like carbon (OLC) or polyhedral onion-like carbon structures. These graphitic structures form multiple layers on top of each other and interact by van der Waals forces [6]. Core/shell nanostructures have attracted increasing interest due to

their remarkable physical-chemical properties such as electrical and tribological properties [7] that leads to applications in the field of energy storage, lubrication, catalysis, and photovoltaic cells [6,7].

Carbide materials can be synthesized by taking advantage of the thermochemical decomposition (pyrolysis) of hydrocarbon liquids at low oxygen concentrations. The synthesis of carbides by LAL, especially molybdenum carbides, has not been extensively studied. Due to its outstanding catalytic properties [8], this is an important system to be explored.

When ablating a molybdenum target inside a hydrocarbon liquid, the solvent can offer carbon resources for reactions to form carbides and graphitic coatings around the NPs. This is possible as the excited species within the cavitation bubble serve as nucleation sites to form carbide-graphite core-shell nanoparticles [4]. This process has been reported to be affected by the laser parameters, atmosphere, and irradiation time [9]. Therefore, this work evaluated the effect of short (6×10^{-9} s) and ultra-short pulses (3×10^{-11} s) to understand better how different fluences and irradiation times impact the formation of these core-shell nanostructures. Additionally, the particle size distribution, morphology, and crystallographic phases were assessed as a function of pulse duration.

3.3   Methodology

3.3.1   Laser ablation

Ablation in liquid experiments has been carried out by two Nd:YAG laser sources with short and ultra-short pulses. A Continuum laser (Surelite, Minilite II) was used for short pulses, and a Satsuma laser for ultra-short pulses. The parameters' specifications are described in Table 3.1 and Table 3.2. Two different solid targets of Mo and Graphite from Kurt J. Lesker with 99% purity were used. Isopropanol, ethyl acetate, and toluene were the solvents selected as the liquid media. As shown in Figure 3.1, the ablation process was done through a glass container with an incident angle of approximately 45 degrees, approximately. The ablation was performed with a nitrogen atmosphere.

The synthesis of MoC NPs was performed in sequence. Initially, only a Mo target was irradiated in the three solvents. However, due to the lack of formation of OLC shells around the NPs, extra carbon was added to the liquid by irradiating a graphite target. Both targets were inserted into the glass container. However, they were irradiated separately. First, the graphite target was irradiated for 3 minutes to form carbon NPs. Subsequently, the Mo target was irradiated for 5 minutes to form the MoC@C core-shell NPs.

To recover the NPs as powder, the excess solvent was evaporated inside a gas extraction chamber. Subsequently, the NPs were washed twice with ethanol through continuous sonication for 1 minute. The

suspension obtained was centrifuged for 15 minutes at 12,000 rpm. Lastly, the NPs were dried at room temperature, and the powder was characterized.

3.3.2   Characterization techniques

High-resolution TEM (HRTEM) was performed to assess the size distribution, morphology, and chemical composition of the NPs. The equipment used was a JEOL-2100 with 200 kV acceleration voltage and LaB_6 filament. At least five representative images were taken for each sample. Particle size distribution (PSD) was measured using Image J software. Raman spectroscopy (LabRam HR 800) was implemented to study the carbon coating and identify possible oxides. The system was equipped with a He-Ne laser source with a wavelength of 632.8 nm, an 800 mm focal spectrometer, and 1800 grooves/mm grating. The powders analyzed were placed in a glass holder and green compressed to form a uniform and flat layer.

Table 3.1 Laser parameters selected for each laser source.

Parameter	Laser Source	
	Short pulse laser	Ultra-short pulse laser
Wavelength (nm)	1064	1064
Pulse duration (s)	$6x10^{-9}$	$3x10^{-11}$
Frequency (Hz)	10	10
Spot Size (mm)	2	0.93

Table 3.2 Ablation parameters were selected for graphite and molybdenum targets.

Parameter	Short pulse laser		Ultra-short pulse laser	
	Graphite	Molybdenum	Graphite	Molybdenum
Ablation time (min)	3	5	3	5
Energy (mJ)	25	50	25	50
Irradiance (W/cm^2)	$6.13x10^8$	$1.23x10^9$	$2.65x10^{10}$	$5.31x10^{10}$
Fluence (J/cm^2)	3.68	7.36	0.79	1.59
Solvent volume (ml)	10	10	10	10
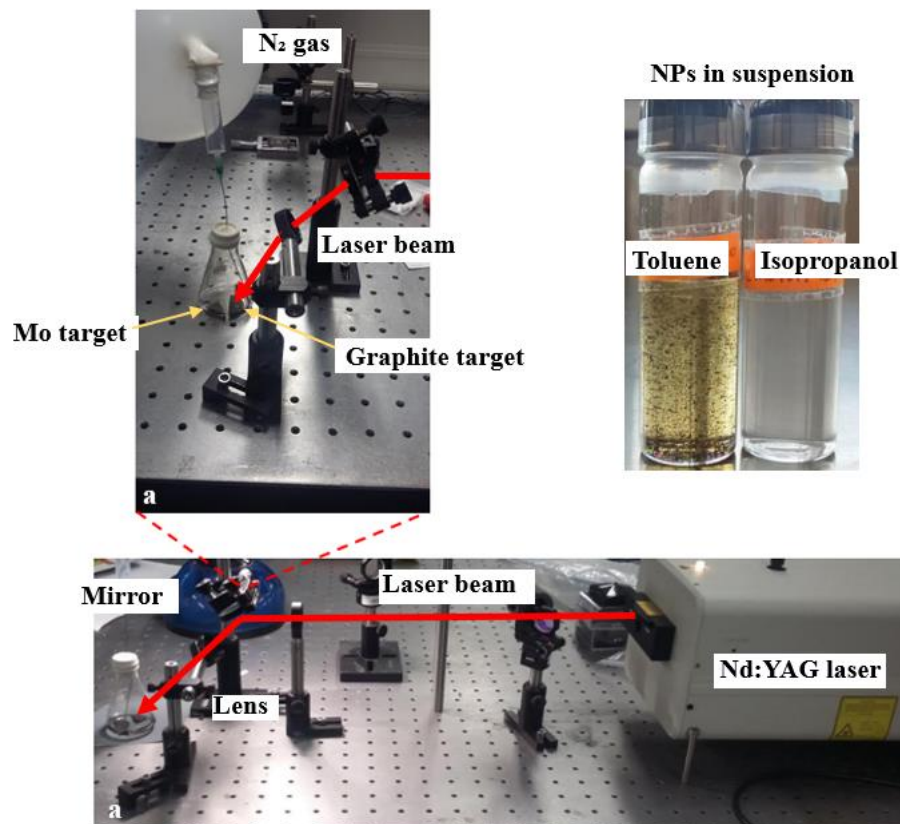
Figure 3.1 Experimental setup for ablation of graphite and molybdenum targets.

3.4 Results and Discussion

3.4.1 Selection of liquid medium

Various solvents were tested to evaluate which one allows a PSD closer to a Gaussian distribution, no agglomeration, and the formation of OLC. Initially, molybdenum was the only target ablated (no graphite ablation was performed) with various liquid mediums, such as isopropanol, toluene, and ethyl acetate. Angela et al. [5] demonstrated that bare carbide and core-shell carbide nanostructures were obtained using similar solvents.

Figure 3.2. and Figure 3.3 shows that none of the selected solvents completely eliminated the agglomeration of the NPs. Among the three systems, isopropanol is known to provide the best PSD, followed by toluene, however, the agglomeration was higher compared to the other solvents. Polarity, boiling point, and solvent volatility contribute to the NP agglomeration. If the polarity index is high, the NPs tend to agglomerate more. All solvents tested have similar polarity nominally between 4.3 and 4.5, approximately and similar volatility, therefore other properties need to be considered to explain the differences observed in agglomeration. Density, thermal conductivity, and liquid absorption are other

47

factors that contribute to PSD and agglomeration, however, the evaluation of these properties was not assessed in this work. The formation of oxides in isopropanol and ethyl acetate caused both solvents to be discarded from the investigation. The oxidation might have occurred due to residual oxygen in the atmosphere and from the rupture of C-O bonds in the solvent.

Figure 3.2c shows high-resolution micrograph of the oxides obtained. The indexing of the micrograph reveals the likely presence of MoO_2, whose reflections correspond to the (111), (022), and (200) planes obtained from JCPDS card No. 72-0671. In the case of MoO_3, the indexed plane corresponded to (060), obtained from JCPDS card No. 65-2421. Regarding the SAED diffraction pattern (Figure 3.2d), the observed rings correspond to the (111), (501), and (711) planes of MoO_3. (JCPDS #65-2421, #75-0912). Figure 3.2g shows the presence of MoO_2 with a (111) plane obtained from JCPDS card No. 86-0135. In the case of its diffraction pattern (Figure 3.2 h), the rings were assigned to MoO_3 with the planes (011), (600), (212), and (10 0 0), obtained from JCPDS card No. 75-0912.
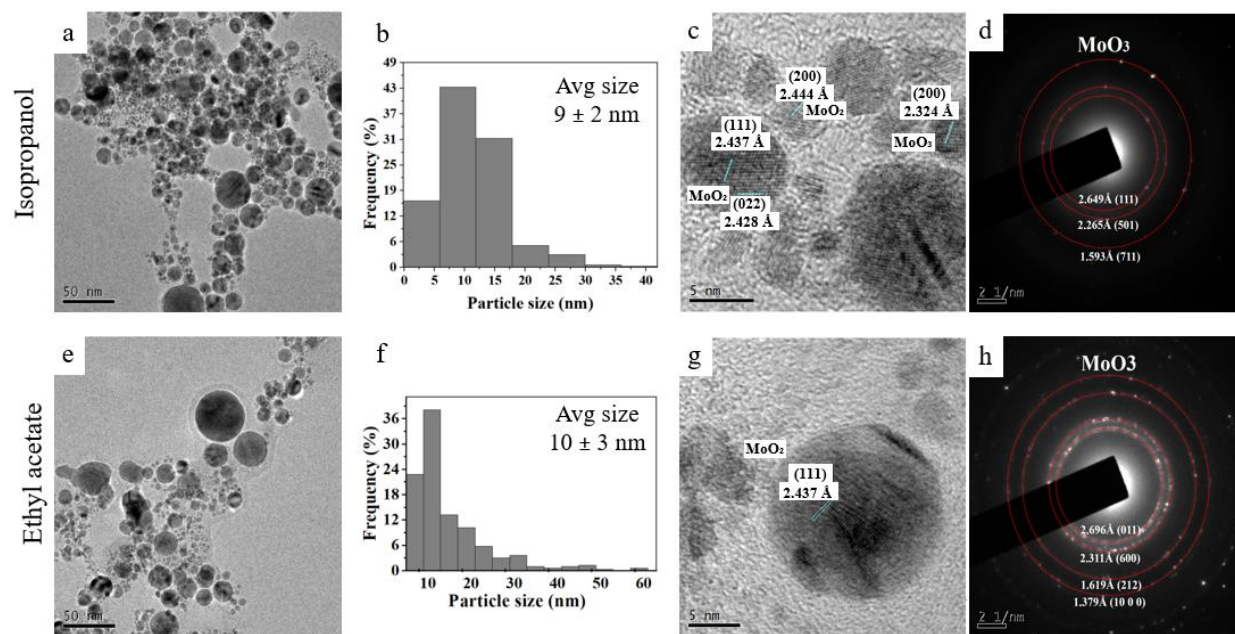
Figure 3.2 NPs obtained from the ablation of the Mo target in isopropanol (a-d) and ethyl acetate (e-h). Particle size distribution, morphology, and composition are indicated for each solvent. The average size and standard deviation are also indicated.

Toluene was selected as a hydrocarbon liquid with no oxygen in its chemical composition and to avoid the oxidation of the NPs. Figure 3.3 shows the result of the ablation of the Mo target without graphite under the same conditions as the two cases described in Figure 3.2. The composition of the synthesized NPs corresponds to MoC, and more precisely, the cubic phase δ-MoC (JCPDS #03-065-8092). No oxides

were observed. Although the synthesis of MoC in toluene was successful, the carbon coating was not uniform around the NPs. It can be deduced that the carbon coming from the decomposition of the solvent was insufficient to form OLC structures. For this reason, the additional step of ablating a graphite target was implemented.
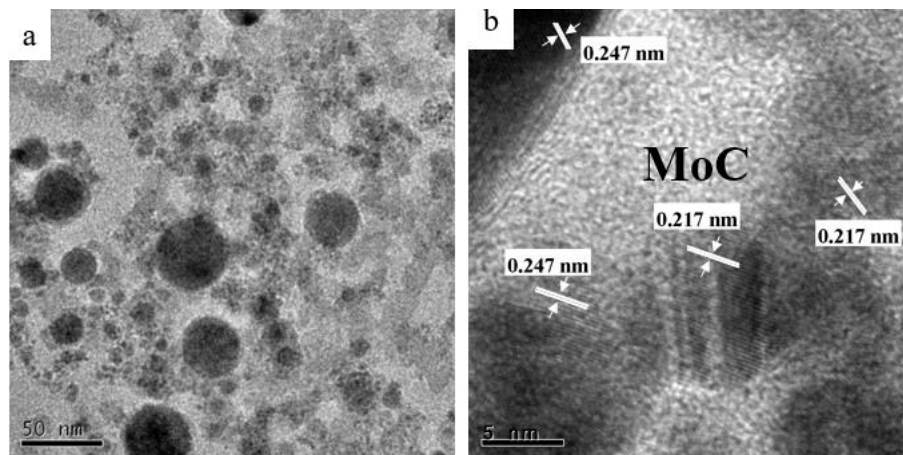
Figure 3.3 Nanoparticles obtained from the ablation of the Mo target in toluene. a) shows the PSD and morphology of the NPs. b) HRTEM image shows the presence of MoC. No oxides were observed.

3.4.2   Synthesis of MoC NPs with ultra-short and short pulses

With ultra-short pulses, the particle size distribution was narrower within a range of 1 – 29 nm and an average size of 6 nm (Figure 3.4a) compared to short pulses. The size range of NPs synthesized with longer pulses was within 1 – 49 nm with an average size of 11 nm (Figure 3.4b). This difference is attributed to different factors related to electron and lattice responses of the material ablated. In a short-pulse duration, a higher thermal effect predominates due to shorter relaxation times between pulses [10]. This phenomenon causes a substantial melting of the target, releasing larger particles due to explosive boiling effects. With short pulses, the cavitation bubbles have more time to grow, favoring more nucleation processes and more significant growth of the particles [11]. In contrast to ultrashort pulses, the thermalization of the lattice is low or nonexistent. In this case, the absorbed laser energy is limited only to the point of focus, thus generating no dissipation of energy into heat, resulting in an ablation process by a transition from solid to vapor without going through the liquid. This dynamic will cause more controlled growth of NPs as the ejected species will have similar cooling rates as the relaxation times between pulses are longer.
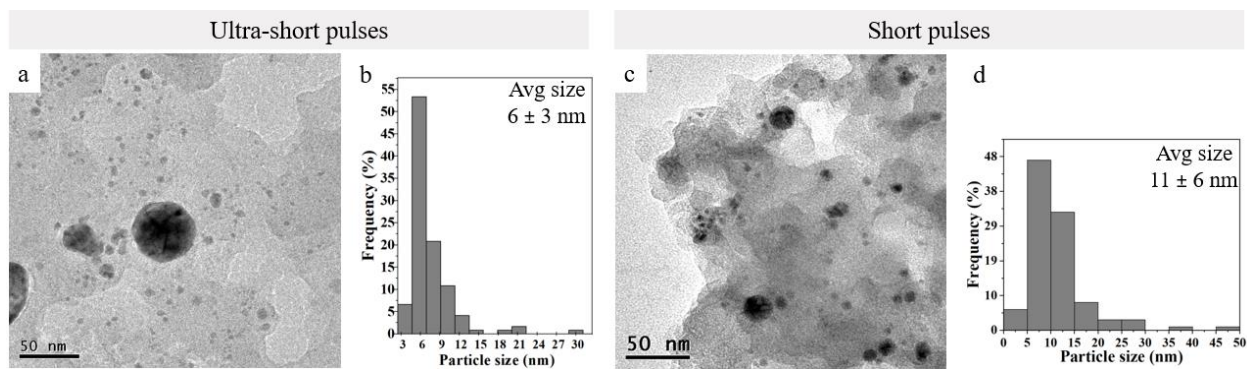
Figure 3.4 a-c) TEM micrographs of the MoC NPs synthesized with ultra-short and short pulses. An amorphous carbon matrix was observed in all the samples analyzed. b-d) Histogram of PSD. The average size and standard deviation are also indicated.

To decompose a liquid during laser ablation, it must be irradiated with a fluence above its breakdown threshold. It has been reported that high power densities of about 10^8 W/cm^2 are necessary [12]. If the liquid is irradiated above this limit, a multiphoton absorption avalanche mechanism occurs. This mechanism consists of inelastic collisions of electrons from the molecules and atoms. At higher fluences, more collisions occur. With ultra-short and short pulse laser, the calculated density fluences when the graphite target was ablated were 2.65×10^{10} W/cm^2 and 6.13×10^8 W/cm^2, respectively. From these values, toluene was expected to decompose more with ultra-short pulses, thus causing the generation of a higher volume of carbon structures. However, the opposite was observed. This can be followed in Figure 3.4c, where a thicker matrix of amorphous carbon coated the NPs. The formation of a thicker carbon matrix is likely due to the combination of a high energy density and a higher thermal effect due to a longer pulse duration. In this case, the solvent is not only decomposed by the localized interactions with the electron and phonon of the laser beam, but also caused by the higher heat dissipation in the rest of the solvent, which increases its temperature, causing thermal decomposition. This mechanism will cause the formation of more carbon species.

To confirm that the matrix was amorphous, TEM-SAED was performed within the area enclosed in Figure 3.5, and Raman spectroscopy was performed on the powders (Figure 3.6). In Figure 3.5, it can be observed that no diffraction pattern was detected; instead, only a diffuse region was observed, indicating that the matrix was amorphous. Raman spectroscopy (Figure 3.6) of the NPs obtained with both lasers showed that the width and proximity of bands D and G matched the values reported in the literature for amorphous carbon [5]. However, Zhang et al. [4] attributed a similar spectrum for OLC structures. Further characterization is still required to confirm this statement, as the amorphous carbon signal could overlap with the signals of the OLC structures. The deconvolution of the peaks for both pulse durations is illustrated in Figure 3.6. The G band was located at 1580 and 1588 cm^{-1} for ultra-short and short pulses,

respectively. This band corresponds to the E_{2g} vibrational mode and indicates the stretching vibration of the sp²-type hybridized carbon bonds in the graphitic structure. Furthermore, this is the characteristic band for the degree of crystallinity. The D bands were located at 1355 and 1343 cm⁻¹ for ultra-short and short pulses, respectively. This band is directly assigned to the degree of structural disorder of the graphite due to the loss of symmetry or vibration of the carbon atoms' sp² and sp³ hybridized bonds. The intensity of the D band was higher than the G band ($I_D/I_G > 0.90$ for both cases), which indicates that the degree of disorder was very high, confirming the existence of amorphous carbon.
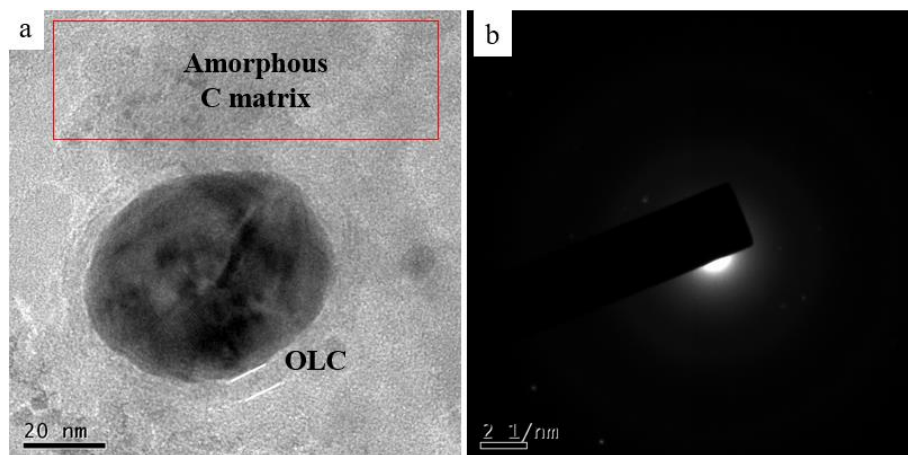
Figure 3.5 a) HRTEM image of MoC@C core-shell nanoparticle embedded in an amorphous carbon matrix when synthesized with short pulses. b) SAED pattern taken in the section inside the red rectangle in a) showing no diffraction signals.
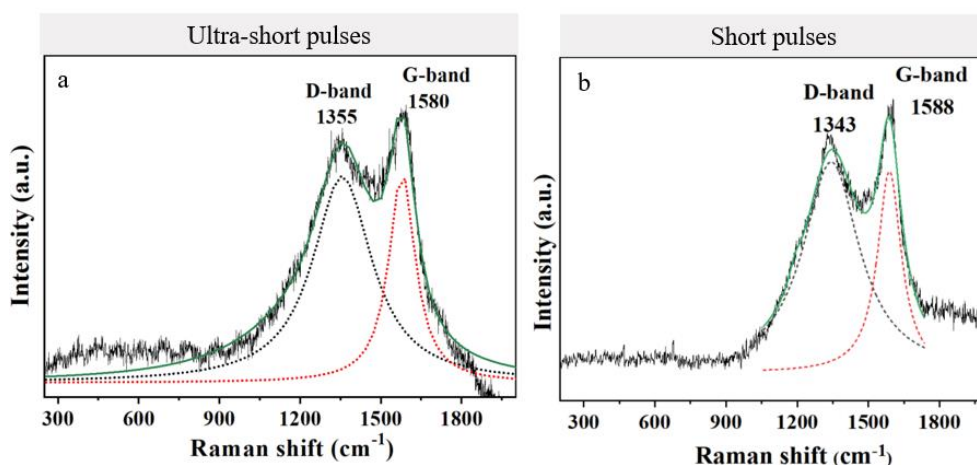
Figure 3.6 Raman spectroscopy of samples obtained with a) ultra-short pulses and b) short pulses. Dashed lines represent the deconvolution of D and G bands in two Lorentzian curves. The solid green line corresponds to their sums.

The NPs synthesized with both pulse durations were encapsulated with onion-like carbon structures (OLC) (Figure 3.7). These structures had a thickness between 3 to 5 nm and an interlaminar distance of ~ 0.35 nm. The theoretical length reported for the spaces between the layers of OLC structures corresponds to 0.335 nm [13]. In contrast with the reported OLC structures, these possessed irregular shapes adapted to the morphology of the NPs. Such changes in shape could have caused a residual strain in the graphitic microstructures, and longer distances between layers might have been necessary to balance its internal energy.

The HRTEM-indexed images in Figure 3.7 showed the presence of MoC for the samples synthesized with both lasers. The specific phase was the phase delta with an interplanar distance of 2.47Å and a (111) plane (JCPDS #03-065-8092). No oxides were observed in the HRTEM particles indexed. Additionally, the Raman spectroscopy did not report oxides signals, as these would have been observed within 100 cm^{-1} and 1000 cm^{-1}.
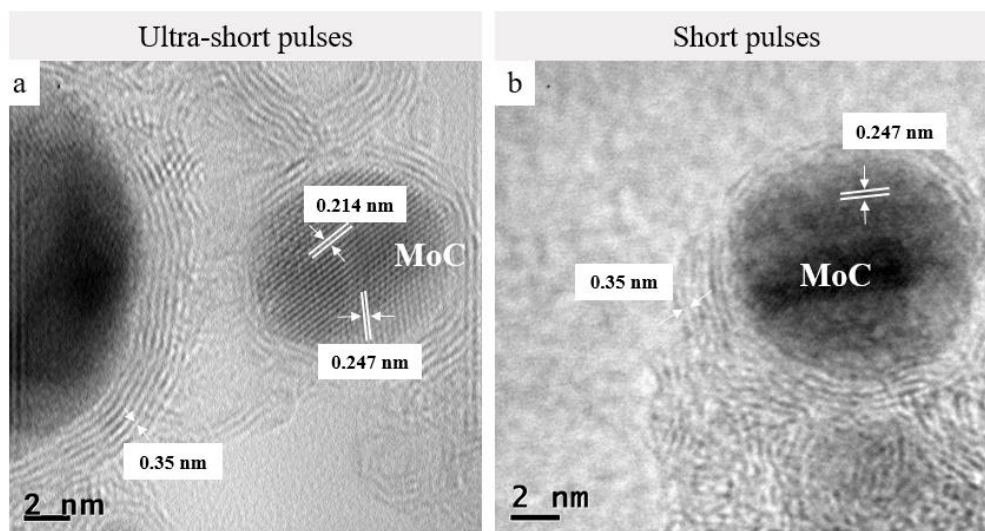
Figure 3.7 HRTEM images of MoC@C core-shell NPs synthesized with short and ultra-short pulse lasers.

3.4.3   Formation of MoC NPs encapsulated in carbon structures

A generalized explanation of the mechanism that led to the formation of MoC NPs is illustrated in Figure 3.8. The high temperature and pressure of the plasma plume (region I) induce the ionization and atomization of the toluene and the material ablated, thereby generating radicals, ions, clusters, and/or atoms [14]. The decomposition of toluene is not well understood due to complications in its measurements. Oehlschlaeger et al. [15] reported that one of the most important complications of toluene

decomposition is due to it taking place via two channels: $C_6H_5CH_3 \rightarrow C_6H_5CH_2 + H$ or $C_6H_5CH_3 \rightarrow C_6H_5 + CH_3$. Due to other secondary and recombination reactions, isolating the kinetics of the two reactions mentioned above is challenging.

Regardless of the exact decomposition mechanism of toluene, the excited species formed from the solvent decomposition will react with Mo atoms, ions, clusters, etc. As the plume experiences an adiabatic expansion, a cavitation bubble is formed, leading to nucleation and growth processes of the MoC NPs (region II) [16]. Mo has a high number of unfilled d-orbitals. Therefore, its affinity to carbon is high due to the possibility of entrapping carbon atoms in the metal vacancies, thus, evolving into metal carbides [17]. Not all of the carbon resultant from the decomposition of the solvent and the graphite ablation participates in the formation of MoC. Therefore, the excess carbon precipitates due to the rapid cooling and finally become the graphite coating (OLC) surrounding the nanoparticles (region III). Letzel et al. [18] reported that carbon encapsulation should occur at the end of the plasma phase and the initial stage of the bubble phase (interface reactions, region III).

When carbon saturation occurs, and the high temperature and pressure are no longer maintained, no more OLC can be formed. As a result, an amorphous carbon matrix is formed. Simultaneously, the NPs are ejected and transferred into the solvent. These NPs will be subsequently exposed to continuous irradiation causing variations in the OLC shells, and more amorphous carbon can condense on the surface of the particles (region IV). Additionally, phase transformations of the MoC might occur in this stage.

Another possible theory of the formation of OLC was studied by Zeiger et al. [19]. It was reported that amorphous carbon could evolve into OLC upon heating under temperatures > 1700 °C. Laser ablation can easily attain this temperature, as temperatures above 4700 °C have been reported [20].
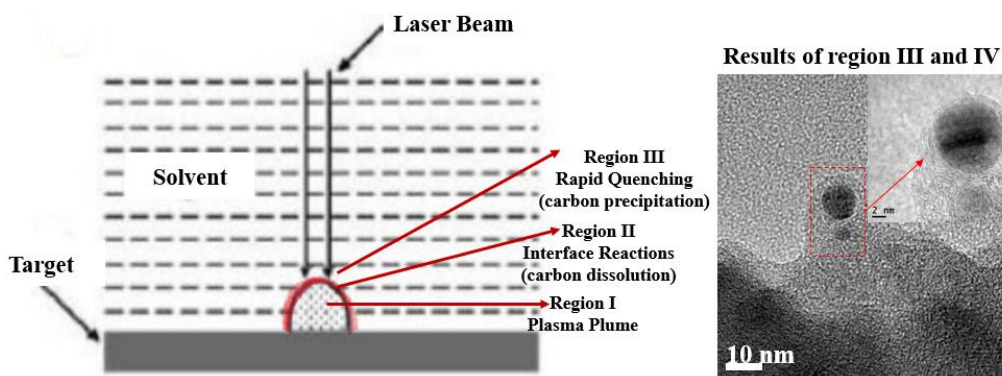
Figure 3.8 Illustration of the steps taking place during the formation of MoC-graphite core-shell nanoparticles.

3.5 Conclusions

In summary, laser ablation in toluene under a nitrogen atmosphere was a simple and fast method for synthesizing spherical MoC@carbon core-shell nanostructures. An additional ablation step of a graphite target was necessary to form OLC shells, as the carbon obtained only from the toluene decomposition was not enough to cause graphitization on the surface of the NPs. The NPs synthesized with ultrashort pulses showed a slightly narrower size distribution since 64% were located between 3 nm and 6 nm. With short pulses, a thicker matrix of amorphous carbon was obtained. This proposed to be due to higher thermal effects, shorter relaxation times, and higher beam absorption by the solvent and nanoparticles. The carbon matrix might be predominant with both pulse durations, as Raman spectroscopy only showed a signal of amorphous carbon, however, there is a possibility that signals from both structures are overlapping. No Mo oxides were observed when toluene was used, thus indicating that the carbonaceous coating prevents the oxidation of the metal.

3.6 References

1. Zhang, H., Liang, C., Liu, J., Tian, Z., & Shao, G. (2013). The formation of onion-like carbon carbon-encapsulated cobalt carbide core/shell nanoparticles by the laser ablation of metallic cobalt in acetone. Carbon, 55, 108-115. doi:10.1016/j.carbon.2012.12.015

2. Correard, F., Maximova, K., Estève, M.-A., Villard, C., Roy, M., Al-Kattan, A., et al. (2014). Gold nanoparticles prepared by laser ablation in aqueous biocompatible solutions: assessment of safety and biological identity for nanomedicine applications, International Journal Nanomedicine,9, 5415–5430.

3. Mafuné, F., Miyajima, K., & Ahmed Sobhan, M. (2013). Physical preparation of nanoalloys. En F. Calvo, Nanoalloys From Fundamentals to Emergent Applications (págs. 39-74). Waltham: Elsevier.

4. Zhang, H., Liang, C., Liu, J., Tian, Z., & Shao, G. (2013). The formation of onion-like carbon carbon-encapsulated cobalt carbide core/shell nanoparticles by the laser ablation of metallic cobalt in acetone, Carbon, 55, 108–115.

5. De Bonis, A., Santagata, A., Galasso, A., Laurita, A., & Teghil, R. (2017). Formation of Titanium Carbide (TiC) and TiC@C core-shell nanostructures by ultra-short laser ablation of titanium carbide and metallic titanium in liquid. Journal Colloid Interface Science, 489,76–84

6. Krüger, A. (2010). Carbon Onions and Related Materials. En A. Krüger, Carbon Materials and Nanotechnology (pág. 284). Weinheim: WILEY-VCH

7. Mohapatra, D., Badrayyana, S., & Parida, S. (2016). Facile wick-and-oil flame synthesis of high-quality hydrophilic onion-like carbon nanoparticles. Materials Chemistry and Physics, 112-119. doi:10.1016/j.matchemphys.2016.02.057

8. Quiroz, J., Frigini Mai, E., & Teixeira da Silva, V. (2016). Synthesis of Nanostructured Molybdenum Carbide as Catalyst for the Hydrogenation of Levulinic Acid to yValerolactone. Topics in Catalysis, 148-158. doi:10.1007/s11244-015-0433-6 32.

9. De Bonis, A., Curcio, M., Santagata, A., Galasso, A., & Teghil, R. (2020). Transition Metal Carbide Core/Shell Nanoparticles by Ultra-Short Laser Ablation in Liquid. Nanomaterials, 10(1), 145.

10. Amendola, V., & Meneghetti, M. (2009). Laser ablation synthesis in solution and size manipulation of noble metal nanoparticles. Phys. Chem. Chem. Phys, 11, 3805–3821. doi:10.1039/b900654k

11. Tomko, J., O'Malley, S., Trout, C., Naddeo, J., Jimenez, R., Griepenburg, J., et al. (2017). Cavitation bubble dynamics and nanoparticle size distributions in laser ablation in liquids. Colloids and Surfaces A: Physicochemical and Engineering Aspects, 368–372. doi:10.1016/j.colsurfa.2017.03.030

12. Kovalchuk-Kogan, T., Bulatov, V., & Schechter, I. (2015). Optical Breakdown in Liquid Suspensions and Its Analytical Applications. Advances in Chemistry, 1-21. doi:10.1155/2015/463874

13. Inoue, A., Seto, T., & Otani, Y. (2012). Onion-like carbon nanoparticles generated by multiple laser irradiations on laser-ablated particles. Carbon, 50, 1116-1122. doi:j.carbon.2011.10.024

14. Kalus, M. R., Barsch, N., Streubel, R., Gokce, E., Barcikowski, S., & Gokce, B. (2017). How persistent microbubbles shield nanoparticle productivity in laser synthesis of colloids-quantification of their volume, dwell dynamics, and gas composition. Phys. Chem. Chem. Phys. 2017, 19, 7112−7123.

15. Oehlschlaeger, M.A., Davidson, D.F., & Hanson, R.K. (2007). Thermal decomposition of toluene: overall rate and branching ratio. Proceedings of the Combustion Institute, 31, 211–219.

16. Lam, J., Amans, D., Chaput, F., Diouf, M., Ledoux, G., Mary, N., et al. (2014). γ-Al2O3 nanoparticles synthesized by pulsed laser ablation in liquids: a plasma analysis. Physical Chemistry Chemical Physics, 16, 963−973.

17. Zhang D., Zhang C., Liu J., Chen Q., Zhu X., Liang C. (2019). Carbon encapsulated metal/metal carbide/metal oxide core-shell nanostructures generated by laser ablation of metals in organic solvents. ACS Applied Nano Materials, 2, 8–39. doi: 10.1021/acsanm.8b01541.

18. Letzel, A., Gökce, B., Wagener, P., Ibrahimkutty, S., Menzel, A., Plech, A., & Barcikowski, S. (2019). Size quenching during laser synthesis of ACS Applied Nano Materials, 2, 28−39 38.

19. Zeiger, M., Jackel, N., Mochalin, V. N., & Presser, V. (2016). Review: carbon onions for electrochemical energy storage. Journal of Materials Chemistry A, 4, 3172−3196

20. Saito, K., Takatani, K., Sakka, T., & Ogata, Y. H. (2002). Observation of the light emitting region produced by pulsed laser irradiation to a solid−liquid interface. Applied Surface Science, 197, 56−6

CHAPTER 4

EFFECT OF PROCESSING, CHEMICAL COMPOSITION, AND ANNEALING

TEMPERATURE ON THE MECHANOCHEMICAL SYNTHESIS OF

Mo$_X$C-GRAPHITE COMPOSITE

4.1   Abstract

Mechanochemical ball milling was used to synthesize a Mo$_2$C-Gr composite without reductants or particle control agents. Subsequent annealing at low temperatures for only one hour was implemented to improve the homogeneity of the phase fraction of the carbide and the crystallinity of the graphite reinforcement. We demonstrated that ball milling is an easy and effective method to synthesize molybdenum carbide with great control to obtain a stable Mo$_2$C phase. To evaluate the evolution of the powders with different graphite molar content and annealing temperatures, X-Ray diffraction, Raman spectroscopy, and scanning electron microscopy were employed.

4.2   Introduction

Transition metal carbides have recently received considerable attention as advanced materials for their attractive physical and chemical properties, including mechanical hardness, thermal stability, superconductivity, and catalytic performance. The typical organic chemical reactions in which metal carbides are used are hydrogenation, hydrodesulfurization, hydrodenitrogenation in petroleum refining, and hydrogen evolution reaction [1-6].

Molybdenum carbide is one of the most promising refractory carbides for thermal stability at high temperatures. Two of the most studied systems are α-Mo$_2$C and β-Mo$_2$C phases [7], while the metastable phases such as δ-MoC, γ-MoC, γ'-MoC, and η-MoC are less reported. On the other hand, Graphite-Metal Carbides composites have been studied since the 1960s [8-10] because, when combined, they minimized undesirable properties of carbides and graphite, e.g., poor thermal shock resistance and reactivity with oxygen, respectively [11]. Thanks to these properties, the family of graphite-matrix composites (MoGr) reinforced with molybdenum carbide has been developed to meet multiple requirements in terms of electrical conductivity, energy absorption, mechanical strength at high strain rates, and thermal stability for nuclear and aerospace applications [12-14].

Most reported studies on the synthesis of graphite systems reinforced with molybdenum carbide involved processing by liquid phase sintering with temperatures exceeding 2500 °C [10,15]. These processes require the complete melting of the metal carbide phase leading to drawbacks such as

heterogeneities in the volume fraction of the metal carbide due to the volatility of residual compounds [16] and prolonged process duration.

Molybdenum carbide reinforced with carbon structures is another system currently under investigation. So far, very little about this system, including its metastable phases is known due to the challenge in its fabrication since high temperatures are required to increase the diffusion between the carbon and molybdenum. A few potential processing methods to synthesize carbides have recently emerged, one of them is high-energy ball milling [17-20], which sometimes is followed by a heat treatment at low temperatures. Xia et al. [17] reported a method for synthesizing molybdenum carbide by mechanical alloying a MoO_3+Al+C mixture in an inert atmosphere. The authors reported that in the first nine hours of milling, no reactions proceeded in the mechanically activated mixture. A further increase in milling time resulted in the formation of β-Mo_2C and η-Mo_3C_2 phases in the sample that also are dependent on the graphite content.

Molybdenum carbide nano-crystalline structures have also been produced by mechano-chemical synthesis at room temperature. Stable powders of Mo_2C with a polyaromatic nanocarbon reinforcement were obtained from mechanically activated mixtures of molybdenum carbide, molybdenum oxide, and carbon or metal reductants [19-21]. With mechanical alloying, the synthesis of molybdenum carbides is facilitated due to the plastic deformation during the process, which refines the particle and increases the grain boundary area, thus reducing the diffusion distances between C and Mo. The diffusion is further aided due to the increase in the defect density and a local rise in temperature during deformation. Moreover, further annealing may bring the system to equilibrium. The combination of these effects is proposed to enable sufficient diffusion to occur in the interfacial regions of the nanocrystalline grains to form molybdenum carbide, and could also facilitate the dispersion of graphite as a second phase to effectively strengthen the carbide matrix thereby creating an intimate bond at the interface between the two phases.

This method mentioned above is worth further study to produce heterostructures, i.e., MoC/C and Mo_2C/C for applications such as electrocatalysis, electronics (energy storage devices), etc. [22-26]. Therefore, this project aims to evaluate the synthesis of Mo_2C/C composite by using elemental molybdenum and different molar graphite concentrations MoC_x (x= 1, 1.5, 2) without reductants or particle control agents. Subsequent calcination in an argon atmosphere at 800 °C and 1000 °C was performed for the excess of graphite, which acts as a solid phase carbidizer to form molybdenum carbide. The structure and morphology of the molybdenum carbide and the graphite reinforcement were also assessed.

4.3   Experimental

Molybdenum and graphite powders with a purity of 99.99% and a particle size range of 1-2 μm and <45 μm, respectively, were used in the mechanosynthesis of Mo_2C-graphite composite. Four groups of samples with different molar graphite contents were established (see Table 4.1). Mechanical activation was carried out in a SPEX (SamplePrep 8000D) at different times without interruption, with a rotation speed of 1060 rpm and a ball-to-powder mass ratio of 7:1. After milling, the samples were annealed inside a tube furnace for 1 hour with a heating rate of 12 °C/min. The heat treatment was carried out under an argon atmosphere at 800 °C for the first and second samples and at 1000 °C for the third and fourth samples. The morphologic features were characterized using an NNS450 scanning electron microscope (SEM). The structural composition was determined using X-ray diffraction (XRD) from PANalytical Empyrean Series 2 with CuKa radiation (λ= 0.15406 nm). To analyze the graphite structures, micro-Raman spectroscopy (LabRaman HR-800 of Jobin-Yvon-Horiba) with a 532 nm He-Ne laser as the excitation source and SEM analysis were utilized.

Table 4.1 Graphite molar contents and experimental parameters. LC refers to low carbon, and HC refers to high carbon.

Process condition	Sample reference name	Milling time	Annealing	Annealing time	Molar concentration
1	1-LC	8 hours	800 °C	1 hour	MoC_x (x=1)
1	1-HC	8 hours	800 °C	1 hour	MoC_x (x=2)
2	2-LC	15 hours	1000 °C	1 hour	MoC_x (x=1.5)
2	2-HC	15 hours	1000 °C	1 hour	MoC_x (x=2)

4.4   Results and discussion

4.4.1   Synthesis of MoCx (x= 1, 1.5, 2) by mechanical alloying.

Ball milling and annealing experiments were conducted in an Ar atmosphere to avoid oxidation. Different mechanical activation times were used for all the samples to relate the proportion of carbon and the milling time needed to obtain the molybdenum carbide-graphite composite. A time of eight hours was established as a baseline for samples 1-LC and 1-HC, and the milling time for samples 2-LC and 2-HC was modified based on the results of the first experiments. The formation behavior of molybdenum carbide phases and graphite crystallization was also considered. The formation of MoC-Graphite composite was expected to be formed after the mechanical activation, however a non-homogeneity of

molybdenum carbides and graphite defects was obtained. Therefore, annealing was carried out to eliminate these defects.

The XRD diffractogram for sample 1-LC before the annealing (Figure 4.1a) shows MoC as the predominant phase fraction. All Bragg peaks observed before the annealing belong to reflections of an FCC structure, except for the peak at 40.53°. The width of this peak precludes the evaluation of its crystalline structure, although there is a possibility of the presence of the α-Mo$_2$C phase. The set of broad diffraction peaks could be attributed to the residual stresses induced during the milling operation. For sample 1-HC, the milling time was insufficient to generate a complete reaction to produce molybdenum carbide, but instead, an inhomogeneous mixture of MoC/Mo was obtained (Figure 4.1b). Increasing the molar concentration of graphite demands an increase in the milling time as the diffusion of C into MoC is a slow and energetically demanding process. However, after thermal treatment of this sample, the Mo peaks disappeared, and sets of orthorhombic structures of α-Mo$_2$C were obtained (Figure 4.1d). In contrast, the powders of the 1-LC sample were not as stable as a mixture of compounds, e.g., MoC(Mo$_3$C$_2$)$_{1.33}$, MoOC, and α-Mo$_2$C were obtained after the annealing (Figure 4.1c). The latter indicates that the polyaromatic carbon layers do not evenly coat the surface of carbide crystallites.
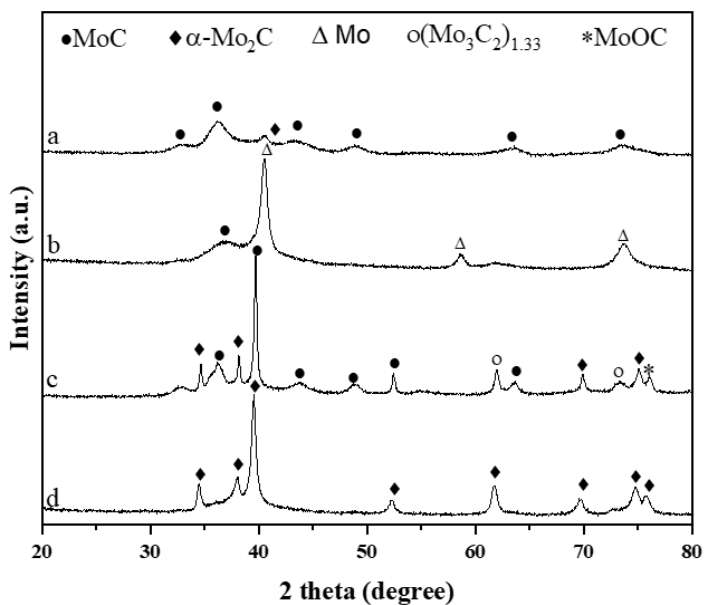
Figure 4.1 XRD comparison of the powders milled for 8 hours before and after annealing at 800 °C with various carbon contents. a) Sample 1-LC (MoC$_x$ x=1) after milling; b) Sample 1-HC (MoC$_x$ x=2) after milling; c) Sample 1-LC after annealing and d) Sample 2-HC after annealing.

Although molybdenum carbide was not a predominant product after the mechanical alloying in the sample with higher graphite content, further annealing proved efficient to sharpen the pattern and confirmed the presence of crystalline Mo_2C. The mechanic-activated powder can easily reach the transformation into α-Mo_2C at 800 °C in 1 hour, which is a low temperature for the synthesis of carbides compared to conventional techniques, i.e., liquid phase sintering [15]. It is assumed that the composite obtained after milling is MoC/Mo with excessive polyaromatic carbon. This carbon is the product of the lack of solubility between carbon and molybdenum carbide, which leads to the precipitation of carbon structures and might contribute to the high cohesion of the matrix and C reinforcement. This carbon coats the molybdenum and later facilitates carbide production during the annealing. This can be verified because no molybdenum oxide was observed in the XRD and Raman results.

For sample 1-LC, a slight increase in graphite crystallinity can be observed (Figure 4.2 a-c). In contrast, for 1-HC, both Raman results before and after annealing (Figure 4.2b-d) are similar, even though the α-Mo_2C phase demonstrated a higher crystallinity than the products obtained for the sample with less graphite content. As seen in Figure 4.2 c, the G-band is at 1584 cm^{-1}, corresponding to the vibrational mode E_{2g}, which is assigned to the stretching vibration of the sp^2 carbon-hybridized bonds in the graphite structure. Band D is located at 1352 cm^{-1} and is directly assigned to the degree of structural disorder of graphite caused by loss of symmetry or vibration of stretching in the sp$_2$ and sp$_3$ hybridized bonds of carbon atoms [27]. In this case, the D band is considerably less intense than the G band, which proves that the stress is relieved after the annealing. The band 2D at 2692 cm^{-1} corresponds to the overtone of the D band, which is related to the stacking order of graphite sheets along the hexagonal axis. With increasing graphene layers, the 2D band will become wider, and the shape of the 2D band tends to be that of 3-D graphite. The study of this band can bear information about the relative orientations and interactions of the graphite layers [28,29]. Because not all the graphite was able to react with Mo to form molybdenum carbide in the sample with the highest graphite content (1-HC) after the milling, most of the energy during the annealing was used to form carbides instead to improve the crystallization of the graphite reinforcement. Hence, the remaining energy and time were insufficient to improve the graphite's crystallinity. This assumption is reflected in the similarity of the G and D bands before and after the annealing. Due to the lack of homogeneity in composition after the milling and residual strains after the annealing of samples 1 (MoC_x x=1) and 2 (MoC_x x=2), the milling time and the annealing temperature were increased to prevent these defects.
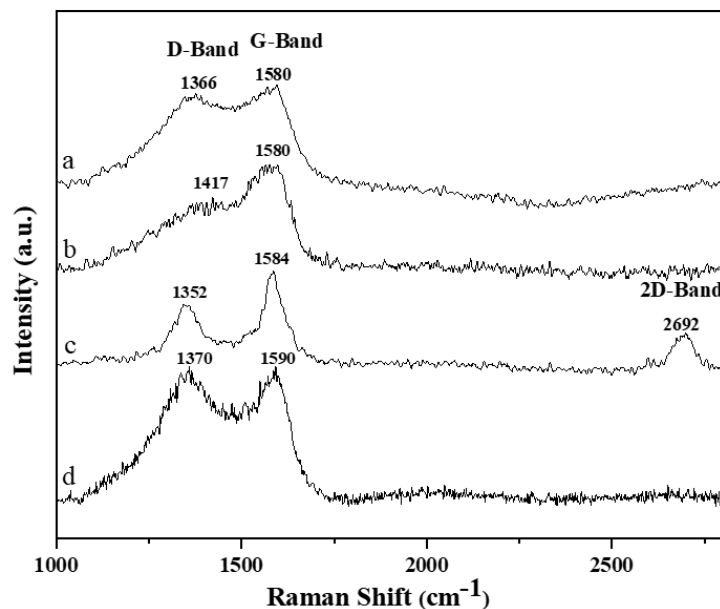
Figure 4.2 Raman comparison of the powders milled for 8 hours before and after annealing at 800 °C with different carbon contents. a) Sample 1-LC (MoC_x x=1) and b) Sample 1-HC (MoC_x x=2) after milling; c) Sample 1-LC and d) Sample 2-HC after annealing.

The as-milled powders of sample 2-LC and sample 2-HC showed the same behavior as sample 1-LC. After the annealing at 1000 °C for 1 hour, the homogeneity in the phase crystallinity increased considerably.

Figure 4.3a-b show peaks corresponding to the hexagonal Mo_2C structure (ICDD #00-035-0787). The reflections are narrower, and their intensity grew more than that of the reflections of previous samples. Reflections of graphite were also not observed in this new procedure, similar to previous reports [17,19-21]. The transformation to Mo_2C was easier to obtain in samples 2-LC and 2-HC after the annealing because the milling time increment caused a complete reaction with the molybdenum and graphite. This claim can be supported by the fact that the graphite also incurred changes in its phases during annealing, and as depicted in Figure 4.4. the crystallinity rose considerably. It has been reported that the excess of graphite encapsulated in the carbide with an onion-like carbon structure [19, 21] provides the composite with more stability against oxidation and corrosion.
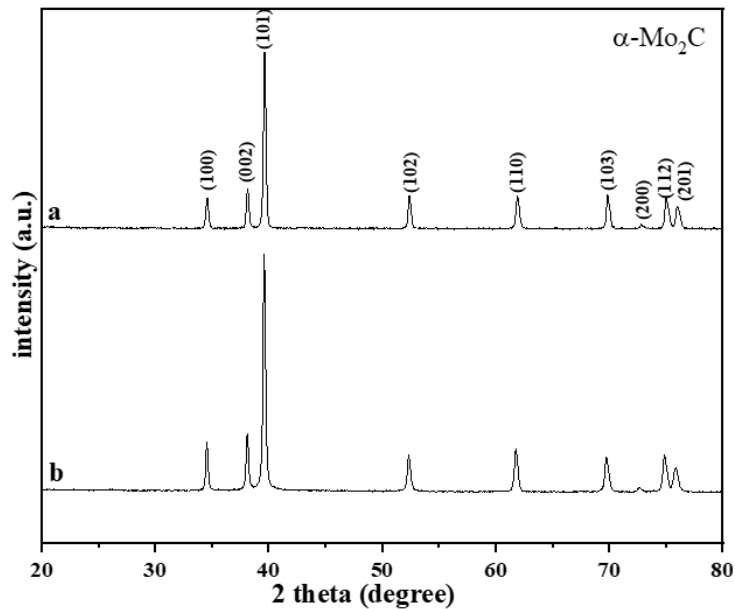
Figure 4.3 XRD comparison of the as-milled powders after annealing at 1000 °C. a) Sample 2-LC (MoC_x x=1.5) and b) Sample 2-HC (MoC_x x=2) milled for 15 hours and annealed.
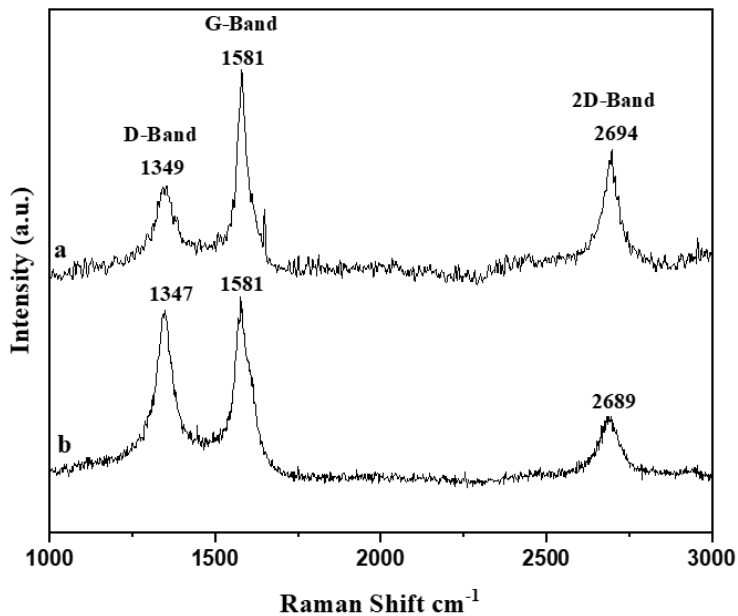
Figure 4.4 Raman comparison of the powders milled for 15 hours after annealing at 1000 °C. a) Sample 2-LC (MoC_x x=1.5) and b) Sample 2-HC (MoC_x x=2) after annealing.

Raman spectrograms (Figure 4.4) demonstrated the presence of graphite, forming a composite of α-Mo_2C-graphite. In both samples, graphitic structures better defined than the ones obtained at lower

milling times were observed. The graphite structures of sample 2-LC (MoC_x x=1.5) showed the highest crystallinity making this composition the most successful in this study.

Morphological and size characteristics of the milled samples before and after annealing greatly depend on graphite molar concentration. By increasing the milling time, more agglomeration of powders can be expected. However, sample 1-LC, with the lowest molar concentration of graphite and milled for 8 hours, showed more agglomerated particles (Figure 4.5a). After the annealing (Figure 4.5b), the particle size distribution improved, thus decreasing its agglomeration. In contrast, sample 2-LC (MoC_x x=1.5) showed less agglomeration and some bigger particles (Figure 4.5c). After its annealing (Figure 4.5d), the morphology of the particles radically changed into very compact powders, whereby it is understood that graphite effectively created an intimate bond at the interface with the carbide. Figure 4.5 d shows that the small particles stack upon one another, making the powder much more compact. This could be an advantage to obtaining highly dense composites on further processes such as hot pressing or spark plasma sintering (SPS).
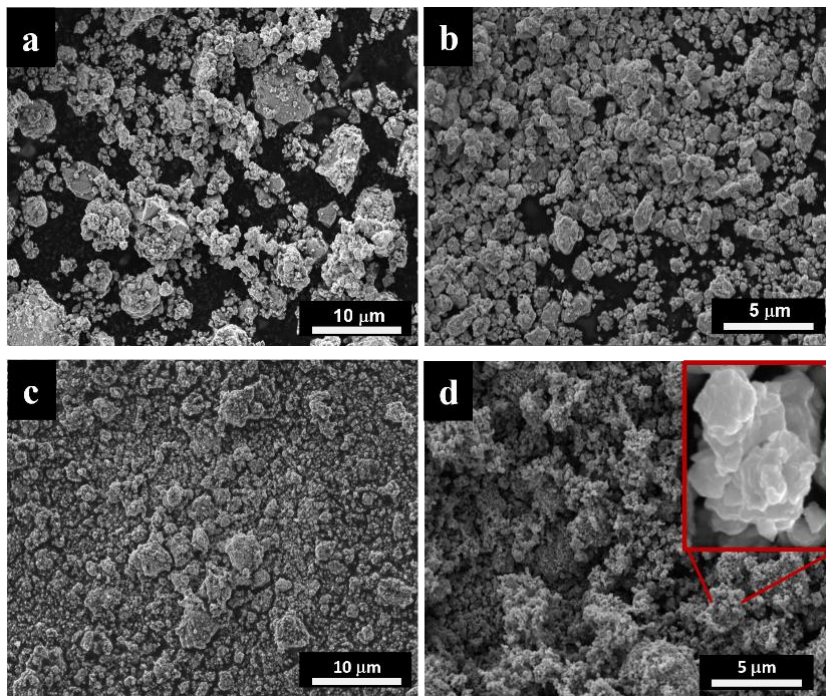
Figure 4.5 SEM images of a) Sample 1-LC (MoC_x x=1) before annealing and b) after annealing at 800 °C; c) Sample 2-LC (MoC_x x=1.5) before annealing and d) after annealing at 1000 °C.

4.5   Conclusions

Low-temperature annealing of mechanically activated mixtures of molybdenum with graphite have been successfully developed to obtain a Mo_2C-Gr composite. The most significant contribution made in this work was the study of different molar concentrations of graphite aiming to find the optimal concentration (MoC_x x=1.5) to synthesize a homogeneous and stable Mo_2C and to improve the crystallization of the graphite reinforcement at 1000 °C. The results show that the annealing is crucial in formation of the carbide and graphitic structures. Finally, thanks to the simplicity of this process, this proposed method can be widely used for large-scale preparation as no reductants, particle control agents or high synthesis temperatures are needed.

4.6   References

1. Wang, H., Wang X. H, Zhang, H., Du, X., Li, W., & Tao, K. (2007). Synthesis of Bulk and Supported Molybdenum Carbide by a Single-Step Thermal Carburization Method. Chemistry of Materials, 1801-1807.

2. Du, J., Wu, J., Guo, T., Zhao, R., & Li, J. (2014). Catalytic performance of Mo2C supported on onion-like carbon for dehydrogenation of cyclohexane. RSC advances, 4, 53950–53953.

3. Hugosson, H., Eriksson, O., & Lars, N. (1999). Theory of phase stabilities and bonding mechanisms in stoichiometric and substoichiometric molybdenum carbide. J. Appl. Phys., 86(7), 3758-3767.

4. Souza Macedo, L., Oliveira, R., van Haasterecht, T., Teixeira de Silva, V., & Bitter, H. (2019). Influence of synthesis method on molybdenum carbide crystal structure and catalytic performance in stearic acid hydrodeoxygenation. Appl. Catal, 241, 81-88.

5. Ramaiyan, K., Ozden, S., Maurya, S., Kelly, D., Babu, S., Angelica, B., et al. (2019). Molybdenum Carbide Electrocatalysts for Electrochemical. J. Electrochem. Soc., 167, 044506.

6. Deng, Y., Ge, Y., Xu, M., Yu, Q., Xiao, D., Yao, S., & Ma, D. (2019). Molybdenum Carbide: Controlling the Geometric and Electronic Structure of Noble Metals for the Activation of O–H and C–H Bonds. Acc. Chem. Res., 52, 3372–3383.

7. Pierson, H. (1996). Handbook of Refractory Carbides & Nitrides: Properties, Characteristics, Processing, and Applications. New Jersey: Noyes Publications.

8. White, J., & Pontelandolfo, J. (1966). Graphite-Carbide Materials Prepared by Hot-Working with the Carbide Phase in the Liquid State. Nature, 209, 1018-1019.

9. White, J., & Pontelandolfo, J. (1966). Graphite-Carbide Materials Prepared by Hot-Working with a Dispersed Liquid-Carbide Phase. Carbon, 4, 305-314.

10. Harada, Y. (1966). Feasibility of fabricating graphite-metal carbide composites of high density and strength by hot pressing. Website: NASA Technical Reports Server: https://ntrs.nasa.gov/search.jsp?R=19660019930

11. John, D., & Jenkins, G. (1986). Hot-working and strengthening in metal carbide-graphite composites. J. Mater. Sci., 21, 2941 2958.

12. Morgan, W. C. (1981). International Nuclear Information System (INIS). Website: https://inis.iaea.org/collection/NCLCollectionStore/_Public/12/633/12633176.pdf?r=1&r=1

13. A. Bertarelli et al., "Innovative MoC – graphite composite for thermal management and thermal shock applications," 2015 31st Thermal Measurement, Modeling & Management Symposium (SEMI-THERM), San Jose, CA, 2015, pp. 56-59.

14. Simos, N., Zhong, Z., Ghose, S., Kirk, H., Trung, L.-P., McDonald, K., . . . Mokhov, N. (2016). Radiation damage and thermal shock response of carbon-fiber-reinforced materials to intense high-energy proton beams. PHYS. REV. ACCEL. BEAMS, 19, 111002.

15. Guardia-Valenzuela, J., Bertarelli, A., Carra, F., Mariani, N., Bizarro, S., & Arenal, R. (2018). Development and properties of high thermal conductivity molybdenum carbide - graphite composites. C, 135, 72-84.

16. Simos, N., Charitonidis, N., Simon, P., Whitaker, M., Zhong, H., Ghose, S., . . . Sprouster, D. (2021). Proton irradiation effects in Molybdenum-Carbide-Graphite composites. J. Nucl. Mater, 553, 153049.

17. Xia, Z., Shen, Y., Shen, J., & Li, Z. (2008). Mechanosynthesis of molybdenum carbides by ball milling at room temperature. J. Alloys. Compd., 453, 185-190.

18. An, G. & Liu, G. (2011). Preparation of ultramicro molybdenum carbide powders and study on wear properties of their coating. Rare Metals., 30, 262

19. Baklanova, O., Vasilevich, A., Lavrenov, A., Drozdov, V., Muromtsev, I., & Trenikhin, M. (2019). Synthesis of molybdenum carbide composite by mechanical alloying in air. Journal of Alloys and Compounds, 793, 715-722.

20. Cheng, P., Ouyang, L., Lang, C., Zhong, H., Liu, J., Wang, H., et al. (2023). All-pH Hydrogen Evolution by Heterophase Molybdenum Carbides Prepared via Mechanochemical Synthesis. ACS Sustainable Chem. Eng.

21. Bokhonov, B., Borisova, Y., & Korchagin, M. (2004). Formation of encapsulated molybdenum carbide particles by annealing mechanically activated mixtures of amorphous carbon with molybdenum. C, 42, 2067-2071.

22. Deng, M., Qi, J., Li, X., Xiao, Y., Yang, L., Yu, X., . . . Gao, Q. (2018). MoC/C nanowires as high-rate and long cyclic life anode for lithium ion batteries. Electrochim. Acta, 277, 205-210.

23. Zhang, H., Jin, H., Yang, Y., Sun, F., Liu, Y., Du, X., . . . Jiang, Z. (2019). Understanding the synergetic interaction within α-MoC/β-Mo2C heterostructured electrocatalyst. J. Energy. Chem, 35, 66-70.

24. Liu, X., Li, Z., Zhang, S., Long, H., Wei, H., Zhang, H., . . . Zhao, C. (2017). Mo2C@onion-like carbon/amorphous carbon nanocomposites as outstanding anode materials for ideal lithium-ion batteries. Ceram. Int., 43, 14446-14452.

25. Xiao, Y., Hwang, J.-Y., & Sun, Y.-K. (2016). Transition metal carbide-based materials: synthesis and applications in electrochemical energy storage. J. Mater. Chem. A., 4, 10379–10393.

26. Zhang, S., Wang, C., Qiu, H., Bao, Y., Long, T., Cai, W., & Huang, Y. (2020). Highly graphitic carbon shell on molybdenum carbide nanosheets by iron doping for stable hydrogen evolution. Int. J. Hydrog. Energy, 45, 14368-14374.

27. Tommasini, M., Castiglioni, C., Zerbi, G., Barbon, A., & Brustolon, M. (2011). A joint Raman and EPR spectroscopic study on ball-milled nanographites. Chem. Phys. Lett., 516, 220-224.

28. Ferrari, A., & Basko, D. (2013). Raman spectroscopy as a versatile tool for studying the properties of graphene. Nature, 8, 235-246.

29. Pimenta, M., Dresselhaus, G., Dresselhaus, M., Cancado, L., Jorio, A., & Saito, R. (2007). Studying disorder in graphite-based systems by Raman spectroscopy. Phys. Chem. Chem. Phys, 9, 1276 –1291.

CHAPTER 5
CoCr ALLOY PROCESSED BY SELECTIVE LASER MELTING: COMPARISON OF ATOMIZED AND MILLED POWDER FEEDSTOCKS

5.1   Abstract

Due to its distinct non-equilibrium solidification and heating process, selective laser melting (SLM) demonstrates great potential for fabricating innovative materials. The vast majority of SLM-fabricated alloys in use today are limited to microstructures with long columnar grains. As a result, challenges such as anisotropy, low fatigue life, and crack propagation have been frequently reported. A solution to this problem is to produce fine-equiaxed grains throughout the component to improve its mechanical performance. Currently, there are limited strategies to achieve this change in microstructure because the high thermal gradients and rapid cooling rates inherent to SLM are difficult to control. In this work, the approach implemented to achieve grain refinement and equiaxed grains is the addition of SiC and WC nanoparticles to the CoCr powder feedstock. Consequently, the powders were melted by different laser techniques. The data was compared with commercial atomized CoCr powder, which underwent the same laser melting conditions. A significant reduction in grain size was observed through the addition of these nanoparticles. The size distribution, however, was not uniform along the build direction. The limitations of this approach are discussed in detail for each laser process applied.

5.2   Introduction

In recent years, research efforts to address compositional modification to improve the printability of alloys for the additive manufacturing industry (AM) have emerged. The limitations to developing more additively manufactured alloys are in part attributed to the incompatible solidification dynamics during the printing process. Alloys in AM tend to form coarse-textured columnar structures as a result of epitaxial grain growth due to the high thermal gradients and high cooling rates within the small melt pools [1,2]. The propensity for coarse columnar grain structures is undesirable as it causes significant anisotropy in the mechanical properties, solute segregation, and susceptibility to periodic crack formation [3].

Preventing columnar grains from forming has been approached by optimizing the process parameters and the alloy composition to form more equiaxed grains. Also, when decreasing the thermal gradients and cooling rates with laser parameters, equiaxed grains can be formed [3]. However, they become vulnerable to remelting and resolidifying epitaxially from the existing grains due to the low nucleation barrier [1]. Hence the best solution is to promote the formation of fine equiaxed grains by adding nucleant particles to

control the solidification conditions [4]. Heterogeneous nucleation is required for successful grain refinement in AM. This can be promoted based on the potency or the number density of nucleant particles, thereby counteracting the almost negligible constitutional supercooling (CS) zone formation during AM [4,5].

For AM, the activated nucleants preferably should be much smaller compared to those used for conventional methods (e.g., metal casting) for more uniform distribution in the metal matrix. Other factors to consider are the atomic mismatch across the interface between the nucleant and the matrix metal and thermodynamic stability in the desired alloy. When the mismatch is small, a low critical undercooling is needed for heterogeneous nucleation. When adding particles with these characteristics, microstructural control can be synergistically engineered to tailor mechanical properties to suit specific applications. Martin et al. [6] used Al_3Zr secondary particulates to successfully induce grain refinement in a 7075 series aluminum alloys for laser powder bed fusion (PBF-LB). The samples printed with the modified alloy showed an 80% increase in strength over AlSi10Mg alloy without adding nucleant particles. Ti-based and 316L stainless steel alloys have also been modified for AM processes. Additions of Cu [7] and La_2O_3 [8] in Ti alloys have been added to form fine equiaxed grains to control the formation of β grains and ultrafine eutectoid lamellar structures. Li et al. [9] reported that nano-sized VC_x particulate reinforcements in 316L alloy contributed substantially to the strengthening without detrimental defects for a selective laser melting process (SLM).

Powder feedstocks are usually decorated with lattice-matched nanoparticles. However, incorporating secondary phases in the powder surface or matrix can be extremely difficult. Incorporating particles at the instant of melting during gas atomization is one of the most successful techniques, although expensive and limited to producing only large powder batches. Other methods reported are electrodeposition, colloidal deposition, and ball milling [10,11]. Among these techniques, ball milling is an efficient technique to add uniformly non-miscible components due to the high plastic deformation of powder, thus inducing mechanochemical reactions.

The use of milled powder feedstock for AM processes is under debate due to its irregular morphology, size, surface roughness, and impurities. Metallic powder suitable for SLM are reported to have a spherical morphology and a small particle size (1–100 μm) with a narrow particle size distribution range. When these properties are not satisfied, adverse effects on the flowability and spreadability of the powder can be obtained. However, by modifying the milling parameters and concentration of the powder mixtures, it is possible to meet these basic requirements to achieve good quality in the printed parts. Successful examples of as-milled powder decorated with secondary phases for AM have been reported for Ti, Al, and stainless-steel alloys. Han et al. [12] synthesized Al-4 vol.% Al_2O_3 nano-composite powders

using high-energy ball milling with two different types of milling and pause combinations. Powders with nearly spherical morphology and similar flowability to atomized powder were obtained. Gu et al. [13] showed that planetary mixing of atomized AlSi$_{10}$Mg powder with TiC nanopowder could be >98% densified with optimized laser energy density. The milling and higher laser energy density processing resulted in dispersed nano TiC reinforcement and superior wear resistance. Zhai et al. [14] applied low-energy ball milling to prepare 316 L stainless steel powder by adding 1-3 wt.% micron-sized TiC particles. The 316L-TiC composites obtained were close to full density (≥99.5%), with a significant increase in strength due to grain refinement.

Currently, there are no investigations for powder production of CoCr alloys via ball milling. Regardless of the significant microstructural anisotropy reported [15], additional secondary phases have also not been evaluated to mitigate the formation of columnar grains. The yield strength, tensile strength, and elongation of the as-built Co–Cr–Mo fabricated samples are substantially affected due to their microstructure and mechanical anisotropy [16]. Therefore, in this work, we evaluated the impact of adding NPs on grain refinement as an alternative to mitigate anisotropy. Following the approach by Wang et al. [17], it was decided to add SiC and WC NPs due to the good bonding interface and the strengthening effect of the matrix. Commercially atomized CoCr alloy versus elemental Co- and Cr-milled powders reinforced with carbides will be compared before and after the SLM process. Additionally, this investigation will provide helpful guidance for developing small-scale AM because low powder quantities represent a challenge for SLM processes.

5.3   Methodology

5.3.1   Powder preparation

Two different powder feedstocks were used to compare the powder properties in laser melting additive processes. Commercial gas atomized powder from Allegheny Technologies (ATI) was used as a baseline, as this powder is currently used for manufacturing production. The second powder feedstock corresponds to milled elemental Co and Cr powders. High-energy ball milling (SPEX), planetary milling, and cryogenic milling techniques were used to generate the powders. Currently, no data is available for producing CoCr-based alloys via milling for AM processes; therefore, many parameters, including milling time, ball-weight ratio, jar material, and particle control agent, were investigated.

Atomized powder presented a particle size range from 2-45 μm. For comparison purposes between the two different powder feedstocks, the milled powder was limited to a maximum size of 45 μm through sieving. Powder chemical composition was significantly different, as shown in Table 5.1 on page 71. The milled powder consisted of alloying elemental powders Co and Cr with weight percentages of 77.4 % and

22.6 %, respectively, and 99.9% purity. SiC and WC nanoparticle additions were also incorporated to work as grain refiners. Around 10 grams of powder was produced via milling, and production yield varied based on each technique. Milling steps were repeated consecutively until 100 grams were obtained for the melting process. The process conditions for each method are shown in Table 5.2 on page 71.

5.3.2 Characterization techniques

Morphological and chemical characterization was carried out employing scanning electron microscopy (SEM/EDS from TESCAN, model Vega3 SBH). A Panalytical Empyrean X-ray diffractometer generated data for powder and solid parts with the following settings: an angular range of 30–110° using a step size of 0.02°, with a Cu Kα radiation source under 40 kV voltage and 40 mA current. The phase and microstructural analyses of the samples were determined by SEM, electron backscatter diffraction system (EBSD, Oxford), and scanning/transmission Electron Microscope (FEI Titan Themis 300).

5.3.3 Laser processing

5.3.3.1 Femtosecond pulsed laser

The first melting experiments were performed using a femtosecond laser (Satsuma, Amplitude Systems Laser) with a wavelength of 1040 nm, power up to 50 W, repetition rate up to 2 MHz, and pulse duration of 350 fs. A copper cup with dimensions of 250 μm in depth and 5 μm in diameter was used to hold the powder and simulated a powder bed. The powder surface was positioned near a beam waist of ~48 μm radius. Several parameters were tested to identify a window process with regions optimal for melting this alloy. The parameters modified are the following. The frequency range tested was from 100 kHz to up to 10000 kHz. The travel speeds of the stage explored were 1, 5, 10, 20, and 50 mm/s. Hatching space was 30 and 70 μm. The laser power was from 1 to 10 W.

This equipment had a few optimizations to make it feasible for the PBF-LB process. To align and measure the beam size, an attenuator and a polarizing beam splitter with a beam sampler were added to the setup (Figure 5.1a on page 73). The beam size was captured in an HD camera for future measurements (Figure 5.1b on page 73). To avoid oxidation and powder flow, a chamber was built and designed to operate with positive pressure and Ar gas flowing at a constant rate.

The melting process was limited to working with only one powder layer. This was added manually to the Cu cup and compacted with a flat glass substrate. Before starting the melting process, the chamber was purged with Ar for 10 minutes to displace as much oxygen as possible. No oxygen sensors were used to regulate the atmosphere.

Table 5.1 Chemical composition of powder samples. Commercial CoCr atomized values were provided by the vendor.

Material	Element (wt. %)								
	C	P	Ni	Mg	W	Fe	Si	Cr	Co
Commercial CoCr atomized powder	[0.05-0.15]	[0.04 max]	[9.00-11.00]	[1.00-2.00]	[14.00-16.00]	[3.00 max]	[0.4 max]	[22-33]	base
CoCr milled powder	-	-	-	-	-	-	-	22.6	77.4

Table 5.2 Experimental settings utilized for high-energy ball milling. Stainless steel (SS) and tungsten carbide (WC) jars were utilized.

Experiment number	Jar material	Total number of cycles and milling time	Total milling time (hours)	PCA (Stearic Acid)	SiC NPs	Yield after Milling	Yield after sieved (-45μm)
1	SS	150 cycles (10 on/15 off)	5	-	1% vol	92%	74%
1	SS	150 cycles (10 on/15 off)	5	1% w	1% vol	100%	75%
2	SS	150 cycles (2 on/4 off)	5	-	1% vol	97%	74%
2	SS	150 cycles (2 on/4 off)	5	1%w	1% vol	101%	73%
3	SS	60 cycles (2 on/4 off)	2	-	1% vol	83%	72%
3	SS	60 cycles (2 on/4 off)	2	1%w	1% vol	116%	8%
4	SS	300 cycles (2 on/4 off)	10	-	1% vol	76%	75%

Table 5.2 Continued

4	SS	300 cycles (2 on/4 off)	10	1%w	1% vol	73%	70%
5	SS	150 cycles (2 on/4 off)	5	-	2% vol	92%	80%
5	SS	150 cycles (2 on/4 off)	5	-	4%vol	87%	90%
6	SS	300 cycles (2 on/4 off)	10	-	2% vol	85%	80%
6	SS	300 cycles (2 on/4 off)	10	-	4%vol	90%	80%
7	WC	30 cycles (10 on / 15 off)	1	-	-	92%	68%
8	WC	150 cycles (2 on / 4 off)	5	-	-	92%	64%
9	WC	300 cycles (2 on / 4 off)	10	-	-	107%	47%
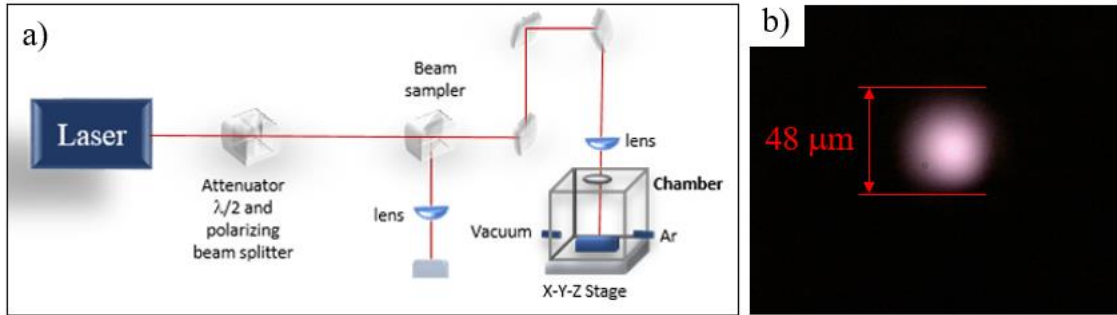
Figure 5.1 a) Femtosecond laser setup. b) Beam diameter.

5.3.3.2 Laser powder bed fusion with continuous laser

The second technique explored was laser powder bed fusion (PBF-LB). A ProX DMP 200 machine from 3D Systems was used. This system is an entry-level 3D printer optimal for manufacturing small volumes (140 x 140 x 125 mm) along with semi-automated material loading. The machine is equipped with a 400 W fiber laser with a wavelength of 1070 nm and a spot size of 100 μm. The printing speed was constant at a value of 1000 mm/s. Additional settings, including hatching space and strategy, were also constant due to operational limitations in the computer control system. The DMP system used nitrogen gas as a cover gas to create an inert atmosphere in the print chamber.

At least 1-2 kg of powder is required for the 3D printer to operate properly. Due to the low as milled powder available (~100 g), a few modifications in the feed piston and plate were necessary to guarantee its operation for lower volumes of powder (Figure 5.2). To ensure that each layer was uniform, the scraper was set to a constant layer thickness of 30 μm. The function of the scraper was to carry out actions of layering such as spreading, smoothing, and compacting from the feeding piston to the sintering plate. With this technique, the printing of multiple layers was possible. In this case, only 20 consecutive layers were printed, corresponding to 600 μm total height. A graphite disk was inserted into the sintering plate to easily remove the printed specimens, which tend to break when printed directly from the stainless steel plate.
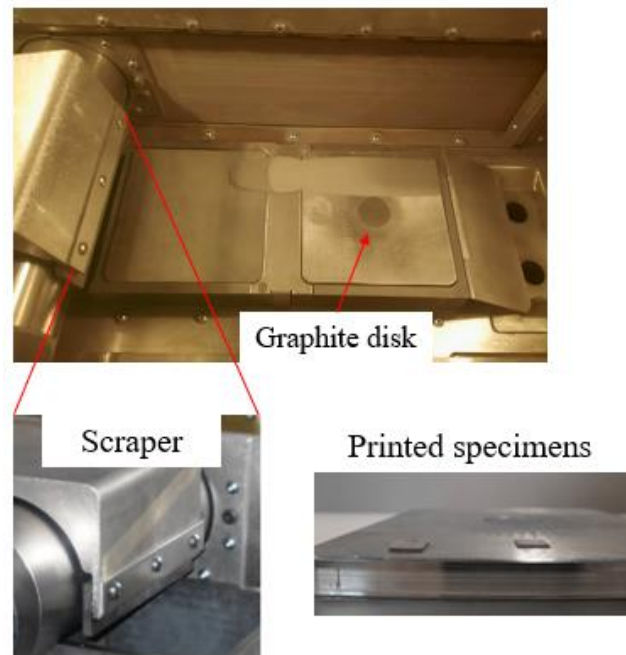
Figure 5.2 Inside view of the ProX DMP 200 machine. The graphite disk was inserted for issue removal of the sample after the printing.

5.3.3.3 Direct energy deposition with continuous laser

The last technique tested was direct energy deposition (DED) using a continuous blue laser. The samples were fabricated using a Formalloy L221 DED system equipped with a NUBURU AO-500 BETA blue laser with a wavelength of 450nm and a spot size of 1 mm. An argon-filled inert chamber with oxygen content below 5 ppm was used.

A 4.57 mm-thick 304 stainless steel substrate was mounted to the water-cooled positioning stage. On top of the substrate, layers of 0.1-mm-thick 304SS foil, which was machined with a cavity on the building site to create the space for powders, were affixed by tungsten blocks to ensure intimate contact by gravity. CoCr powder was manually poured into the cavity and flattened by an aluminum blade to imitate the operation of the robotic arm in typical selective laser melting (SLM) machines so that a thin and uniform powder layer was deposited. The thickness of the powder layer was controlled by adjusting the number of 304ss foils. As the laser scanned across the 10 x 10 mm building region, the CoCr powder was fused together to form a dense layer of the material. Subsequently, more 304SS foils with identical cavities were added to the top, and the operation described above was repeated to build the next layer. The position of the laser head was correspondingly adjusted to ensure the focus was maintained as the sample increased in build height.

In the present work, CoCr samples were built with 450 W laser power, 0.25 mm hatching distance, 1000 mm/min scanning speed, and 0.2 mm powder bed thickness. In addition, the laser scanned twice for each layer to ensure the density and improve the surface quality of the samples.

The use of this equipment was in collaboration with Dr. Kenneth Vecchio at the University of San Diego in the Materials Science and Engineering Department.

5.4   Results and discussion

5.4.1   Powder production by high-energy ball milling

By implementing ball milling as a method for powder production for SLM processes, various requirements should be met, including particle size distribution, morphology, and flowability. Size distribution and shape are reported to have the greatest influence on the powder packing density. This is critical for SLM additive manufacturing as packing density is proportionally correlated with the powder bed density and part densification [18]. When the powder bed density is high, good densification in the parts is achieved [19]. As broader size distributions are typically attained in ball milling, flowability and spreadability are the two main properties to consider in avoiding defect formation in the as-printed parts. Figure 5.3 compares commercial atomized virgin powder versus the same powder after milling for 12 hours. As expected, irregular shapes and wider size distribution were obtained in the milled powder compared to atomized powder. However, most of the powder was concentrated below 45 μm, similar to the virgin condition.
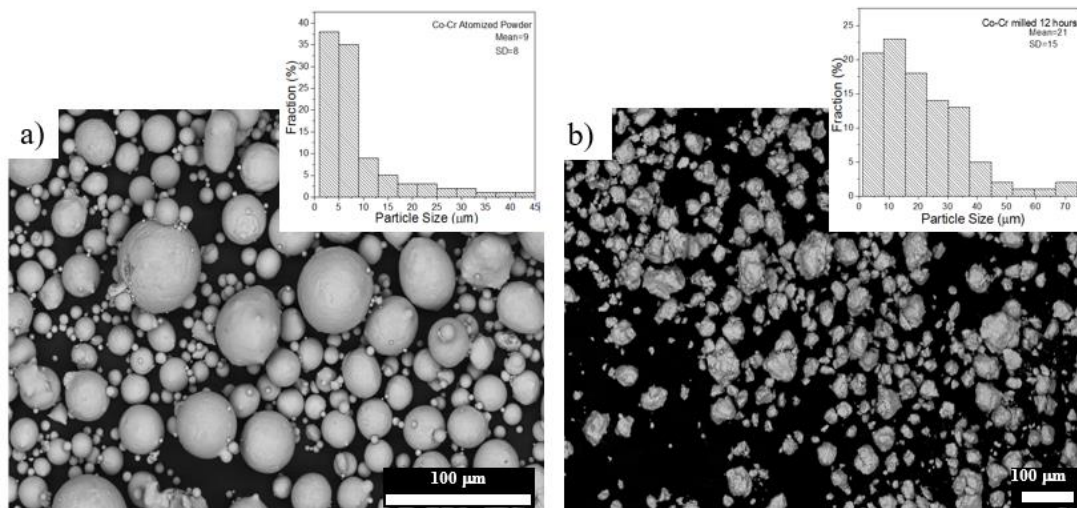
Figure 5.3 Comparison of particle size distribution and morphology of CoCr atomized and milled powder.

Due to higher driving forces during the mechanical deformation, the grain size of the as-milled powder was almost ten times smaller than atomized powder (Figure 5.4a-b). This can be advantageous as retained microstrain could improve the nucleation rate and refine microstructures during the rapid solidification in the laser process [20]. If changes in chemical composition cause grain refinement, the segregated elements could also work as nucleants. However, EDS was executed in a few particle cross-sections cut by Focused Ion Beam (FIB), and no segregation was observed (Figure 5.4c).
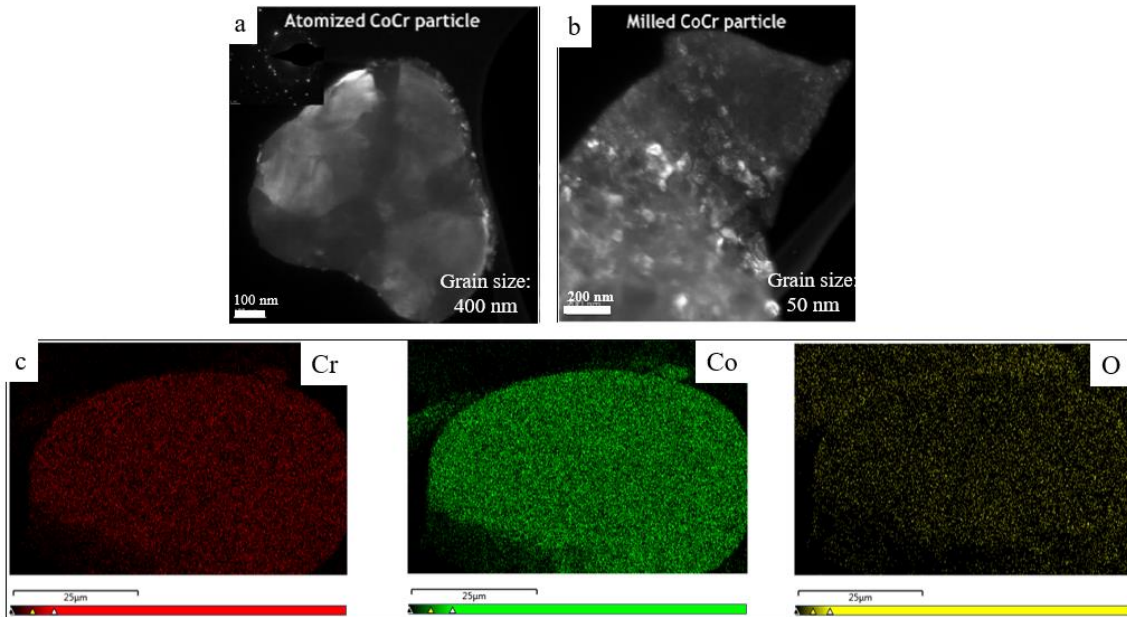
Figure 5.4 Comparison of grain sizes of particle cross-section for the atomized powder (a) and milled powder (b). EDS maps of a milled particle showed a uniform distribution of Co and Cr (c). No segregation was observed.

Figure 5.5 exhibits the phase fraction of both powder conditions. Both powder batches consisted of dual FCC/HCP phases. However, the intensity of the γ-Co FCC peaks was highly reduced in the as-milled powders. The XRD pattern of the milled powders showed a broadening of the peaks and decreased intensity. This behavior occurs due to the presence of residual strain in the lattice by introducing crystalline defects. The retention of the metastable FCC phase in the atomized powder can be attributed to the high cooling rates. The decrease of this phase in the milled powder may be assigned to strain-induced martensitic transformation, leading to the transformation of some amount of the γ-Co FCC phase to the ε-Co HCP phase [21]. This allotropic transformation has been previously reported in various investigations [22,23]. Louidi et al. [22] investigated such transformation even further by analyzing different compositions of elemental Co-Cr powders and a broad range of milling times. They reported that all the

allotropic transformations this system experiences during ball milling are primarily related to the increase of dislocation and the accumulation of two types of stacking faults, twin and deformation faults.

Louidi et al. [22] reported that at the beginning of the milling process, the increase in stacking fault probability (SFP) increases for both phases, the FFC and the HCP. However, for a concentration of 20% Cr (similar to this current study) and milling times below 6 hours, the SFP in the HCP phase is slightly below the FCC phase. This means the HCP phase is more stable as more ordered planes (number of planes between two neighboring stacking faults) are present. Consequently, this will lead to the transformation of the FCC to the HCP phase. However, the FCC phase is usually partly converted into the HCP phase because longer milling times are required to complete the transformation.
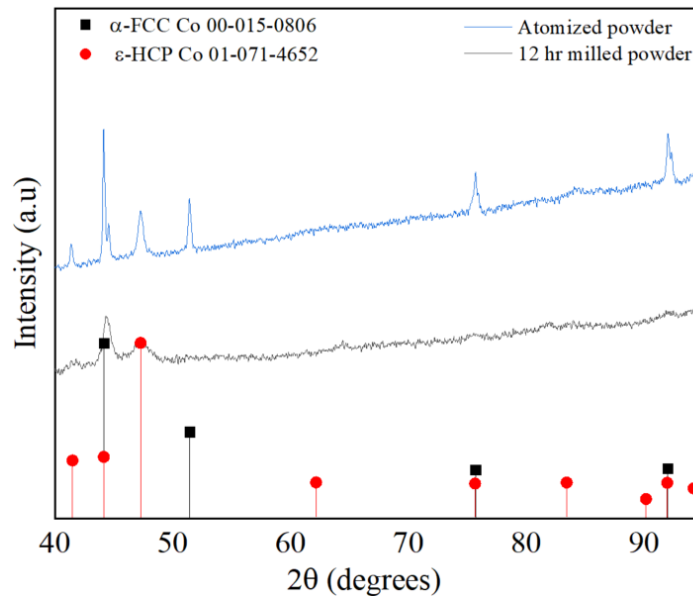
Figure 5.5 XRD patterns of CoCr atomized (blue) and milled (black) powder.

Since it was proved that a reasonable particle size distribution and high production yield (>90% below 75 μm) was achieved in the milled powder, the next step was to attempt powder production by alloying elemental Co and Cr powders. Powder properties are associated with specific processes and device characteristics. Therefore, the powder production was evaluated as a function of speed, mill time, and ball-to-weight ratio. Additionally, various particle control agents (PCA) and compositions were tested to control the phase fraction and production yield. It is important to mention that PCA is absorbed on the surface of the particles to reduce the surface and interfacial energy between the particles and the ball, thus avoiding the agglomeration problem and coarsening of the particles. However, based on the data

obtained, the effect of PCA was contradictory when SiC NPs were added. This will be discussed later in Figure 5.10.

Three different alloy mechanical processes were tested, including planetary, cryogenic, and high energy (SPEX) ball milling. Planetary and cryogenic milling were inadequate for powder production under all the conditions tested, as size distribution could not be controlled (Figure 5.6). Cryogenic milling is a technique that reduces cold welding of the powders, therefore it was only implemented in the CoCr + WC composite synthesis as this composition presented the highest cold welding and the lowest yield (Figure 5.6c). When using cryogenic temperatures, the fragmentation stage occurs more readily than cold welding, and as a result, the powder particle size and agglomeration decreased [24]. The particle size distribution of CoCr + WC improved significantly compared to planetary milling, and the addition of PCA (1 wt. % stearic acid) also promoted control in size distribution. However, the powder presented a flake morphology, which is inadequate for SLM processes.
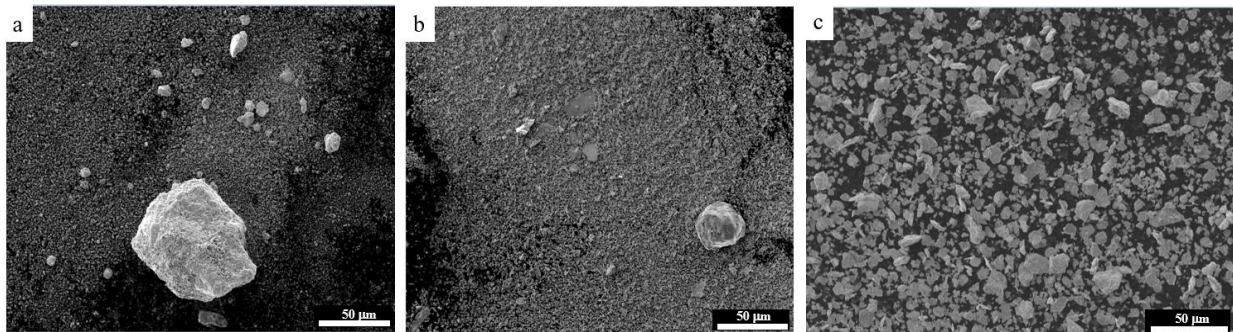
Figure 5.6 Comparison of powder batches produced by planetary and cryogenic milling. a) CoCr+WC with PCA and milled for 2 hours b) CoCr + 1wt. % SiC with PCA and milled for 2 hours. c) CoCr+WC after cryomilling for 5 hours.

High-energy ball milling was the third method tested. Adding PCA (1 wt. % stearic acid) was detrimental in obtaining a uniform morphology and well-distributed particle size for both systems (Figure 5.7 and Figure 5.8). In the case of CoCr+WC (Figure 5.7), adding PCA resulted in a production yield of only 47%. Additionally, the flowability of this powder could not be executed as the powder was retained in the nozzle. This could be attributed to the high volume of finer particles and the possibility of moisture retention causing an increase in the interparticle adhesion. Due to the negative results obtained, the CoCr + WC system was discarded for further investigations.
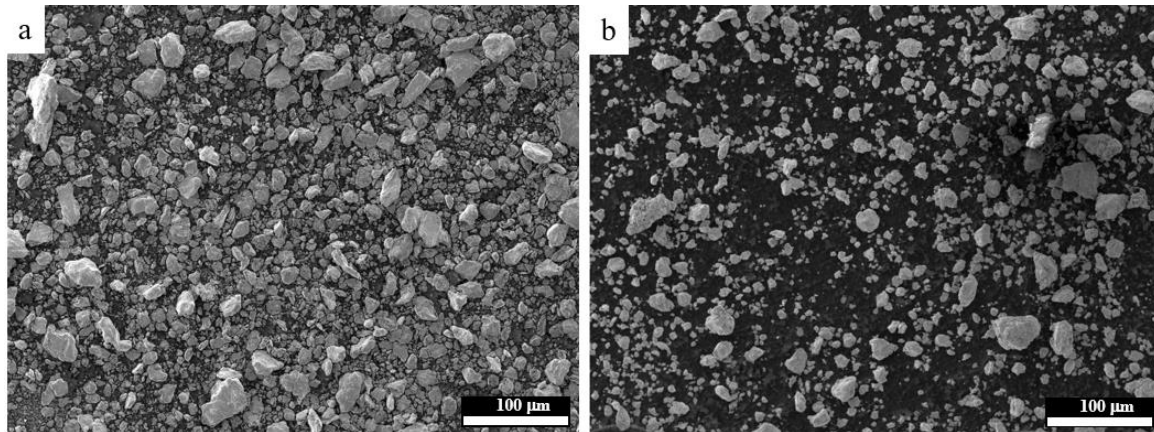
Figure 5.7 CoCr+WC powder obtained with high-energy ball milling. a) PCA was used, and a yield of 60% was obtained. b) No PCA was added, resulting in a yield of 47%. All powder batches were sieved below 45 μm.

The study of the granulometry evolution for CoCr + 1 wt.% SiC can be observed in Figure 5.8 on page 80. For this system, the most satisfactory milling time was 10 hours, with cycles of 2 min on and 4 min off. Figure 5.8 shows the results of the milling times tested with and without the addition of PCA. As mentioned before, powder agglomeration was persistent with the addition of PCA (Figure 5.8 a-c). Among the three options without PCA (Figure 5.8 d-f), the most successful powder batch was produced after 10 hours. A Gaussian particle size distribution was observed in this sample, indicating a good distribution of fine and coarser particles below 45 mm (similar to the as-virgin condition). This size distribution could be beneficial for better spreadability on the build plate, as a decrease in the surface-to-volume ratio is possible. Consequently, the powder might be less affected by interparticle friction, Van der Waals forces, and agglomeration. The average size obtained after 10 hours was also the closest to the atomized powder. For all the above reasons, the sample from Figure 5.8 f was selected for the subsequent laser melting experiments.

XRD was carried out to investigate the phase fractions for the CoCr + 1wt.% SiC sample milled for 10 hours (Figure 5.9 on page 81). The effect of PCA was evident as only the Co-FCC phase was obtained. Conversely, the Co-HCP phase was predominant in the absence of PCA. Literature has reported that the right PCAs can accelerate the mechanosynthesis reactions to some extent [25]. The differences between a residual strain with and without PCA may lead to an increase in energy that influences the formation of different phases.
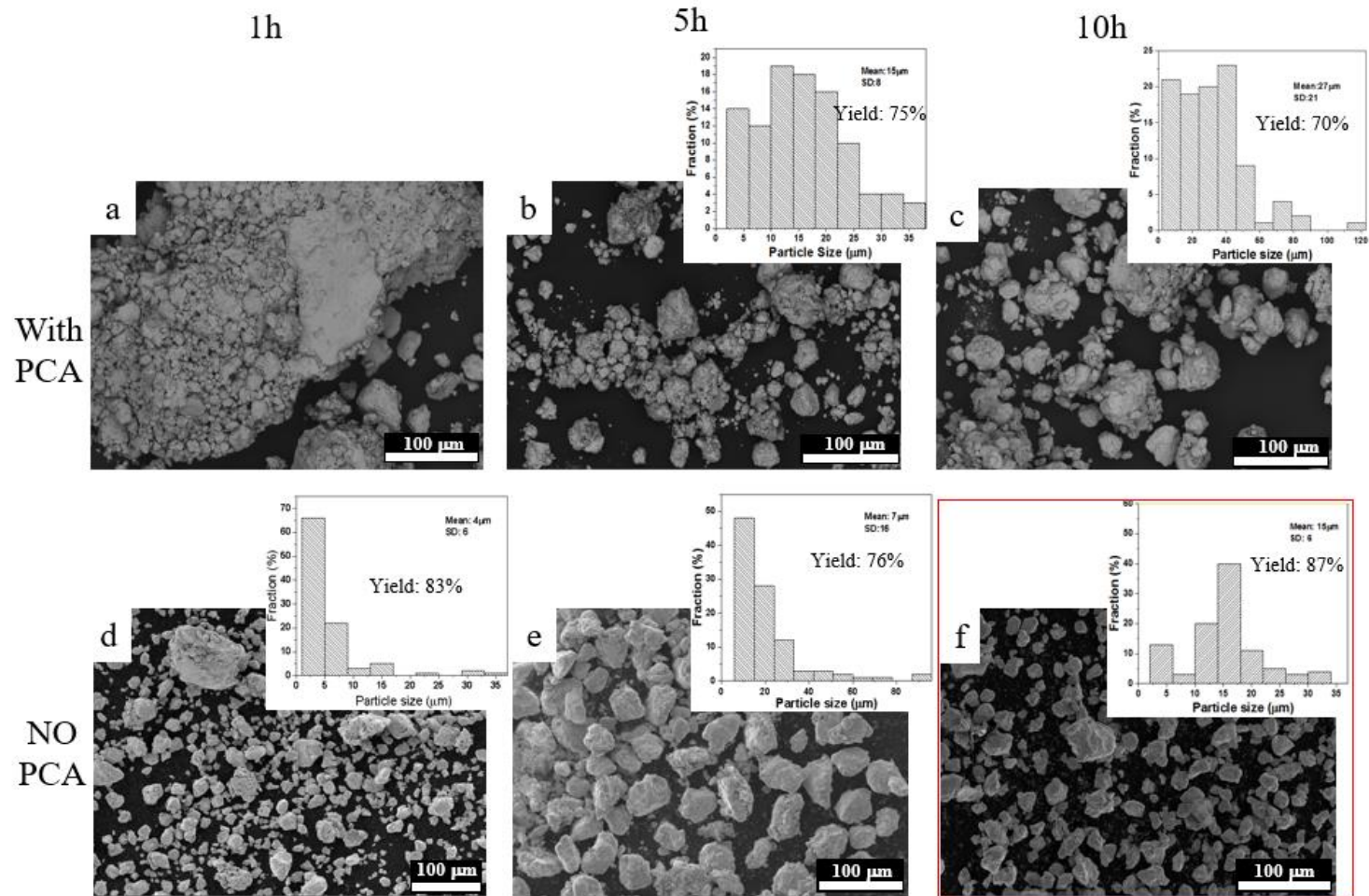
Figure 5.8 CoCr+SiC powder synthesis by high-energy ball milling. a-c) No addition of PCA. d-f) Addition of 1 wt.% stearic acid. The powder was milled for 1, 5, and 10 hours. The sample highlighted in red corresponds to the selected sample for the melting process.
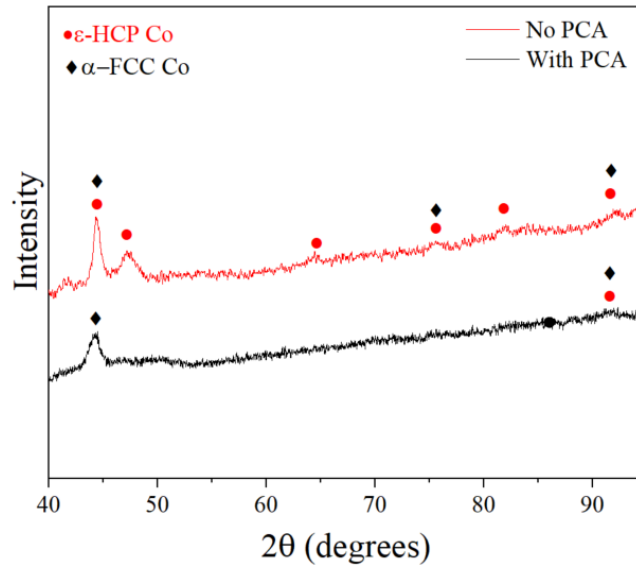
Figure 5.9 XRD patterns of CoCr+SiC after being milled with and without PCA. SPEX equipment was used.

Additional weight concentrations of SiC NPs mixed in with the CoCr were tested. These powder batches were milled for 10 hours for comparison purposes. Figure 5.10 illustrates the morphological and size distribution of the milled powder with 2 wt.% and 4 wt.% of SiC NPs. Particle agglomeration was no longer controlled regardless of the high production yields after sieving. Negative impacts on the densification of the parts and mechanical properties have been reported with higher NPs content [26]. This is due to the non-homogenous distribution on powder surfaces. For example, in the case of aluminum matrix composites reinforced with 10 vol.% Al_2O_3 and 10 vol.% SiC of microscale reinforcements, the yield strength was inferior to those reinforced with only 3 vol.% Al_2O_3 nanoparticles [27].
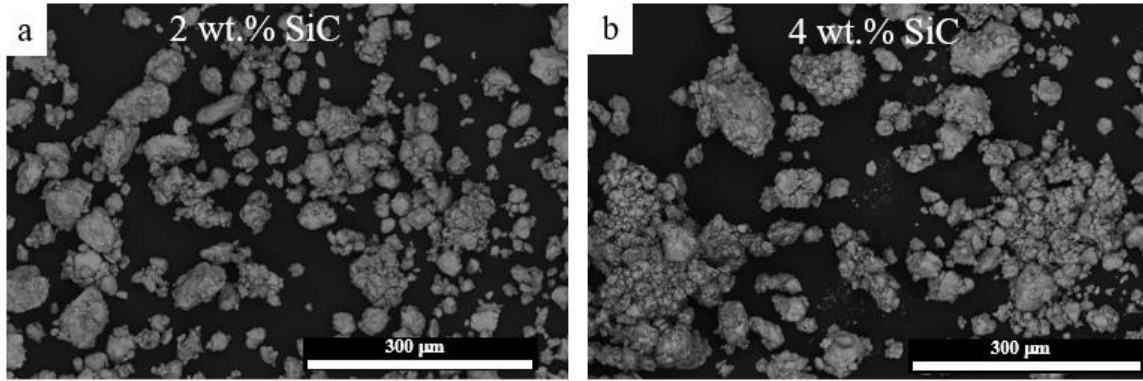
Figure 5.10 Higher weight percentages of SiC NPs were added to evaluate the evolution of powder morphology, size, and agglomeration. a) 2 wt.% SiC NPs and b) 4 wt.% SiC NPs.

5.4.2 Laser processing

To melt the CoCr+SiC system, various custom-made laser processing techniques were implemented to process a low powder volume. To date, one of the biggest challenges is that industrial machines are not designed to work with small volumes, e.g., less than 100 grams of powder. Therefore, for alloy development in the SLM techniques, it is imperative to develop alternatives that allow the printing of small specimens to reduce research and development cost and waste.

5.4.2.1 Femtosecond laser processing

Because of the ultra-short pulses and ultra-high power intensity ($>10^{14}$ Wcm^{-2}) involved, femtosecond (fs) lasers can be used to process almost any material with high quality and high precision. Due to the lack of information about fs-lasers in additive manufacturing, several parameters had to be tested to find the optimal processing window. In Figure 5.11, the parameters that showed better results are enclosed in the red circle. This graph shows the volume energy density (VED) as a function of peak power. In this case, peak power was selected to better illustrate the high energy available using this equipment compared to continuous lasers for PBF-LB, which is 1×10^6 times smaller. When the laser scanning speed was less than 20 mm/s, overheating was severe and could not be avoided due to the accumulation of localized energy. As a result, the powder combusted. For this reason, these speeds were no longer considered in attempts to melt the material.

With speeds above 50 mm/s, the powder melted more homogeneously. We found that the threshold using this speed using power from 1W to 10W was frequencies between 315 kHz and 2000 kHz. The only exception found was that with power equal to 1W, a frequency of 100KHz could be used to melt the material (power peak = 2.86×10^7, shown in Figure 5.11 in area enclosed inside the red circle). It is important to mention that material produced at lower speeds and frequencies was blasted away from the

powder bed. The strong removal of the loose powder can be explained by the generation and accumulation of shockwaves combined with vaporized material caused at very high pressures. Another important consideration in fs-laser processing techniques for AM is that material ablation of the printed part may occur. The high peak power in a short time can cause blasting forces from electric charges, such as hot electron blasts, Coulomb explosions, or repulsions. However, these phenomena were not evaluated in this study.
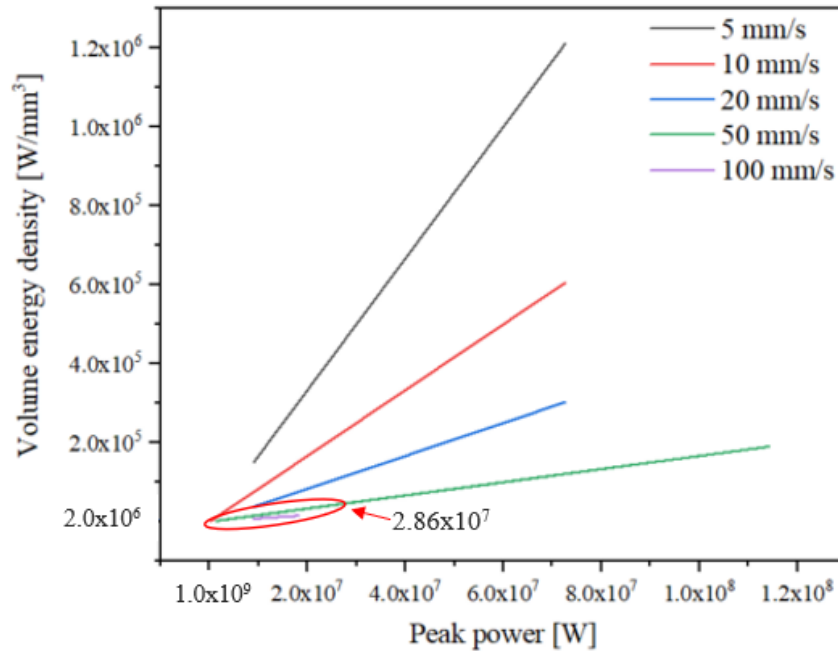
Figure 5.11 Volume energy density as a function of peak power for all the conditions tested. Average power, travel speed, and frequency were modified while beam diameter, hatching space, and layer thickness remained constant.

Figure 5.12 shows three examples of the samples obtained using the conditions within the process window highlighted in Figure 5.11. When using atomized powder (Figure 5.12a), the material only partially melted. On the contrary, the material was fully melted when using milled powder (Figure 5.12b-c). Some possible reasons why the as-milled powder melted under the same laser conditions might be related to the residual strain within the microstructure, which may cause less energy input to be required to melt. Additionally, changes in chemistry could also contribute to the differences in the melting point.
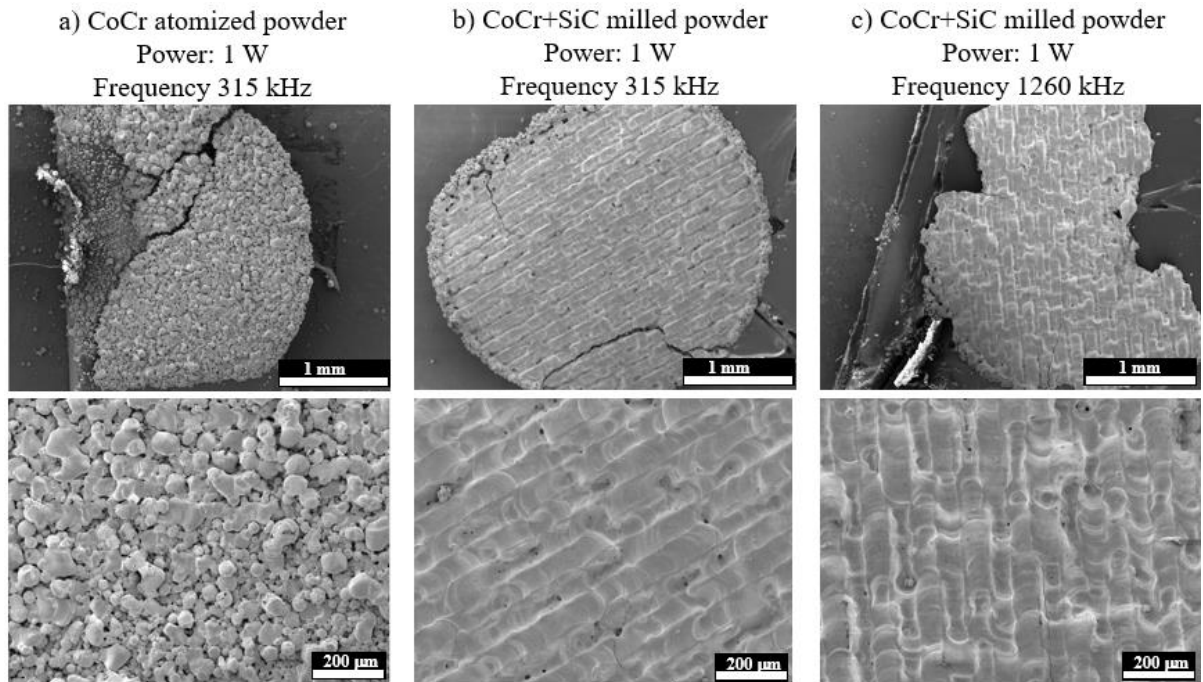
Figure 5.12 Comparison of CoCr and CoCr+SiC single-layer samples processed by the same parameters. No major differences were observed in the milled powder using the lowest and highest frequency within the process window.

The melting and densification of the single layers of as-milled powder is poor compared with industrial PBF-LB processes. Further, when higher powers were input to increase the energy density, the equipment experienced technical difficulties. Therefore, we could not explore the full power capacity of this equipment. For illustrative purposes, Figure 5.13 shows the complete range of maximum power possible. As enclosed in the blue circle, the maximum peak power and VED possible would be 4.54×10^8 W and 7.56×10^5 W/mm^3, respectively. These values represent a significant difference compared with the settings tested (section enclosed within the red circle). This technique has great potential in SLM based on its high energy density. However, due to the low penetration and ablation issues, the setup should be drastically modified to make it relevant for PBF-LB purposes. Ullsperger et al. [28] showed that it is possible to melt Al-Si alloys with a maximum relative density of 95%. They did not report the laser setup, but the settings were similar to the ones we implemented in this study. They also reported that the most successful samples were melted using an average power of 25 W, a speed of 200 mm/s, and a frequency of 10 MHz.

An additional challenge in the molten samples was that the singles layers experienced cracking immediately after removing them, impeding subsequent characterization. To obtain meaningful data about this material, a more homogenous melting is required to analyze the samples properly. Multiple

layers are also a requirement to evaluate the microstructure to confirm if grain size reduction is possible with the addition of SiC NPs. However, with the setup available, the completion of these requirements was not possible. For this reason, continuous lasers were selected as an alternative to obtaining the necessary improvements.
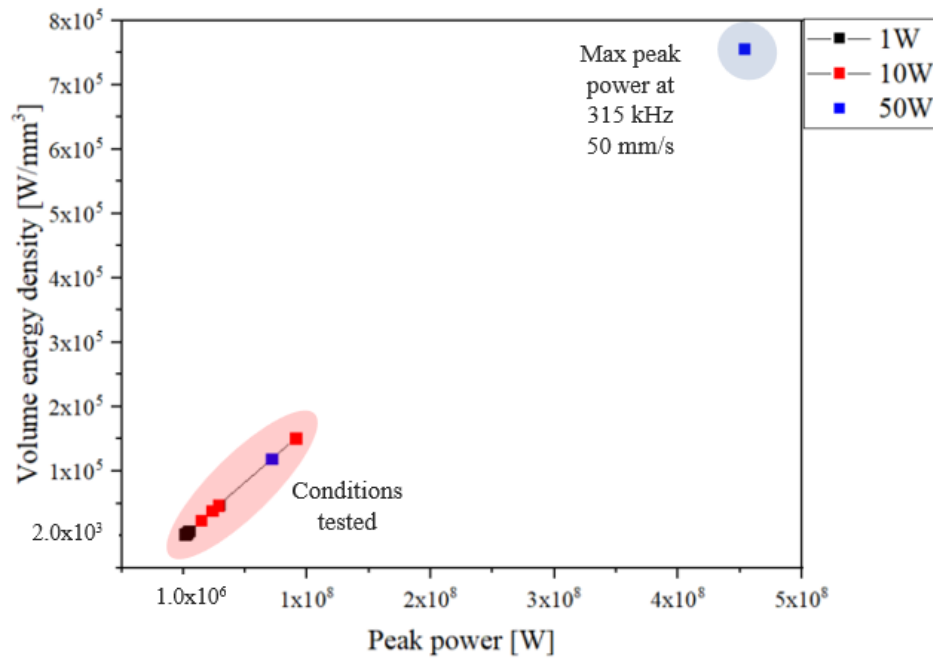
Figure 5.13 Volume energy density as a function of peak power for all the minimum (red) and maximum (blue) parameters available with the fs-laser.

5.4.2.2 Powder bed fusion process using a continuous laser.

Laser powder bed fusion was the first approach implemented using a continuous laser. Among the advantages of using the Pro-X DMP 200 were the evaluation and improvements of powder spreadability, printing of multiple consecutive layers, and better control of the inert atmosphere inside the chamber. The powder spreadability was evaluated by comparing the virgin and as-milled powder differences. This step was critical to improving the settings of the mill conditions to obtain proper PSD and therefore to overcome issues related to the lack of powder spread in the bed. Figure 5.14b-c illustrates the before and after the PSD was improved. We observed that when PCA was not added and a Gaussian PSD was obtained, the powder spread more homogeneously than the virgin powder (Figure 5.14a, c). For reference, the powder batches illustrated in Figure 5.8 b and f on page 80 correspond to the powder shown in Figure 5.14 b-c, respectively. Due to this improvement, multiple layers were consecutively printed.
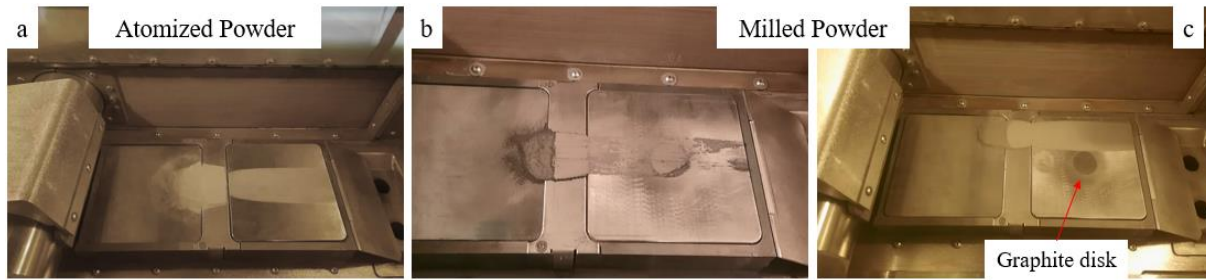
Figure 5.14 a) Atomized powder spread in the powder bed. b-c) Milled powder spreadability evolution before and after the PSD was improved.

Optimization of the melting process was challenging as most of the machine settings are not able to be modified given the proprietary design of the 3D Systems machine. As shown in Figure 5.15, the complete powder melting was unsuccessful with the settings used. Since the scan speed was a fixed parameter, power and layer thickness were the only settings tested to improve the process. When using the minimum layer thickness of 30 μm and a maximum power of 240 W, the material did not melt homogeneously. Possible reasons for the defects observed might be related to inconsistencies in the powder spreadability, as no compacting forces were exerted by the roller. Therefore, the lack of control in powder packing density could lead to a lack of fusion in the final printed parts. Additionally, the adhesion of the specimens with the build plate was not strong and irregular surfaces were observed. This could cause the rupture of the layers when the scraper added powder. This can further hinder surface wetting conditions, causing a subsequent decrease in layer adherence and densification while contributing to AM part porosity.
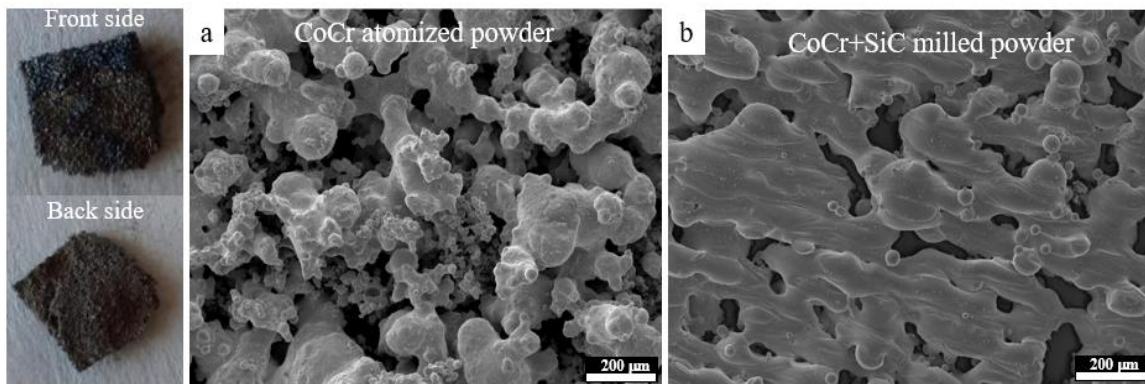
Figure 5.15 CoCr atomized (a) and CoCr+SiC milled (b) powders after they were processed with a continuous laser. A maximum power of 240 W was used with a layer thickness of 30 μm. A total of 20 layers were printed.

The challenges observed with the CW laser technique were mainly related to the process. This equipment does not have the conditions necessary to manipulate low powder volumes. Additionally, the lack of freedom to adjust the settings drastically limited the process window. As shown in Table 5.3, the volume energy densities selected in this study were close to the ones reported by Li et al. [29], in which they successfully printed full-density parts. However, the layer thickness and speed they reported were slightly different compared to our study. Additionally, the dimensions of the printed specimens were significantly bigger, above 5 cm in length and 1 cm in thickness, indicating that at least a few kilograms of powder were utilized. A higher number of layers could reduce the defects, as at the first layers, roughness and lack of fusion can occur [16]. Based on the data provided by Wang et al. [30], a power of 175 W was enough to melt the CoCr alloy fully. This power was below those we tested, but their reported speed was half of what we used, thereby providing a higher volume density in their study.

Table 5.3 Minimum and maximum laser parameters tested in this study compared to similar investigations reported in the literature.

Beam diameter [μm]	Hatching space [μm]	Layer thickness [μm]	Average Power [W]	Speed [mm/s]	Volume energy density [W/mm^3]	Specimen density (%)	Reference
100	-	30	180	1000	60	-	Current study
100	-	30	240	1000	80	-	Current study
100	80	40	325	1120	73	>99	10
80	110	25	175	550	159	>99	11

Despite the lack of bulk melting in our studies, some small areas (100 mm^2, approximately) successfully melted (Figure 5.16). The sample printed with milled powder (Figure 5.16b) was further characterized to discover if SiC NPs were present in the microstructure. TEM data (Figure 5.16c) showed only the presence of Cr_2O_3 oxide, δ-Co, and ε-Co and no traces of SiC were found. The delta phase was not present in the x-ray diffractogram (Figure 5.17), probably due to a resolution limit or the small surface area available for a scan. In the case of SiC NPs, it is possible that their weight fraction and size are too small that were not captured in the TEM and XRD data respectively. The oxide inclusions might have been the by-product of oxides present in the powder and also due to high oxygen levels inside the chamber (>1500 ppm). Contrary to our study, PBF-LB samples reported by various researchers [31,32] showed the γ-Co (FCC) phase as the primary phase with a small percentage of the ε-Co (HCP) phase.

More recently, Li et al. [29] reported SLM specimens with only the γ-Co phase. Wang et al. [30] reported 95 % HCP and 5% FCC phases, similar to our results. Further explanation of phases in the CoCr alloy will be provided in section 5.4.2.3. Compared to steel or aluminum alloys, it is evident that CoCr-based alloy is very susceptible to differences in the process parameters, mainly the cooling conditions that can lead to phase transformations and segregation.
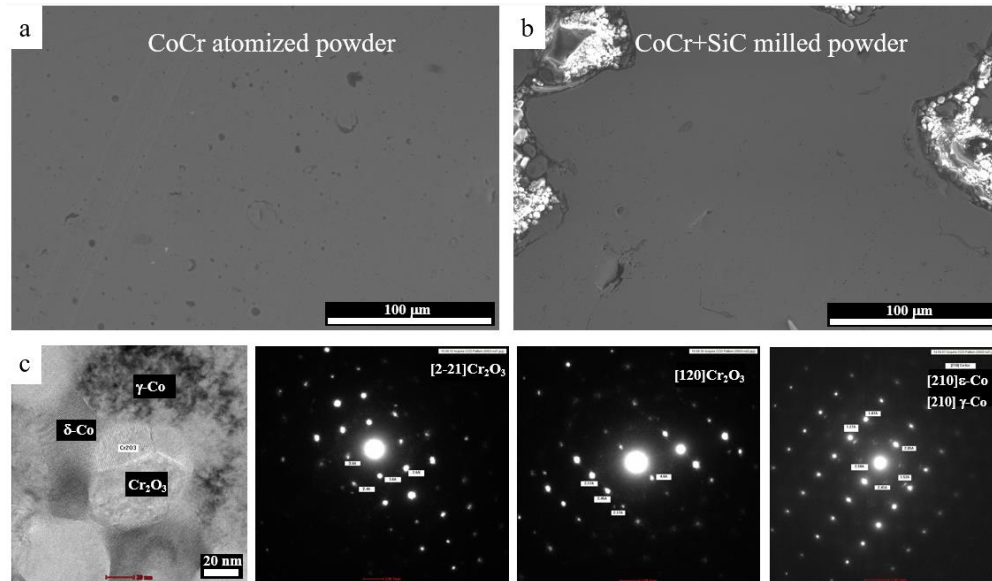
Figure 5.16 Melted areas of atomized (a) and milled (b) powder after being processed by the same laser parameters. c) Various phases were detected in the milled powder.
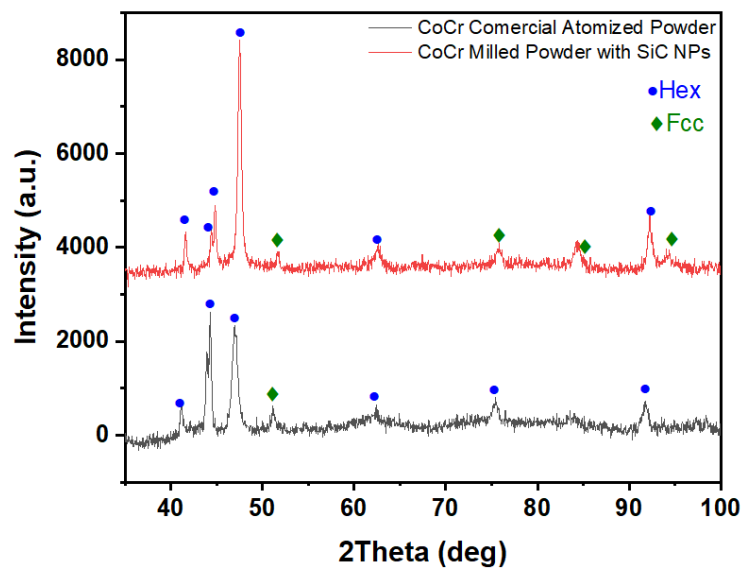
Figure 5.17 XRD pattern of atomized and milled powder after being processed by PBF-LB.

5.4.2.3   Direct energy deposition using a continuous blue laser.

Due to the lack of fusion observed in the previous femtosecond and PBF-LB processes, a higher-power blue laser in combination with Direct Energy Deposition (DED) was implemented. The set-up was significantly improved based on the previous challenges in powder spreadability and the inability to process more than 20 consecutive layers. Cobalt absorbs blue light (450 nm) better than the 1070 nm wavelength used in the previous two laser techniques. The increase in absorption led to an observable improvement in the melting and solidification behavior compared to previous approaches. Density measurements of the parts via the Archimedes method revealed relative densities of 99.6 ± 0.2 % and 99.1 ± 0.2 % for samples CoCr and CoCr+SiC, respectively. As Xiao et al. [33] reported in their study using the same blue laser, even at lower power energy density values than those reported for IR CW lasers, the effective laser power of a blue laser could reach values equivalent to a ~5000 W IR laser. This is a substantial increase in effective heating due to the increase in absorption of the 450 nm wavelength.

Figure 5.18a on page 90 and Figure 5.20a on page 93 show the samples printed with commercial atomized CoCr and milled powder CoCr+SiC. At the bottom of the build, the CoCr sample primarily contains coarse columnar grains oriented parallel to the build direction. Moving away from the bottom of the sample, the columnar grains become narrower and more elongated. Closer to the substrate, the phase corresponds to FCC (Figure 5.18b) due to the mixing with the substrate. Co and Fe can form a solid solution in the high-temperature range, where the FCC structure is favored [34]. As the number of layers increases and Fe concentration decreases (purple scan in Figure 5.18c), the ε-Co HCP phase becomes dominant. Figure 5.19a on page 91 shows the coexistence of γ-FCC austenite and ε-HCP Co martensite phases in the microstructure with coarse and fine grains. A minor amount of BCC-Cr and σ-CoCr was observed as well. In regions with finer grain sizes, the FCC, BCC, and sigma phases are more segregated at the grain boundaries (Figure 5.19b).

The BCC phase is not commonly reported for AM CoCr alloys. However, the Co-Cr-W alloys have shown a correlation between BCC phases and the presence of $Co_5Cr_3Si_2$ nano precipitates [35]. Specifically, the later phase tends to initiate near amorphous oxides and/or along cell boundaries, where high concentrations of W and Si elements are found [35]. Despite the presence of precipitates in the CoCr alloy, no grain refinement was observed.

Figure 5.18 a) Grain size evolution along the build direction of the as-printed CoCr sample. b) EBSD map showing the predominant phases. Red corresponds to the ε-Co HCP phase, and blue to the γ-Co FCC phase. c) EDS scan along the build direction.
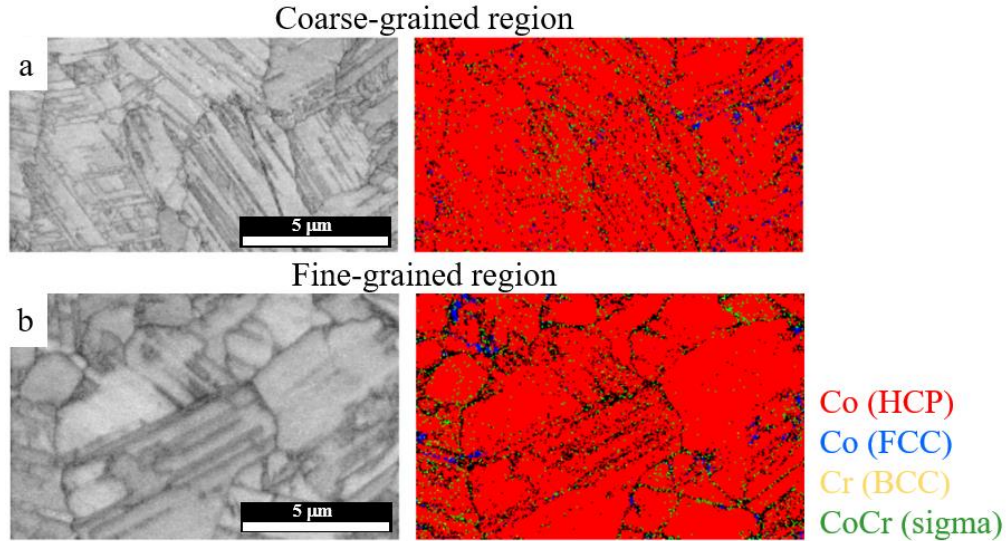
Figure 5.19 SEM micrographs and EBSD maps of the coarse- and fine-grained regions for the CoCr sample. Finer grains were predominantly closer to the top layers.

For the CoCr+SiC sample, the grain size and morphology changed considerably as equiaxed grains were dominant (Figure 5.20a on page 93). Like Figure 5.20a, the length and width of grains tend to become smaller toward the surface of the sample. However, the gradient of grain reduction along the build direction was more evident in this sample. This may be related to the combination of the continuous re-heat and re-melt of each layer in addition to the SiC nucleant particles, which could trigger the formation of more equiaxed grains. These particles control the solidification microstructure by developing a large constitutional supercooling zone ahead of the S/L interface. This causes a high density of heterogeneous nucleation sites, which induces near equiaxed grain formation [6]. The re-heating process facilitates the formation of equiaxed grains by providing a longer incubation time for the nucleation stage. The CoCr+SiC (Figure 5.20b) alloy showed an ε-HCP Co predominant phase along with a γ-Co FCC. Similar to the CoCr alloy, closer to the substrate, the main phase observed was FCC. The volume fraction of FCC is significantly higher along the microstructure than in the previous case without NPs.

More equiaxed grains were observed closer to the edge of the sample (Figure 5.21 a on page 94) due to the differences in chemical composition along the sample. The EDS scan showed the same trends in the decrease of Fe and increase of Co as the number of layers increased. The main difference in chemical composition was the increase of Si on the top layer and contaminants from the milling process (Figure 5.20c). We further confirmed that the top layer had a different composition than the rest of the sample. Figure 5.21 shows the presence of an impurity skin rich in Cr and Si on the surface. This indicates that SiC would not uniformly distribute in the bulk material. Instead, SiC is likely to float on the melt pool and consequently become the impurity layer on the sample surface. The contaminants from the jars and balls

91

might have also contributed to the segregation observed on the surface of the sample. However, there could still be remnants of nucleating particles within the melt pool that led to the formation of the smaller equiaxed grains (see Figure 5.22 on page 95).

Since the sample printed with virgin powder showed a higher volume of HCP phase, the formation of this phase might be associated with the laser process. The laser scan was applied twice per layer leading to constant re-heating of the previous layers. This can be considered as an annealing treatment for those layers, triggering the transformation from the FCC to the HCP phase. The FCC phase is usually formed first since the laser reaches temperatures above 1400 °C at which this phase is formed, and the faster cooling rate suppresses the formation of ε martensite. However, the martensitic transformation occurs during the re-heated of the formed region. If the temperatures reach 900 °C [36], the conditions will be sufficient for the formation of ε martensite, which transforms part of the γ-FCC phase into a more stable ε martensite at room temperature [37]. This study has no evidence of what phase was formed initially. Another possible reason for the formation of the HCP phase is the high power input used during the laser process. This could lead to an elevated concentration of high-density defects, including staking fault and dislocation, which can act as martensite nucleation sites [30].

Literature reports that the FCC and HCP phases not only depend on the process but the composition of the alloy elements Mo and W. As-built CoCrW alloys have been reported as duplex phase structures of γ-FCC and ε-HCP phases, although the FCC phase is predominant [37]. As-built CoCrMo alloys have been reported to mainly exist in the FCC phase. However, the FCC phase cannot be presented as the only phase for the CoCrMo systems, as there are some other studies [36] in which both phases are observed. In the case of the CoCr+SiC sample, the increase in the FCC phase volume fraction may be attributed to the SiC NPs additions and contaminants from the milling process. Segregation of certain elements could be a by-product of the contaminants. For example, higher concentrations of carbon and iron were present in the jars and balls, which could lead to a higher stabilization of the FCC phase if these elements segregated or are in a solid solution.

The bimodal structure of columnar and equiaxed grains was also confirmed by microhardness results (Figure 5.23), which showed that the columnar grain region from the CoCr sample has a lower hardness than the equiaxed grain region obtained with the milled powder. Additionally, for both samples, an increment of hardness was observed as the number of layers increased. As a result of the drastic reduction in grain size, the CoCr sample showed a more significant increment in hardness of 26% from the region closer to the substrate to the top of the sample. In contrast to the CoCr+SiC sample, the grain size evolution was more uniform leading to only an increase in hardness of only 9% from the bottom to the top of the sample.
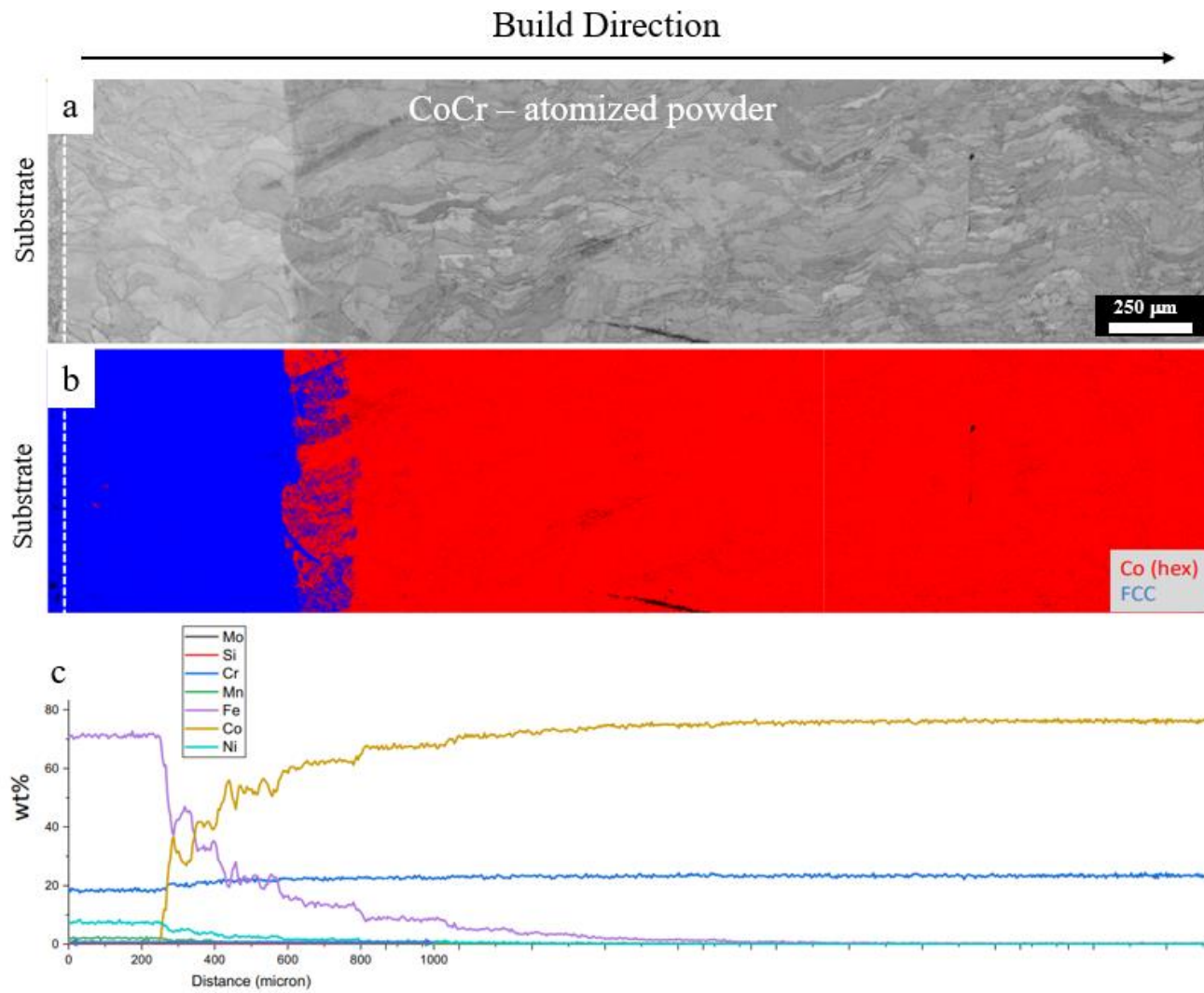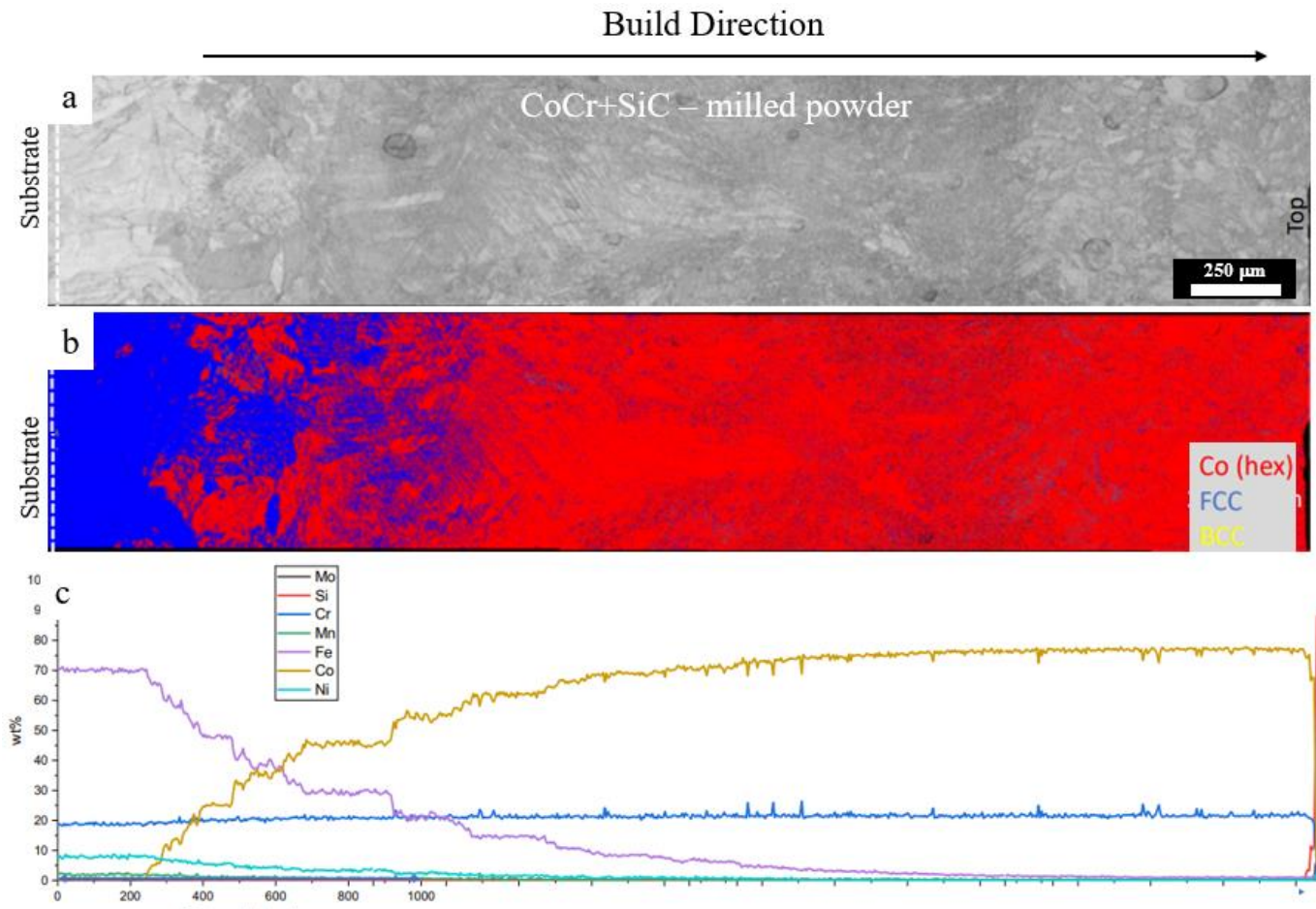
Figure 5.20 a) Grain size evolution along the build direction of the as-printed CoCr+SiC sample. b) EBSD map showing the predominant phases. Red corresponds to the ε-Co HCP phase, blue to the γ-Co FCC phase, and yellow to the BCC Cr phase. c) EDS scan along the build direction.
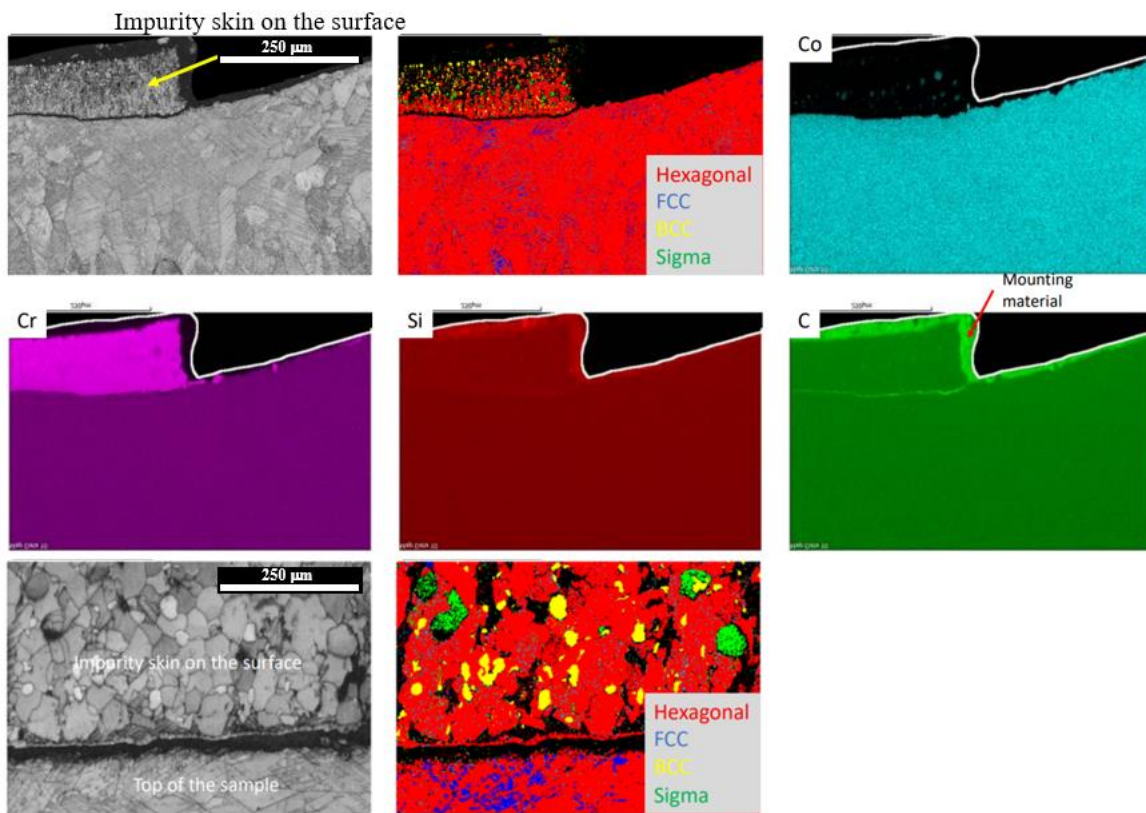
Figure 5.21 Higher magnification of the top of the CoCr+SiC sample. Impurity skin was deposited at the top layer. EBSD maps show the presence of multiple phases and EDS the segregation of Cr and Si elements.
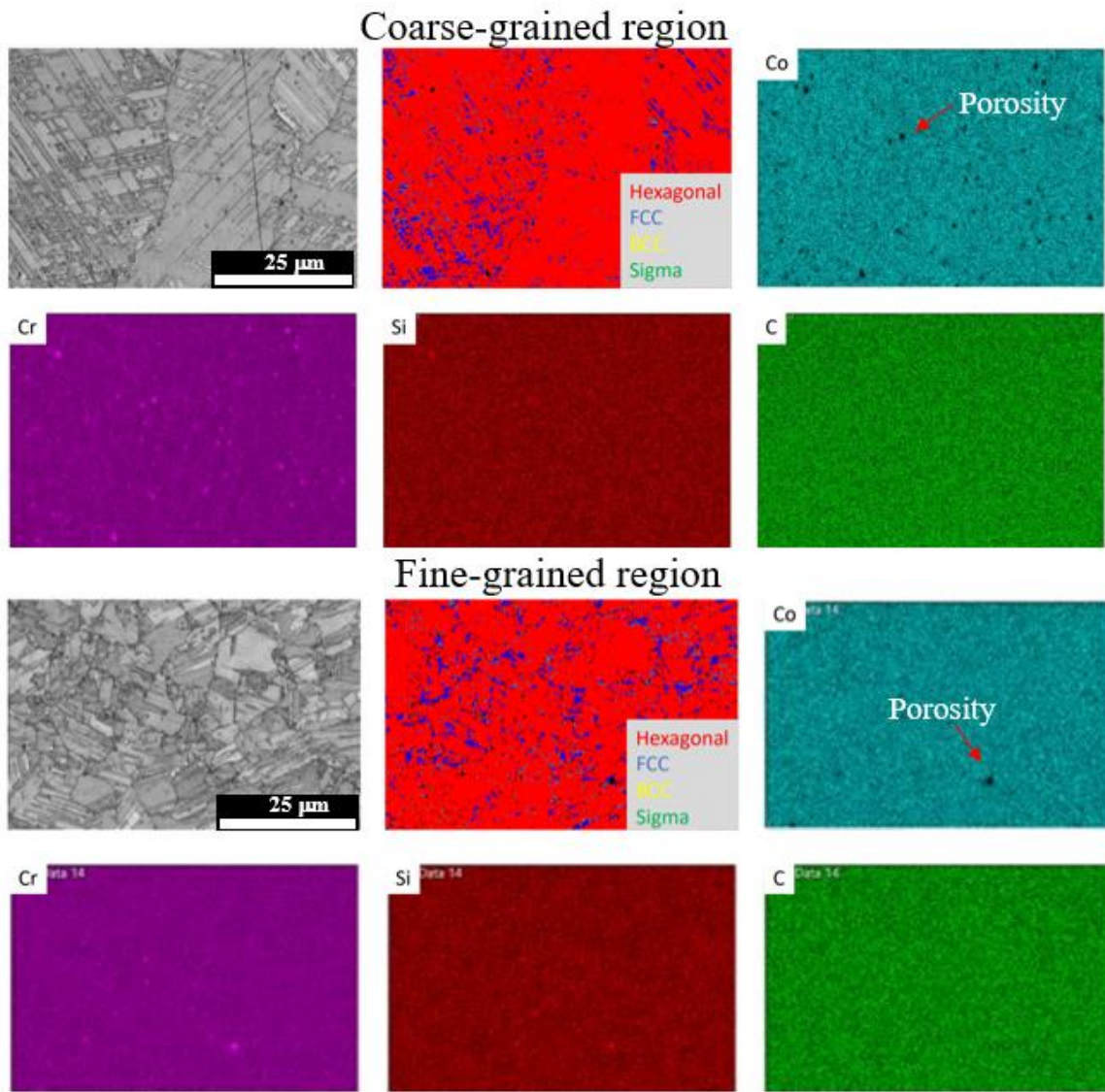
Figure 5.22 SEM micrographs, EBSD, and EDS maps of the coarse- and fine-grained regions for the CoCr+SiC sample. Porosity is highlighted in the Co EDS map.
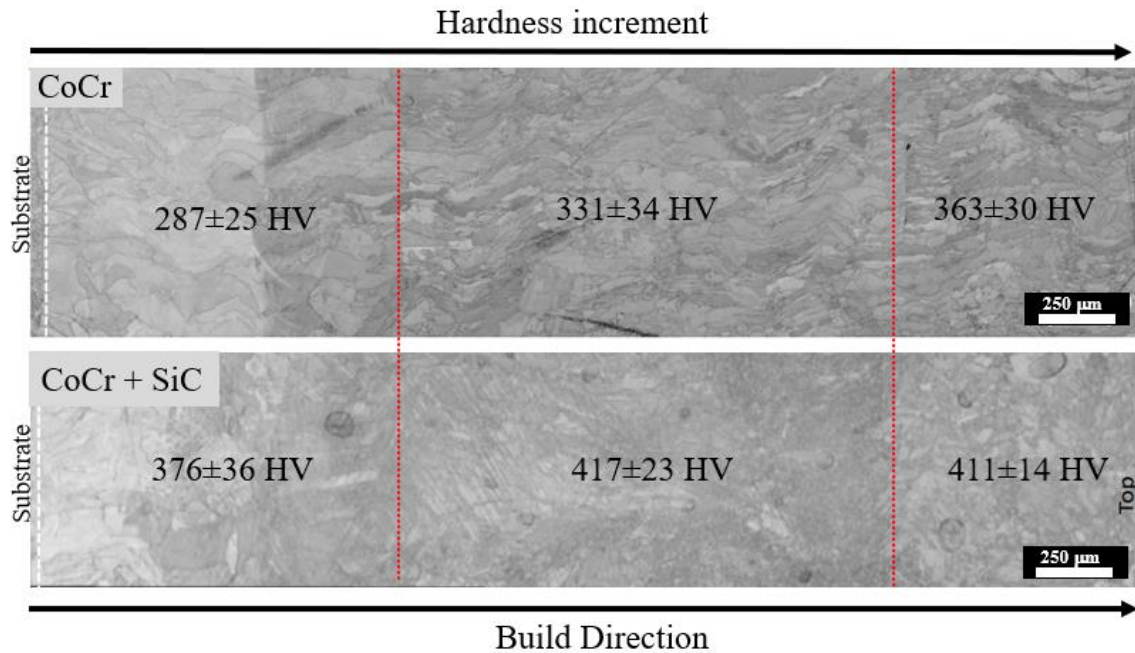
Figure 5.23 Hardness values along the build direction of CoCr and CoCr+SiC samples.

5.5 Conclusions

In this work, CoCr alloy was evaluated for SLM processes. Two different powder feedstocks were used. The first was commercial atomized CoCrW alloy obtained from Allegheny Technologies (ATI), and the second was CoCr+X (X=SiC and WC) milled powder. Both powder batches were melted by three different laser technologies, femtosecond pulsed laser, powder bed fusion, and direct energy deposition. The powder production was evaluated by the influence of the milling parameters and chemical composition. The printed samples were assessed by the capabilities of the laser set-up to print low-scale powder volume and by the changes in microstructure. The main conclusions that can be drawn are as follows:

1. High energy ball milling (SPEX) was the most successful process to synthesize powder with PSD with a range similar to the atomized virgin powder. The average grain size of the virgin and milled powder was 9 μm and 15 μm, respectively. A total time of ten hours was required to obtain these characteristics.

2. Adding stearic acid as the PCA for all three milling processes, SPEX, planetary and cryogenic milling, was ineffective in controlling PSA, particle morphology, and reducing agglomeration. Generally, the yield production in powder samples with PCA was reported as the lowest.

3. The synthesis of CoCr+WC powder was not successful due to the low yield rates, wide PSA, and high agglomeration could not be prevented. On the contrary, CoCr+SiC powder was successfully produced by SPEX with 1 wt.% of SiC NPs.

4. Two more concentrations of SiC NPs were evaluated, 2 and 4 wt.%. Particle agglomeration was no longer controlled with both concentrations regardless of the high production yields after sieving.

5. The DED system using a high-energy blue laser was the only one to melt the powders successfully. With the femtosecond laser and the PBF-LB systems, the energy density was insufficient. The main issues found in the fs-laser were related to the lack of an automated system that could handle low volumes of powder and spread uniform layer thickness.

6. The high power resulting from the blue laser's short wavelength (450 nm) significantly improved the melting process. Despite spreading the powder layers manually when using this laser system, high-density printed parts were obtained.

7. The addition of SiC NPs in the CoCr alloy resulted in a marked difference in the final microstructure of the printed parts. Smaller and more equiaxed grains were obtained. However, the grains sizes were not uniform along the sample. More equiaxed grains were observed closer to the edge of the sample due to variability in the chemical composition.

8. Hardness values were higher in the regions with more equiaxed grains. Sample CoCr+SiC showed less variability in measurements, indicating a microstructure more uniform than the CoCr sample.

9. Cr, Si, and Co segregation was observed at the top surface of the CoCr+SiC sample. This indicated that the Si is not uniformly distributed in the matrix. Optimization of the ball milling and laser process is necessary to guarantee a better distribution and wettability of these NPs.

10. Obtaining the ε-Co HCP in laser additive manufacturing is challenging. However, when using a blue laser, it is possible to obtain ε-Co HCP as the predominant phase. Repeating the laser scan one more time after the layer is melted likely favored the formation of this phase.

5.6   References

1. Bermingham, M., StJohn, D., Easton, M., Yuan, L., & Dargusch, M. (2020). Revealing the Mechanisms of Grain Nucleation and Formation During Additive Manufacturing. JOM, 72(3), 1065–1073. https://doi.org/10.1007/s11837-020-04019-5

2. Kok, Y., Tan, X. P., Wang, P., Nai, M. L. S., Loh, N. H., Liu, E., & Tor, S. B. (2018). Anisotropy and heterogeneity of microstructure and mechanical properties in metal additive manufacturing: A critical review. Materials & Design, 139, 565–586. doi:10.1016/j.matdes.2017.11.021

3. L. Thijs, K. Kempen, J.P. Kruth, J. Van Humbeeck, Fine-structured aluminum products with controllable texture by selective laser melting of pre-alloyed AlSi10Mg powder, Acta Mater. 61 (2013) 1809–1819, https://doi.org/10.1016/j. actamat.2012.11.052.

4. Tan, Q., Yin, Y., Prasad, A., Li, G., Zhu, Q., StJohn, D. H., & Zhang, M. X. (2022). Demonstrating the roles of solute and nucleant in grain refinement of additively manufactured aluminium alloys. Additive Manufacturing, 49, 102516. https://doi.org/10.1016/j.addma.2021.102516

5. Schimbäck, D., P. Mair, M. Bärtl, F. Palm, G. Leichtfried, S. Mayer, P. J. Uggowitzer, and S. Pogatscher. (2022). "Alloy Design Strategy for Microstructural-Tailored Scandium-Modified Aluminium Alloys for Additive Manufacturing." Scripta Materialia 207: 114277. doi:10.1016/j.scriptamat.2021. 114277.

6. Martin, J. H., Yahata, B. D., Hundley, J. M., Mayer, J. A., Schaedler, T. A., & Pollock, T. M. (2017). 3D printing of high-strength aluminium alloys. Nature, 549(7672), 365–369. https://doi.org/10.1038/nature23894

7. Zhang, Duyao; Qiu, Dong; Gibson, Mark A.; Zheng, Yufeng; Fraser, Hamish L.; StJohn, David H.; Easton, Mark A. (2019). Additive manufacturing of ultrafine-grained high-strength titanium alloys. Nature, 576(7785), 91–95. doi:10.1038/s41586-019-1783-1

8. Bermingham, M.J., StJohn, D.H., Krynen, J., Tedman-Jones, S., Dargusch, M.S. (2019) Promoting the columnar to equiaxed transition and grain refinement of titanium alloys during additive manufacturing, Acta Mater. 168, 261–274, https:// doi.org/10.1016/j.actamat.2019.02.020.

9. Li, Bo; Qian, Bo; Xu, Yi; Liu, Zhiyuan; Zhang, Jianrui; Xuan, Fuzhen (2019). Additive manufacturing of ultrafine-grained austenitic stainless steel matrix composite via vanadium carbide reinforcement addition and selective laser melting: Formation mechanism and strengthening effect. Materials Science and Engineering: A, 745(), 495–508. doi:10.1016/j.msea.2019.01.008

10. Doñate-Buendia, C., Kürnsteiner, P., Stern, F., Wilms, M.B., Streubel, R., et al. (2021). Microstructure formation and mechanical properties of ODS steels built by laser additive manufacturing of nanoparticle coated iron-chromium powders, Acta Mater. 206, https:// doi.org/10.1016/j.actamat.2020.116566 116566.

11. Streubel, R., Wilms, M.B., Doñate-Buendía, C., Weisheit, A., Barcikowski, S., Schleifenbaum, J.H., Gökce, B. Johann, et al. (2018). Depositing laser-generated nanoparticles on powders for additive manufacturing of oxide dispersed strengthened alloy parts via laser metal deposition, Jpn. J. Appl. Phys. 57 (4), https://doi.org/10.7567/ JJAP.57.040310.

12. Han, Q., Setchi, R., Evans, S.L.. (2016). Synthesis and characterization of advanced ball-milled Al-Al2O3 nanocomposites for selective laser melting, Powder Technol. 297, 183–192, https://doi.org/10.1016/j.powtec.2016.04.015.

13. Gu, D., Wang, H., Chang, F., Dai, D., Yuan, P., (2014). Selective laser melting additive manufacturing of TiC / AlSi10Mg bulk-form nanocomposites with tailored microstructures and properties 56, 108–116.

14. Zhai, W., Zhu, Z., Zhou, W., Mui, S., Wei, J. (2020). Selective laser melting of dispersed TiC particles strengthened 316L stainless steel. Composites Part B: Engineering, 108291. doi:10.1016/j.compositesb.2020.108291

15. Kajima, Y., Takaichi, A., Nakamoto, T., Kimura, T., Yogo, Y., Ashida, M., Doi, H., Nomura, N., Takahashi, H., Hanawa, T., Wakabayashi, N. (2016) Fatigue strength of Co-Cr-Mo alloy clasps prepared by selective laser melting. J Mech Behav Biomed Mater 59:446–458. https://doi.org/10.1016/j.jmbbm.2016.02.032

16. da Silva Costa, A.M., Oliveira, J.P., Munhoz, A.L.J. et al. (2021). Co–Cr–Mo alloy fabricated by laser powder bed fusion process: grain structure, defect formation, and mechanical properties. Int J Adv Manuf Technol 116, 2387–2399. https://doi.org/10.1007/s00170-021-07570-w

17. Wang, S.; Zhan, S.; Hou, X.; Wang, L.; Zhang, H.; Zhang, H.; Sun, Y.; Huang, L. (2022). Microstructure and Mechanical Property of a Multi-Scale Carbide Reinforced Co–Cr–W Matrix Composites. Crystals, 12, 198. https://doi.org/10.3390/cryst12020198

18. Jacob, G., Brown, C.U., Donmez, A., et al. (2018). The Influence of Spreading Metal Powders with Different Particle Size Distributions on the Powder Bed Density in Laser-Based Powder Bed Fusion Processes. NIST Adv. Manuf. Ser. 100–17. https://doi.org/10.6028/NIST.AMS.100-172

19. Zhu, H.H., Fuh, J.Y.H., Lu, L., et al. (2007). The influence of powder apparent density on the density in direct laser-sintered metallic parts. Int. J. Mach. Tools Manuf. 47, 294–298. https://doi.org/10.1016/j.ijmachtools.2006.03.019

20. Q. Han, R. Setchi, S.L. Evans, (2017) Characterisation and milling time optimisation of nanocrystalline aluminium powder for selective laser melting, Int J Adv Manuf Technol 88 (5-8) 1429–1438

21. Sawangrat, C., Yamaguchi, O., Kumar, S., Ameyama, K. (2014). Application of Harmonic Structure Design to Biomedical Co–Cr–Mo Alloy for Improved Mechanical Properties. Materials Transactions, 55, 99-105

22. Louidi, S., Bentayeb, F. Z., Tebib, W., Suñol, J. J., Escoda, L., & Mercier, A. M. (2012). Stacking faults and phase transformations study in ball milled Co 100-xCrx (x = 0, 20, 50) alloys. Materials Chemistry and Physics, 132(2–3), 761–765. https://doi.org/10.1016/j.matchemphys.2011.12.008

23. Moumeni, H., Nemamcha, A., Alleg, S., Greneche, J.M. (2010). Stacking faults and structure, analysis of ball milled Fe–50%Co powders. Materials Chemistry and Physics, 122, 439-

24. Hossein, M. (2017). Nanocrystallization of Al Powder by Cryomilling Process. KONA Powder and Particle Journal, 34, 207-212

25. Chen, D., Ghen G., Ni, S., Cen, G., Yan, H., Chen, Z. (2008). Phase formation regularities of ultrafine TiAl, NiAl, and FeAl intermetallic compound powders during solid–liquid reaction milling. Journal of Alloys and Compounds, 457, 292–5

26. Kang, Y-C., Chan, SL-I. (2008). Tensile properties of nanometric Al2O3 particulate-reinforced aluminum matrix composites. Materials Chemistry and Physics, 85:438–43. 98

27. Tjong, SC. (2007). Novel nanoparticle-reinforced metal matrix composites with enhanced mechanical properties. Advance Engineering Materials, 9:639–52

28. Ullsperger, T., Liu, D., Yurekli, B., Matthaus, G., Schade, L., Seyfarth, B., Kohl, H. (2021). Ultra-short pulsed laser powder bed fusion of Al-Si alloys: Impact of pulse duration and energy in comparison to continuous-wave excitation. Additive Manufacturing, 46, 102085

29. Li, K., Mao, X., Khanlari, K., Song, K., Shi, Q., & Liu, X. (2020). Effects of powder size distribution on the microstructural and mechanical properties of a Co–Cr–W–Si alloy fabricated by selective laser melting. Journal of Alloys and Compounds, 825, 153973.

30. Wang, Z., Tang, S. Y., Scudino, S., Ivanov, Y. P., Qu, R. T., Wang, D., Yang, C., Zhang, W. W., Greer, A. L., Eckert, J., & Prashanth, K. G. (2021). Additive manufacturing of a martensitic Co–Cr–Mo alloy: Towards circumventing the strength–ductility trade-off. Additive Manufacturing, 37(November 2020), 1–14. https://doi.org/10.1016/j.addma.2020.101725

31. Takaichi, A., Suyalatu, T., Nakamoto, N., Joko, N., Nomura, Y., Tsutsumi, S., Migita, H., Doi, S., et al. (2013). Microstructures and mechanical properties of Co-29Cr-6Mo alloy fabricated by selective laser melting process for dental applications, Journal of the Mechanical Behavior of Biomedical Materials, 21,67–76. https://doi.org/10.1016/j.jmbbm.2013.01.021

32. Hedberg, Y.S., Qian, Z., Shen, S., Virtanen, I. (2014) In vitro biocompatibility of CoCrMo dental alloys fabricated by selective laser melting. Dental Materials, 30, 525–534. https://doi.org/10.1016/j.dental.2014.02.008

33. Xiao, L., Wang, H., Kaufmann, K., Vecchio, K. (2023). Directed energy deposition of pure copper using blue laser. Journal of Manufacturing Processes, 85, 314-322. https://doi.org/10.1016/j.jmapro.2022.11.064

34. Watanabe, T. (2023). Electrodeposited alloy. Nano-Plating (III), 217-603. https://doi.org/10.1016/B978-0-323-99894-9.00010-0.

35. Li, K., Wang, Z., Song, K., Khanlari, K., Yang, X.-S., Shi, Q., Liu, X., & Mao, X. (2022). Additive manufacturing of a Co-Cr-W alloy by selective laser melting: In-situ oxidation, precipitation and the corresponding strengthening effects. Journal of Materials Science & Technology, 125, 171–181. https://doi.org/10.1016/j.jmst.2022.01.036

36. Review, K. S., Konieczny, B., Szczesio-wlodarczyk, A., & Sokolowski, J. (2020). Challenges of Co – Cr Alloy Additive Manufacturing Methods in Dentistry — The Current State of. Materials, 13(16), 3524.

37. Kuai, Z., Li, Z., Bai, P., Nie, Y., Liu, W., Yang, S., & Qi, K. (2020). Microstructures and Mechanical Properties of CoCrW Alloy Fabricated by Simulating Multi-Beam Selective Laser Melting. Advanced Engineering Materials, 1901356. doi:10.1002/adem.201901356.

CHAPTER 6

ELUCIDATING THE EFFECT OF POWDER REUSABILITY OF 316L STAINLESS
STEEL ON THE AS-PRINTED PARTS FOR LASER
POWDER BED FUSION

6.1   Abstract

With each use in the additive manufacturing process, the powder feedstock undergoes various forms of degradation. Thermal cycling, exposure to high temperatures, and interaction with oxygen can lead to changes in powder morphology, particle size distribution, and chemical composition. If such defects are present in the powder, they can potentially transfer to the as-printed part during the melting and solidification process. In the case of powder reusability for 316L stainless steel, when implementing effective powder handling and storage practices, small variability in the as-printed components has been reported within 10 to 30 reuses. However, in this study, it was observed that the as-printed parts experienced strengthening after 20 reuses, equal to 1000 hours of total printing time. From zero reuses to 20 reuses, the UTS increases from 667 to 709 MPa, and the yield strength from 554 to 618 MPa. This was also accompanied by a slight decrease in uniform elongation from 22 % to 17 %. To date, this behavior has not been reported for reusability studies on 316L stainless steel. Therefore, an extensive analysis of the evolution of the powder feedstock and printed parts to explain the relationships between reuses with improvement in yield strength was performed. Additionally, individual strengthening mechanisms were calculated to determine the primary contributors. The contribution of dislocation and grain boundary strengthening was found to be significant due to the differences in dislocation density, changes in grain boundary misorientations, and the formation of quasi-equiaxed grains.

6.2   Introduction

The evolution of powder properties in 316L stainless steel (SS) alloys in Laser Powder Bed Fusion (PBF-LB) has been reported in several powder reusability studies [1-5]. Following a suitable initial composition specification and sieving during reuse, powder feedstock exhibits minor size distribution and bulk composition changes. However, significant changes to particle morphology, magnetic properties, and surface oxidation have been reported. With many properties changing after each powder reuse, identifying which specific property affects the component quality is extremely difficult [1,2]. Isolating individual variables to generate comprehensive knowledge may be feasible for laboratory scale experiments using custom made PBF-LB equipment [6]. However, at an industrial manufacturing level, other approaches should be considered.

Differences in the process parameters, atmosphere, geometries printed, and reuse methodologies cause the powder to degrade at different rates. Therefore, predicting powder changes, defects, and standardizing reusability guidelines remain fields for further development. Thanks to systematic studies assessing various properties of powder feedstock, it is possible to estimate defect transferability from the powder feedstock to the finished part. The highest impact has been reported in areas such as 1) disruption of powder spreadability caused by powder agglomeration, changes in size, and morphology [7-11] and 2) increment in impurities, contaminants, and loss of alloy elements. The first case is reported to affect surface roughness [12], powder bed packing density [13], balling [14], and porosity [15-16]. In the second case, the melt pool experiences instabilities due to decreased wettability and disruptions in the surface tension and Maragoni flow [17-19]. As a consequence, various defects are presented, such as porosity [20-21], increment in spatter ejection [22], balling [23], microstructural changes [24], grain boundary segregation [25], and formation of oxide inclusions [21]. The discussion section will provide additional correlations of possible less-reported consequences due to powder changes.

To assess the impacts of powder reuse on mechanical performance, more long-term reuse studies are still required, along with the performance of various tests, predominantly tensile and fatigue [26]. For 316L alloys, no significant changes have been reported in the microstructure and tensile properties of the as-printed parts after 12 [5], 15 [1], and 30 [2] reuses. However, Liu et al. [27] demonstrated that for samples reused five times, their UTS, yield strength, and elongation decreased by 25 %, 11 %, and 53 %, respectively. This discrepancy may arise from the lack of sieving after each reuse. In this study, despite the powder changes being consistent with the trends already reported in the literature, it is observed that the yield strength increased by 12 %, and the uniform elongation decreased by 17 % after 20 reuses.

Modifications in composition, solution strengthening, grain refinement, and grain boundary strengthening have been reported as mechanisms for enhancing the mechanical properties of ferrous alloys in AM. Among these mechanisms, it has recently been reported that the intrinsic cellular dislocation structures markedly contribute to the strength of additive manufactured (AM) 316L SS [28-31]. Additionally, due to the complex microstructural transitions in PBF-LB processes, these strengthening sources' origin, evolution, and effects still need to be determined. However, progress has been made in quantitative methodologies focused mainly on the effects of solidification cell structure, high-angle grain boundary (HAGBs), low-angle grain boundary (LAGBs), and dislocation strengthening [29,32,33] on mechanical behavior.

Due to the low variability in microstructure and tensile properties reported for AM 316L samples, strengthening mechanisms have not been considered for powder reusability. Therefore, in this study, individual strengthening mechanisms were quantified to understand better powder reusability's impact on

mechanical behavior. Additionally, the evolution of the powder feedstock and as-printed parts is reported and correlated to changes observed in the microstructure of the as-printed parts.

6.3   Methodology

6.3.1   Powder feedstock and reuse method

AISI 316L gas atomized powder (3D Systems) was reused in four different powder batches. All powder batches started from the virgin condition and were reused following the methodology specified in Figure 6.1. The residual powder from the supply chamber, overflow tank, and build area was collected to collect as much degraded powder as possible. Following this, the powder was blended, sieved, and reused. An automated sieving unit with a 200 mesh size and an argon atmosphere keeping an oxygen content below ~4% was used.
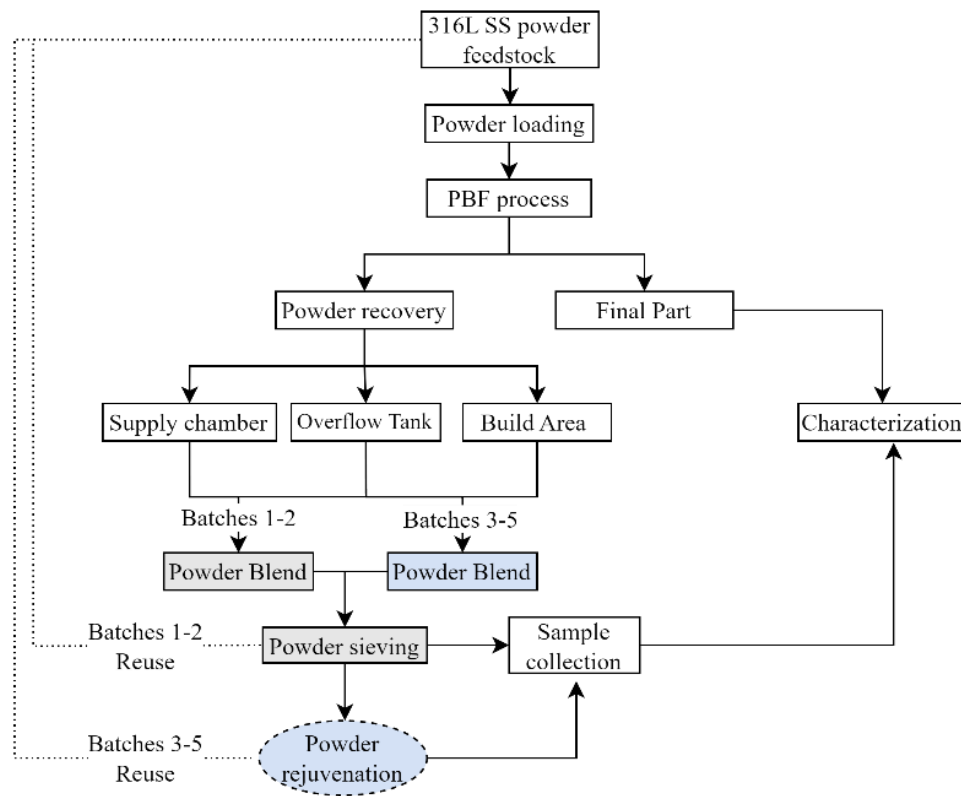
Figure 6.1 Powder reuse method implemented.

Table 6.1 shows the specifications of each batch and printing conditions. For *batch 1*, only virgin powder was used to print only one build. *Batch 2* was reused five times, and no virgin powder was added after the completion of each build (powder rejuvenation). *Batch 3* was reused 20 times, and powder

103

rejuvenation was implemented after each build to reach this number of reuses. This powder feedstock was in service for six months. Similarly, *batch 4* was reused 20 times, and powder rejuvenation was employed as well. However, this powder was in service for a total of 12 months. Due to the long time required to obtain sufficiently degraded powder for 316L SS alloys, *batch 5* was created to accelerate the powder degradation intentionally. This batch was a mix of powder from batch 4 (20 reuses) with 10% of sieved spatter particles collected throughout ten consecutive builds. Batch 4 is not correlated to a specific number of reuses or printing time due to the complexity of connecting the powder properties to a particular aging time.

Once each powder batch reached the number of reuses specified, 0, 5, and 20, nine horizontal rectangular blocks (10x20x70 mm^3) and six cubic blocks (10x10x10 mm^3) were printed under the same conditions (Figure 6.2 b). The goal of printing this extra build was to obtain the exact part geometry to compare changes in microstructure, chemistry, and mechanical performance due to different powder aging rates.

Table 6.1 316L SS powder feedstock classification and printing conditions for batches 1-4.

Sample ID	Powder batch name	Number of reuses	Printing time (hours)	Time in service (months)	Batch size (kg)	Specifications
0R	Batch 1	0	8	0	35	Printed from virgin powder (VP)
5R	Batch 2	5	48	3	35	No powder rejuvenation
20R-3	Batch 3	20	710	6	~100	Powder rejuvenation
20R-4	Batch 4	20	1010	12	~100	Powder rejuvenation
20R+S	Batch 5	20	1018	12	15	80% reused powder + 10% spatter
S	Spatter	-	-	4	3	Powder collected from the chamber hood
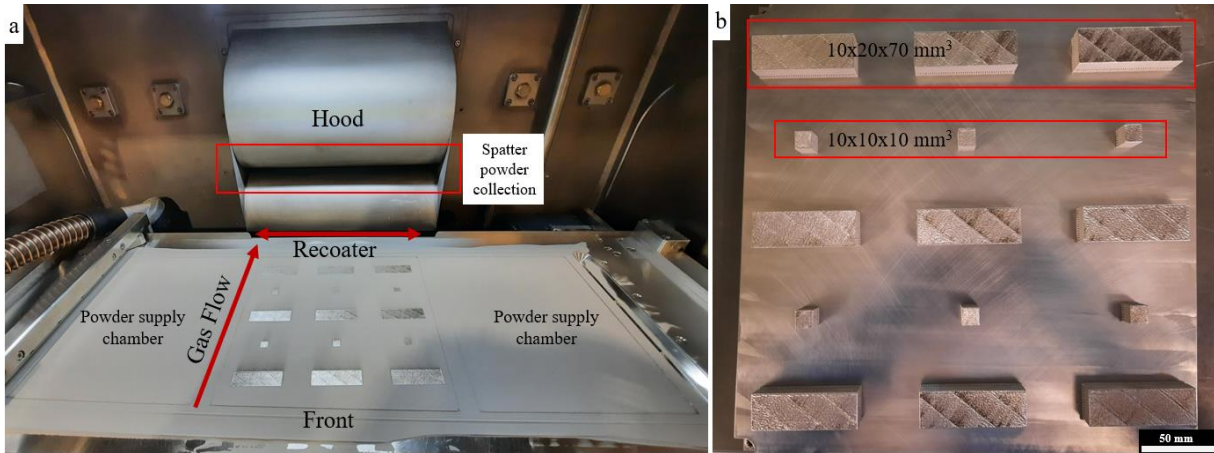
Figure 6.2 a) View of the inside of the laser powder bed fusion machine. This system allows recoating in both directions (right-left). Spatter powder was collected in the aperture from the hood indicated within the red rectangle. b) Distribution of the geometries of the printed parts in the build plate.

6.3.2 PBF-LB process

A ProX DMP 350 PBF-LB machine from 3D Systems with a power of 300 W, speed of 900 mm/s, and hatch spacing of 100 μm was used to produce batches 1-5. The chamber was pressurized to a positive pressure of 150 MPa to ensure a low oxidation risk, and the oxygen level was kept below 10 ppm. An Argon atmosphere was circulated from the front to the back into the chamber (Figure 6.2 a). The laser parameters, powder storage, and sieving were consistent throughout all the builds to minimize variability.

6.3.3 Sample preparation

A small amount of powder was embedded in conductive Bakelite powder to analyze its cross sections. The powder was ground using 1200-grit SiC paper for 20 seconds and then polished with 0.02 mm colloidal silica for 24 hours. The printed parts were cut in the build and transverse direction, mounted in Bakelite, and ground with SiC paper from 320 to 1200-grit. The polishing steps were carried out using 1 μm and 3 μm diamond suspension and then up to 0.02 μm colloidal silica for 24 hours. The TEM samples from the printed parts were prepared using a focused ion beam (FIB) after the polishing steps described above. Before FIB cross-sectioning, a protective layer of Pt was deposited to prevent Gallium implantation and prevent surface erosion.

6.3.4 Characterization

Morphological characterization was carried out employing scanning electron microscopy (Helios NanoLab 600i SEM/FIB DualBeam™). Particle size distribution (PSD) was obtained using a Microtrac S3500 laser diffraction analyzer according to ASTM B822-20 [34]. The measurement of powder

flowability was conducted using the Carney flowmeter funnel. A Panalytical Empyrean X-ray diffractometer generated data for powder and solid parts with the following settings: an angular range of 40–110° using a step size of 0.02°, with a Cu Kα radiation source under 40 kV voltage and 40 mA current. Silica standards were used as a baseline for strain and dislocation calculations.

The chemical characterization for each powder and the solid bulk samples was performed using X-ray energy spectra using energy dispersive spectroscopy (EDS). Additionally, combustion, inert gas fusion (IGF), and atomic emission spectroscopy (AES) tests were executed according to ASTM E1019-18 [35] and ASTM E1086-14 [36], respectively.

The as-printed microstructure was characterized by electron backscatter diffraction (EBSD, Helios NanoLab 600i SEM/FIB DualBeam) and transmission electron microscopy (TEM, Talos L120C). EBSD and TEM characterizations were carried out at the center of the cross-section. Five EBSD maps with areas of the size 919x174 mm^2 were characterized to obtain a good statistical determination of the microstructures. EBSD maps were obtained using a step size of 0.8 mm. Grain boundaries were classified based on their misorientations of ≥2° and <15° for LAGBs and ≥15° for HAGBs. The grain sizes and misorientation fractions were determined using the MATLAB toolbox MTEX. All fractions computed in this work are length fractions.

6.3.5   Mechanical Testing

Ten tensile samples were cut from the 10x20x70 mm^3 blocks. The dimensions of the tensile coupons were consistent with the subsize specifications from ASTM E8 [37]. An MTS 6 Landmark 22.5 kip tensile tester was used, applying the load perpendicular to the build direction. For all tests, the displacement rate was 0.16 mm/s, resulting in an initial strain rate of ~10^{-3} 1/s. Displacement was recorded using a 25 mm extensometer. Microindentation measurements were obtained using LECO's AMH55 automated hardness equipment. The average values resulted from 300 indents distributed along three locations, 100 at the bottom, 100 at the center, and 100 at the top of each sample.

6.4   Results and discussion

6.4.1   Powder feedstock changes due to reusability

During reuse, powders are expected to change in size, morphology, composition, and microstructure, which ultimately affects the properties of the printed parts. This is due to the collisions of the ejected metal droplets with the cold, raw particles around the melt pool. This further leads to agglomeration, breakage, and remelting of the particles. Figure 6.3 compares changes in size and morphology for batches 1-4. Due to the complexity of the PBF-LB process, isolating specific powder changes to monitor their

effect on defect formation is exceptionally challenging. Therefore, the level at which each change impacts the final quality of the printed part remains to be determined. However, important correlations between their effect on the microstructure and mechanical performance can be obtained by keeping track of the powder evolution as the number of reuses increases.

From Figure 6.3c-f, it can be observed that after a high number of reuses, the changes in morphology were more significant compared to lower number of reuses. This study confirmed that the aspect ratio of the highly reused sample (20R-4) decreased by 7 %, indicating that its morphology had a negligible change. Particles with substantial morphological changes can also be correlated to internal porosity. Figure 6.3f shows that only irregular particles showed porosity, while the spherical particles (virgin powder or spatter) remained unchanged.

Regarding particle size distributions, several researchers have reported that the reused powder is slightly coarser after reuse [38-41]. When comparing our samples, it was observed that there was an increase in size distribution which shifted toward large particle diameters only for powder from 0R, 5R, and spatter (Figure 6.4). It is likely that during the first number of reuses, the powder experienced the formation of agglomerates that passed through the mesh, leading to an increase of D_{50} and D_{90}. On the other hand, powder reused for extended periods can either experience particle breaking due to remelting cycles or the formation of more oversized agglomerates causing particles to be stopped during the sieving process. The number of finer particles in all powder batches remained relatively constant, which can be beneficial as the bed density may not meaningfully change through multiple reuses. In the case of the spatter powder, there is an evident increase in PSD, showing a D_{90} above 100 μm. Broader size distributions are expected for spatter powder due to the different forming processes and aggregation with the subjacent particles from the powder bed [27].
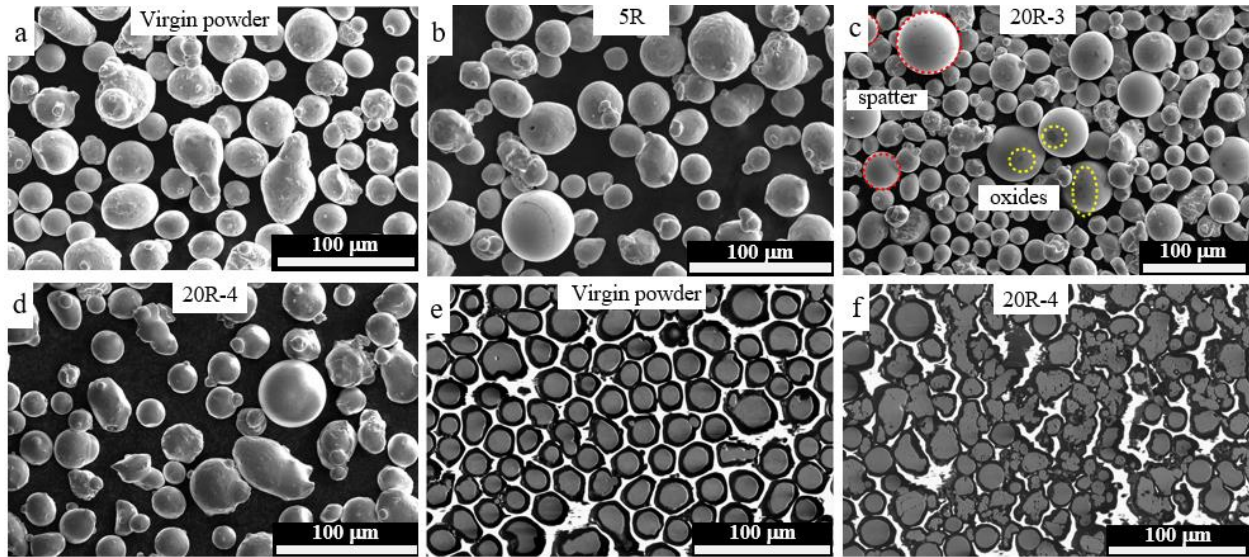
Figure 6.3 SEM images of powder evolution from the virgin condition to reused after 5 and 20 reuses. a) Atomized virgin powder with spherical and irregular morphologies. b-d) Reused powder after a low and high number of reuses. Spatter particles are enclosed in red and surface oxides in yellow. e-f) Powder cross-sections indicating an increase in internal porosity after 20 reuses.
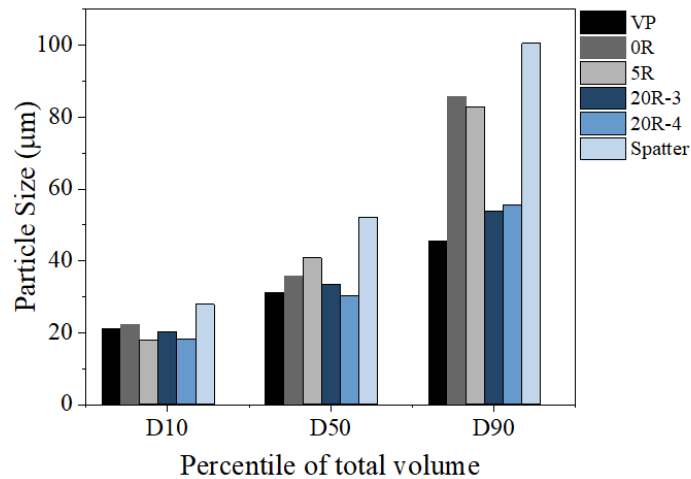
Figure 6.4 Particle size distribution of each powder condition after sieving.

The heat-affected powder can be classified into two groups. Group 1 corresponds to the particles lying near the vicinity of the melt pool but not in direct contact with the laser beam, and group 2 is the particles directly in contact with the laser beam. Particles in group 1 experience changes in shape due to the sintering or fusion of overheated material leading to microstructural and chemical changes as well. The particles directly in contact with the laser beam are classified as spatter. Spatter can be further categorized as 1) material ejected directly from the melt pool due to recoil pressure [42], 2) entrained particles by the

vapor jet, and 3) metal vapor ejection (condensate). The first two spatter formation mechanisms led to spatter Type I, II, and III, represented in Figure 6.5.

For spatter Type-I, the particles exhibit smooth spherical morphologies as they experience rapid cooling while getting away from the laser radiation and encountering gas flow developing an excellent spherical shape. Type-II spatter is characterized by ejected molten material at lower distances from the melt pool split into small droplets. This molten material adheres to the surface of splashed particles and the powder bed, contributing to forming more irregular shapes. Lastly, Type-III spatter is expelled at even shorter splashing distances under the effects of vaporizing and shock waves caused by the interaction of the laser beam and the melt pool [43]. Powder with coarse, irregular shapes and a large amount of unmelted material on the surface is characterized as Type-III. The effect of the spatter is investigated by evaluating changes in laser power and scan speed [25, 44,45]. However, for powder reuse purposes, there is currently a lack of information about the behavior of existent spatter particles interacting with virgin and non-virgin powder and how this can affect the quality of the parts.
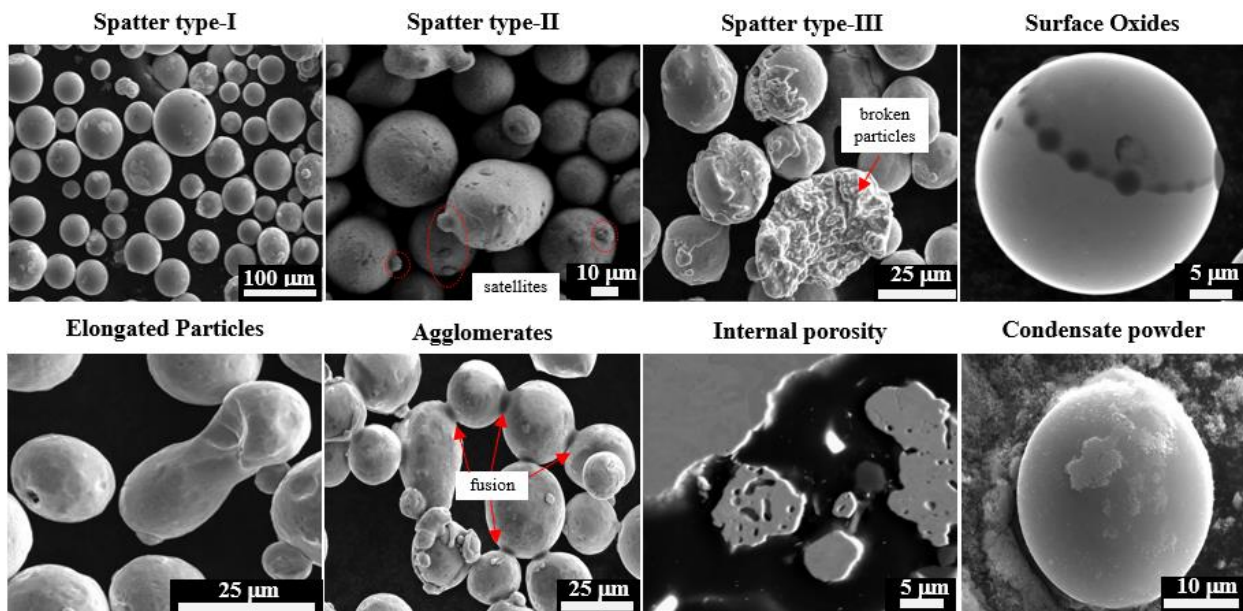
Figure 6.5 Summary of the most common changes observed in the heat-affected powder and spatter classification.

To further evaluate the impact of the changes observed in the powder size distributions and morphology, a visual inspection of the powder bed was performed to detect surface-visible anomalies in the powder bed. Any non-conformity was observed from zero to 20 reuses. However, when mixing the sieved reused powder (20R-4) with 20 % spatter, recoater hopping and streaking were detected. Due to

the impact of inhomogeneous powder spreadability on the densification of the printed components, it was decided to add only 10% of the spatter. A further comprehensive understanding of the effect of spatter is required in the powder reusability field. Therefore, intrinsic correlations between this by-product and the part quality could be established by analyzing and quantifying the spatter. Santecchia et al. [47] reported an overview of how excessive powder contaminants such as spatter and condensate can alter the properties of the reused powder.

Flow rate is another essential characteristic that is linked with spreadability. Figure 6.6 shows no specific trend with a low number of reuses. For a few reuses, powder samples after 1,2,3,4, and 5 were additionally analyzed. Highly reused powder flowed at a slightly faster rate. This is likely due to the irregular powder having lower free surface energy which decreases the interparticle adhesion, thereby reducing friction.
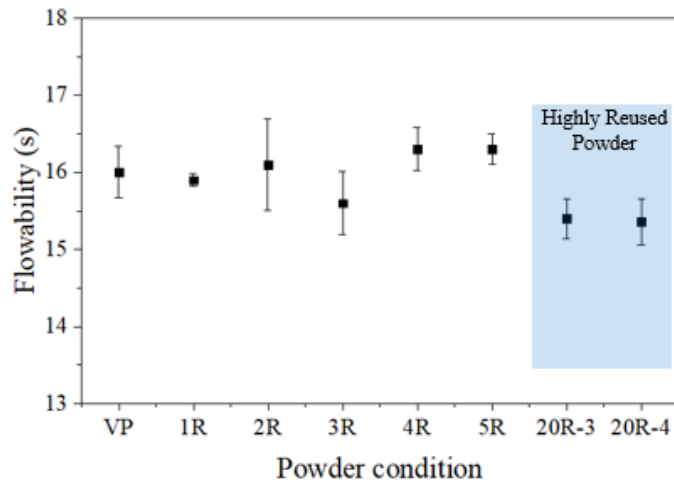
Figure 6.6 Hall flow test results for virgin and sieved powder after different reused cycles.

Surface oxidation is a by-product that was detected from the first reuse, and which commonly presents as circular dark spots. There is sufficient evidence indicating that the heat-affected particles, especially droplet spattering, present a higher volume of such surface oxides. Sources of oxide formation in PBF-LB processes are associated with the existing oxygen inside the chamber, the sieving process, and the entrapped porosity in the powder particles after reuse cycles and atomization processes. Figure 6.7 shows an example of silicon-rich oxide on the surface of a spatter particle. Si and Mn, with higher oxidation potential than Cr and Fe, can selectively oxidize on the powder surface when the powders are subjected to heat treatments [24]. The rate at which they form after each reuse is unknown, however, this can be correlated with the increase in oxygen content in the bulk composition of the reused powder.

Rory et al. [47] reported a summary of the most recent papers on the powder reusability of 316L, where a significant increase in oxygen content was observed after 15 reuses. In the present study, such a trend was not observed after 20 reuses, and the oxygen content increased by less than 5 % (Table 6.2 on page 112). The spatter powder showed an increase of 51% (721 ppm) from the virgin condition. This indicates that the volume of spatter powder present in the highly reused powder was not significant in modifying the oxygen content in the powder bulk composition. This can further lead to a localized oxygen variation in the powder bed, increasing the probability of defect formation or premature failures in the printed components [48]. Passive oxide films are expected in stainless steel powder. However, oxide layers in the range of 10 μm to 100 μm can lead to melt pool instabilities as these films cannot be entirely vaporized by the stirring action of the beam and Marangoni flow [22]. Surface oxides of this kind may lead to entrapped oxide inclusions affecting the melt pool's surface tension effects and flow, causing lower surface wetting conditions [18, 24]. Consequently, a decrease in layer adherence and densification can occur, causing lower mechanical properties of the built components.
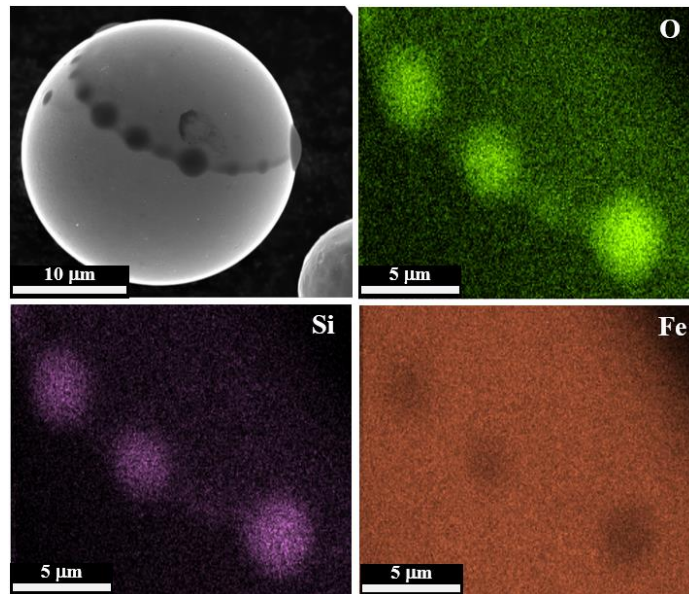
Figure 6.7 Surface oxide on spatter particle with its EDS map showing Si-rich oxides.

Table 6.2 Chemical composition of the various powder conditions and as-printed parts using powder with zero and 20 reuses.

	Element (wt.%)													
	Cr %	Cu %	Si %	Mn %	Mo %	Ni %	P %	S %	C %	O %	N %	H%	Fe %	Cr_{eq}/Ni_{eq}
Standard F3184 – 16 [49]	16-18	-	≤1	≤2	≤3	10-14	≤0.045	≤0.03	≤0.03	-	-	-	Bal	-
Supplier	-	≤0.5	-	-	-	-	-	-	-	≤0.1	≤0.11	-	-	-
Virgin powder	18.09	0.09	0.5	1.15	2.32	12.24	0.014	0.009	0.016	0.048	0.068	0.0004	Bal	1.35
20R-4 powder	18.2	0.06	0.45	1.06	2.37	12.4	0.014	0.006	0.02	0.049	0.086	0.0005	Bal	1.3
Spatter powder	-	-	-	-	-	-	-	-	-	0.072	-	-	-	-
0R - bulk solid	17.67	0.03	0.56	1.32	2.4	12.99	0.012	0.008	0.014	0.041	0.065	0.0002	Bal	1.31
20R-4 - bulk solid	17.75	0.04	0.58	1.19	2.42	12.95	0.013	0.008	0.022	0.042	0.08	0.0002	Bal	1.27

Other chemical composition changes presented were the increase in nitrogen and carbon content by 26 % and 25 % after 20 reuses, respectively (Table 6.2 on page 112). Both elements can be picked up through diffusion at the melt pool, powder, and solidified surface. The presence of carbon-based by-products (soot) from reuse also contributes to the increase of carbon content. The presence of both elements may favor the formation of carbides and nitride precipitates or segregation in combination with active metals like chromium, molybdenum, etc. However, the XRD diffractograms (Figure 6.8) showed that all powder batches corresponded to single-phase, thus indicating that they are completely dissolved in the metallic matrix as interstitial elements or cannot be detected.
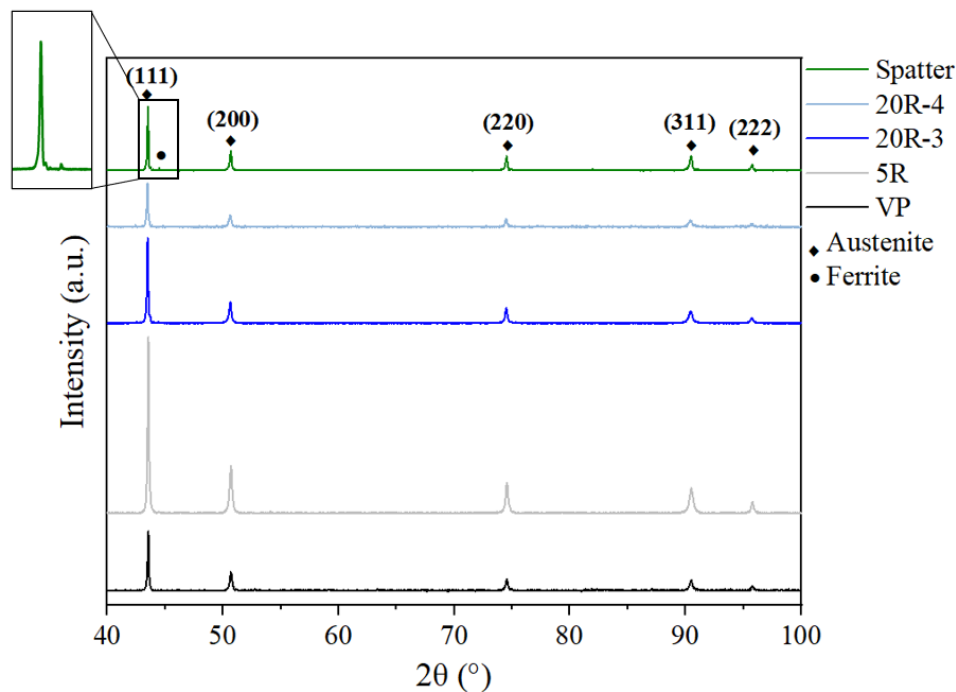
Figure 6.8 XRD of virgin powder and reused 316L stainless steel powder. Ferrite peak was detected only in spatter powder.

With a homogeneous microstructure, absence of inclusions, and high nitrogen content, positive contributions to corrosion resistance and strengthening can be obtained in stainless steel alloys [50]. Therefore, the addition of nitrogen in 316L for PBF-LB has been studied by printing materials under various concentrations and flows of nitrogen-protective atmospheres [51,52] or by increasing the nitrogen content directly into the steel powder [53,54]. Such investigations reported that only the roughness and flowability of the powder feedstock with higher nitrogen levels (>800 ppm) are slightly affected. It should be considered that powder degradation has been reported to be faster when the PBF-LB process is

performed under a nitrogen atmosphere. Pauzon et al. [51] reported that the 316 L powder degradation in argon was negligible after three reuses. Under a nitrogen atmosphere, the powder experienced more critical oxidation covering a significant area of the powder surface, thus causing a lower Charpy impact value.

Molten ejecta droplets in PBF-LB experience extreme cooling rates ($>10^5$ K/s) [55], leading to sufficiently large undercooling to facilitate the formation of solid-state transformations. This can lead to an increase of δ-ferrite in reused powder [1,2,43]. As indicated by XRD analysis results shown in Figure 6.8. spatter powder showed a minor increase in ferrite content. It can also be observed that after 20 reuses, the phase fraction did not differ from the virgin condition.

Ferrite presence is not exclusive to powder reusability; it has also been found in virgin atomized powder [56,57]. Kurzynowski et al. [56] confirmed the presence of ferrite in the powder and the as-fabricated parts. Ferrite was located in intercellular regions, columnar grain boundaries, and solute banding lines in quantities below the XRD identification threshold. Furthermore, even if ferrite is not present in the virgin powder, the chemical composition of the powder indicates that the ferrite-austenite (FA) solidification mode should dominate due to the Cr_{eq}/Ni_{eq} values being within 1.4-1.95 [58]. However, it has been reported that primary austenite formation dominated despite FA solidification mode due to high cooling rates [59,60]. Therefore, the risk of a high ferrite volume in the PBF-LB printed parts remains low. This statement can be confirmed with the investigation done by Pinto et al. [43], in which a noticeable increment of δ-ferrite was detected (6 vol.%) in the reused powder. Independently of the phase fractions of the reused powder feedstock they used, δ-ferrite-free 316 L steel parts were printed.

Ferrite in 316L powder can also lead to an increase in powder agglomeration due to its magnetic properties. This subsequently affects the packing density of the powder bed, which eventually favors building defects. When ferrite is present in the as-built specimens, this has been manifested by a slight increase in yield strength value, a slight decrease in ductility, and higher susceptibility to stress corrosion cracking and localized corrosion [56,61]. Therefore, it is advised that magnetic separation is performed after or during sieving. Controlling the ferrite formation during the laser process is more challenging. However, this can be regulated by adjusting the laser parameters, e.g., laser powder density, or even after post-processing heat treatment [58].

Additional changes in the reused powder are seen as changes in the grain size (Figure 6.9). Rapid solidification of the ejecta particles leads to a decrease in the grain size within the particles and on their surface. Grain sizes fluctuated between 45 nm to $\geq$ 100 μm and <5 nm to 84 μm for virgin and reused powder, respectively. Solidification rates for atomization and PBF-LB processes are similar (10^4-10^6 K/s); however, slower gas flow occurs during atomization, which may be a reason for the larger grain size.

Compared to the virgin powder, the reused powder has a stronger $\{001\}\gamma$ texture relative to the surface [001]. There were no representative trends of texture preferences, as only a small fraction of reused powder was analyzed. The extent to which the drastic microstructural differences in the heat-affected powder would affect the quality of the print parts remains an open question.
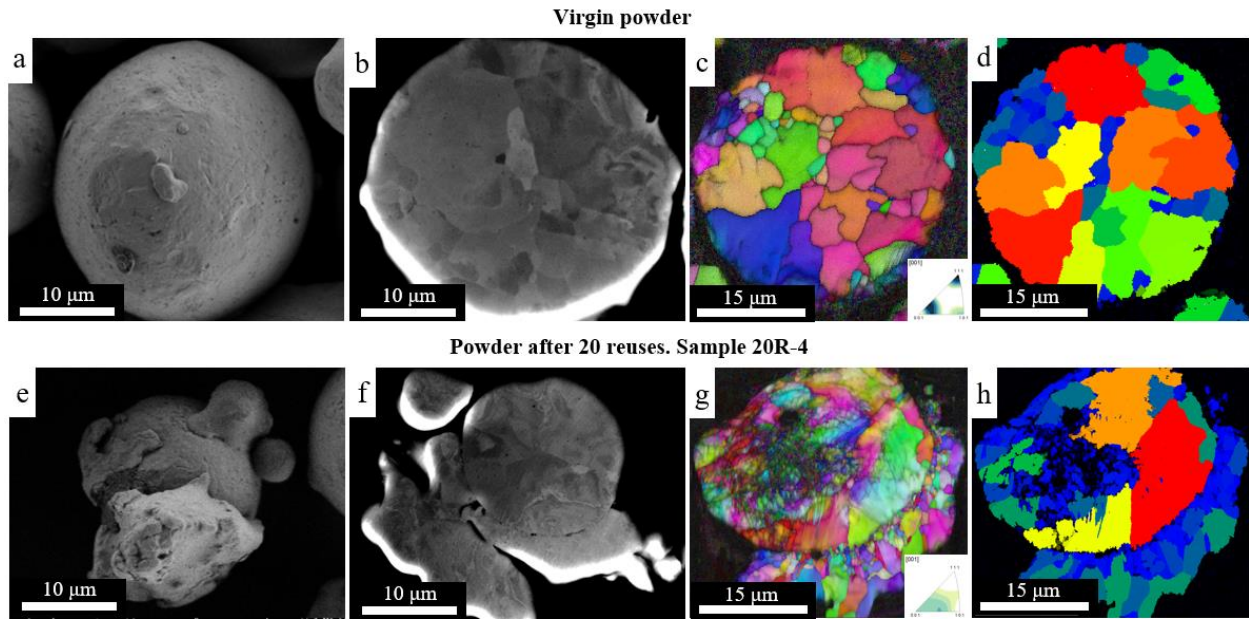
Figure 6.9 SEM-BSE images of bulk (a,e) and cross sections (b,f) particles. Virgin powder (a-d) and reused powder (e-h). Pole figure maps (c,g). Grain size distribution maps (d,h). Polished particles are representatively similar to the bulk powder on (a,e).

6.4.2   Effect of reused powder on the microstructure and chemical composition of the printing components

The influence of the reused powder properties on the microstructure of the printed components has yet to be investigated thoroughly. This is mainly due to most of the studies reported in the literature, the powder feedstock was far from its end of life, leading to low variability and still acceptable printing qualities [47]. In this study, we found changes related to porosity, the volume fraction of oxide nano-inclusions, the strength of tensile specimens, and an increase in N and C content.

6.4.2.1   Increase in porosity

Figure 6.10 compares the builds printed with virgin powder (Figure 6.10a-c) and after 20 reuses (Figure 6.10d-f). Porosity slightly increased after a high number of reuses; however, this defect was not critical as the tensile properties of the parts were not detrimentally affected. Tensile properties will be discussed in section 6.4.3. Based on the powder changes observed, the increment in porosity may mainly

be dominated by differences in 1) powder spreadability, 2) internal porosity of the reused powder, and 3) surface oxides.
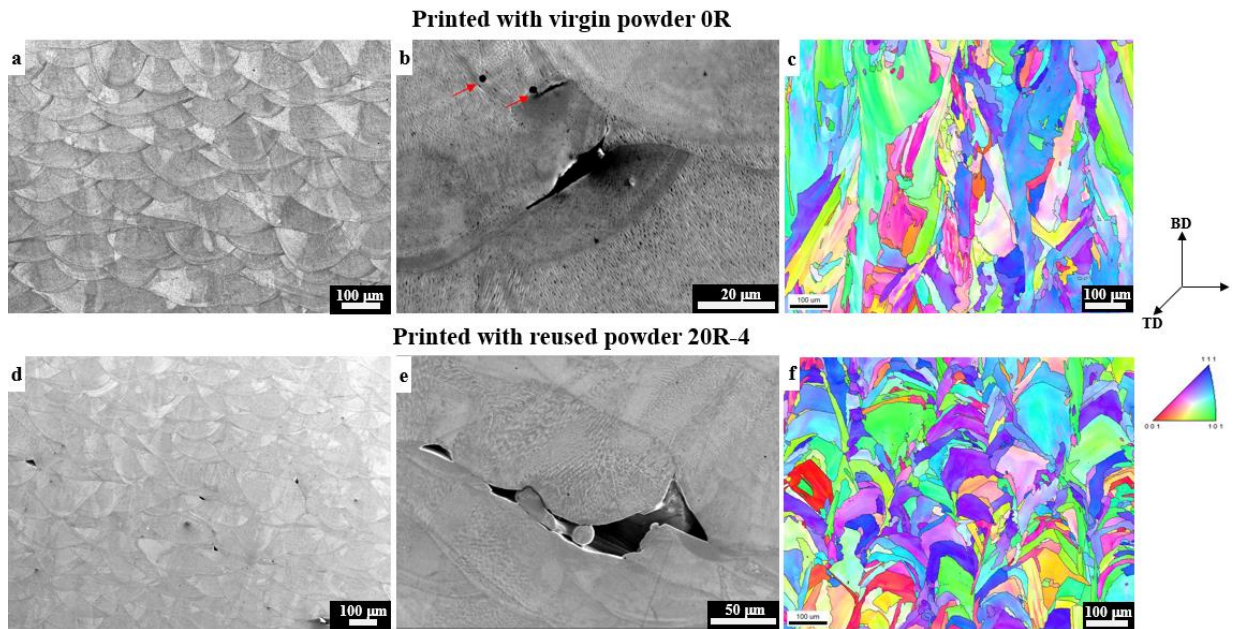
Figure 6.10 Comparison of as-printed parts after zero (a-c) and 20 reuses (d-f). After zero reuses, the microstructure presented microporosity, including a lack of fusion at the bottom of the melt pool and spherical porosity, indicated with red arrows (b). Elongated columnar grains along the build direction for printed parts with VP (c). There is a slight increase in the lack of fusion after 20 reuses (d, e). More quasi-equiaxed grains were observed in parts using reused powder after 20 cycles (f).

Powder spreading is the first critical step that rules the quality of the layer and its fusion. To avoid a reduction in powder bed density, the recoating process was designed to feed the powder bed with 200 % more powder than is needed to compensate for the differences in powder size and shape. However, cluster formation still can occur, hindering the spreading process [62]. So far, only one study in stainless steel powder reusability by Sutton et al. [38] has reported differences in powder bed densities at various locations of the build plate. Although, in this investigation, the variability in powder bed density was not directly correlated to the powder properties. Further studies on the spreading dynamics of reused powder are needed to assess its effects on defect formation. Inconsistencies in the spread layer can also develop a lack of fusion, as some gaps might remain after the melting ends. As a result, the surface of this location becomes rough, causing obstructions to the flow of the molten material when the next layer of powder is melted. This will further develop into multi-layer defects [44, 64].

As shown in Figure 6.3e-f on page 108, the porosity within powders has a combination of spherical and irregular shapes. There appears to be a correlation between the spherical porosity in reused powder to the trapped porosity formed in the atomization process and the argon-entrapped gas used during the laser

process. On the other hand, irregular voids are the product of the repetitive collisions of ejected molten metal due to the rapid solidification rates. The transferability of the trapped gas pore of the powder to the as-fabricated part has been studied using in situ X-Ray Synchrotron experiments [18, 64, 65]. Leung et al. [66] analyzed the pore formation and evolution mechanism while depositing the first and second-layer melt tracks. They reported that the powder with trapped porosity might remain within the melt pool depending on the competition between the Marangoni-driven flow and the buoyancy forces as the solidification progresses. Most of this porosity can escape into the atmosphere via bursting caused when the buoyancy forces dominate. As reported by Gordon et al. [65], almost 90 % of porosity was eliminated by this mechanism.

The porosity generated in the as-solidified melt track may also be caused by the increase in surface oxide in the powder feedstock and oxygen uptake at the melt pool surface [67]. Narasimharaju et al. [22] reported that when oxide layers grow thicker (10-100 um), these oxide films cannot be entirely evaporated by the stirring action of the laser beam and Marangoni flow. Consequently, oxide trapping can occur, leading to the formation of oxide inclusions of various sizes. Coarse oxide residues may reduce melt permeability [68], which leads to inappropriate fusion of the subsequent layers inducing part porosity. In this study, oxide inclusions are observed for all powder conditions. However, the maximum oxygen content increase observed was less than 5% after 20 reuses (sample 20R-4), as shown in Table 6.2 on page 112). This is similar in comparison to other powder reuse studies [47]. Despite the low oxygen increase in the printed parts after 20 reuses, the volume fraction and size of the oxides increased by 47% compared to zero reuses (Table 6.4, Figure 6.11). Volume fraction and size values correspond to the average calculation of 10 images analyzed for each condition using the Image-J software.

6.4.2.2   Increase in nano-inclusions

It was found that the nano precipitates for samples printed with virgin and reused powder are rich in Mn, Si, and transition-metal-rich, as shown in Figure 6.11. The inclusions were observed within and at the edge of the cell structures with average sizes after zero and 20 reuses being 39 nm and 54 nm, respectively. The volume fraction increases after 20 reuses showing a more uniform distribution within the microstructure.

So far, none of the studies in powder reusability for 316L have associated negative consequences due to oxide inclusions using powder feedstock with an oxygen level below 1000 ppm. This could be explained by the fact that this upper oxygen limit may not be high enough to lead to significant melt pool instabilities and affect the solidification dynamics. As reported by Yang et al. [21], 316L atomized powder with low (355 ppm), medium (1575 ppm), and high surface oxide content (4800 ppm) indeed caused significant differences in the melt and solidification behavior. However, the sample with lower

oxygen content was far from causing detrimental consequences as oxides were fine and uniformly distributed in the matrix. Similarly, the medium concentration (above the oxygen reported in powder reuse studies) was still in a zone with a lower risk of causing oxide agglomeration and promoting only undesired coarse and elongated columnar grain growth. In the study reported by Chia et al. [17], more consequences of the effect of oxygen in the melt pool dynamics are discussed, even considering the effect of powder reusability.

This area of investigation should be further explored as insufficient data is available to predict oxidation growth and the oxide content threshold at which the 316L powder will reach its end of life. Microstructure heterogeneities within samples of the same build, corrosion susceptibility, and premature failure under impact or fatigue loading are also other areas that may be affected by the increase of oxygen content in the powder.
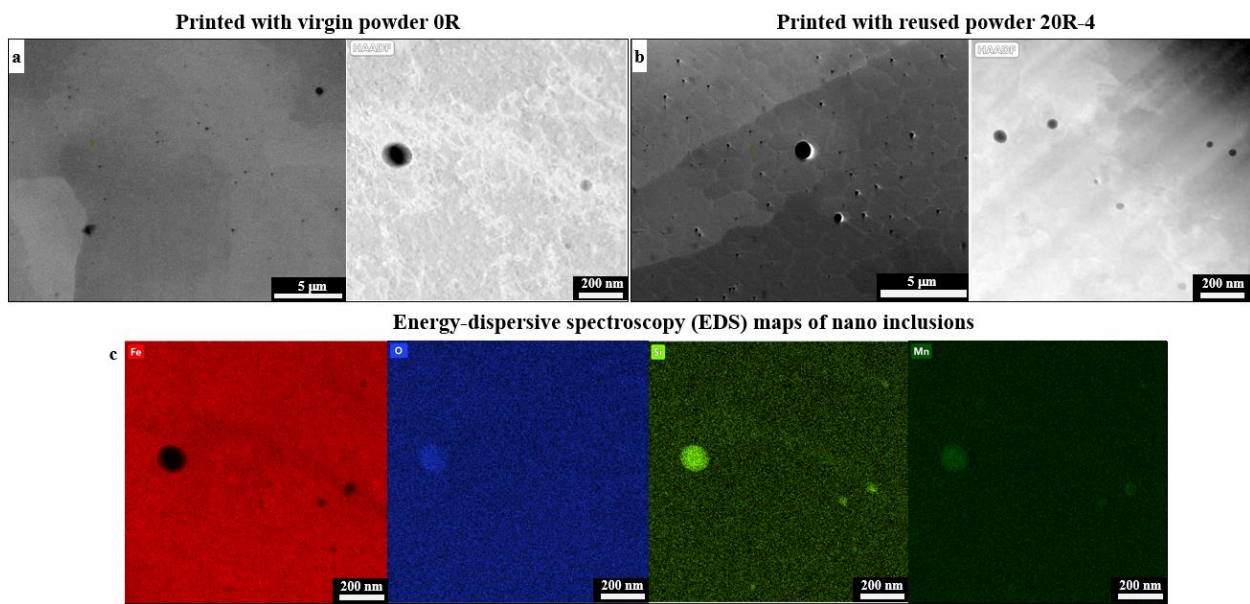
Figure 6.11 SEM and TEM micrographs of as-built samples after zero reuses (a) and 20 reuses (b) showing the distribution of nano inclusions. EDS mappings (c) revealed that the inclusions were rich in Si and Mn.

6.4.2.3 Change in grain size and shape

Both samples present epitaxial growth between adjacent layers. The average grain size, including LAGBs and HAGBs, for sample 20R-4 was 52 μm with quasi-equiaxed grains compares to the initial condition. After zero reuses, the grains were more elongated parallel to the build direction with a slightly larger average size of 69.3 μm. The increase in the volume fraction of the nano inclusions with a uniform

118

dispersion after 20 reuses may be the reason for the change in grain morphology. These particles can potentially control the solidification microstructure by developing a large constitutional supercooling zone ahead of the S/L interface. As a result, this causes a high density of heterogeneous nucleation sites, which induces near equiaxed grain formation [69].

Nano inclusions and the in-situ formation of Si and Mn oxides are commonly observed at 316L AM stainless steel [70-72]. However, the presence of these structures has not been reported as sufficient to form fully equiaxed grains in the as-printed condition. This is due to their nucleation potency, growth restriction factor (Q), particle spacing, or chemical stability are not enough to generate sufficient undercooling to trigger equiaxed nucleation. Other external factors might contribute due to the intrinsic dynamic solidification nature of PBF-LB processes.

6.4.2.4 Increase in nitrogen and carbon content

Nitrogen and carbon from the powder were transferred to the printed parts as a similar composition was observed in the powder feedstock (Table 6.2 on page 112). Like the powder feedstock and based on the XRD and TEM data from Figure 6.11 and Figure 6.12, built specimens only present an austenitic microstructure with no evidence of the formation of carbides or nitrides. The presence of both elements may lead to an increase in interstitial solute strengthening. However, nitrogen is more effective as a strengthening agent when retained in a solid solution than carbon [73].

It has been reported that an increase in nitrogen content in 316L SS AM parts resulted in a significant increase in yield strength. Boes et al. [53] compared the tensile strength of 316L printed samples with powder with nitrogen levels of 0.016 mass %, 0.065 mass % (similar to this current study), and 0.27 mass %. With the highest nitrogen content, the tensile strength and yield strength increased by 22 % and 21 %, respectively, while the uniform elongation reduced by 25 %. For the case of 0.065 mass %, the increase in strength was negligible, while the uniform elongation was reduced by 11 %. Pauzon et al. [51] reported a slight difference in tensile properties for samples with a nitrogen level of 0.075 mass %, representing a 4% increase from the virgin condition. Further investigations of the effect of nitrogen on powder reusability are necessary to confirm its impact not only in tensile properties but in corrosion, wear, fatigue, creep resistance, and strain hardening [74].
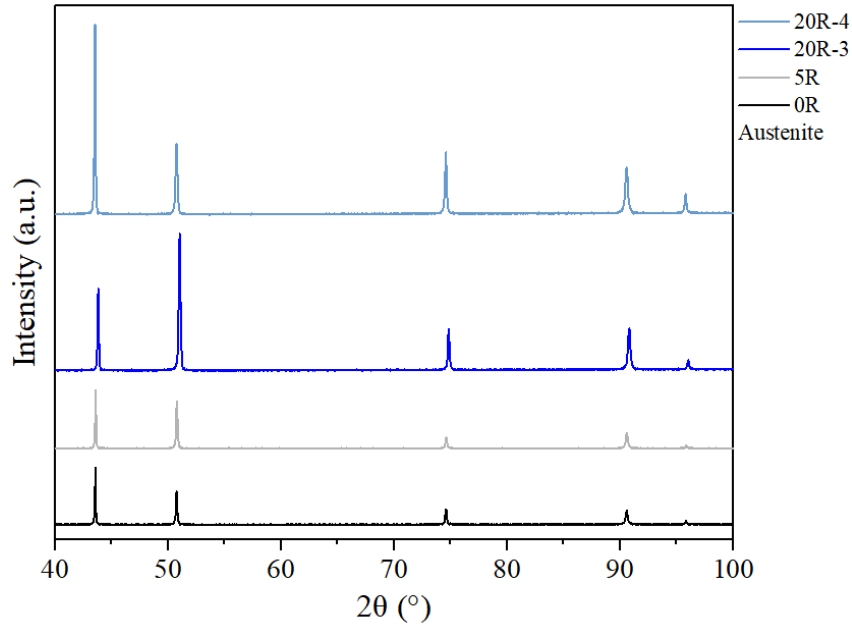
Figure 6.12 XRD diffractogram of as-printed samples after 0, 5, and 20 reuses. Only the austenite phase was detected.

6.4.3 Effect of reused powder on the mechanical properties of the printing components

No significant changes in mechanical properties were observed within 700 printing hours. However, the sample 20R-4 (~1000 printing hours) exhibited an increase in strength compared to zero reuses (Figure 6.13). The yield and tensile strength increased by 12 % and 6 %, respectively. At the same time, the uniform elongation was reduced by 17%. Table 6.3 shows the summary of the tensile data for each powder batch. Compared to batch 20R-3, the 300 hours difference in printing time and six more months of storage time in powder batch 20R-4 might have been the reason for the increase in strength. The possible strengthening causes are related to the combination of many structural and chemical heterogeneities, including solidification/dislocation structures, sub-grain cellular structures, LAGBs, HAGBs, and segregated elements [32]. In section 3.3, individual strengthening mechanisms will be discussed to understand the dominant contributors to the strength.

The addition of 10 % of spatter particles did not negatively affect the mechanical behavior of the samples as the UTS, yield strength, and uniform elongation values reported were only ~4% lower than samples 20R-4. This was probably due to insufficient volume of spatter particles to cause detrimental effects. Another possible reason could be related to the tensile specimens being cut from the middle of the printed part. This location may not represent the powder's total distribution within the build. The variability within the build plate location and height should be considered for the mechanical testing for

120

powder reusability. For 316L, this has not been proven, although, for Ti-6Al-4V alloys, variation of strength with build height has been confirmed by Derimow et al. [75].

In general terms for PBF-LB processes, anomalous events may be unnoticed due to the challenge of being detected. Additionally, more statistically relevant populations of samples need to be characterized and mechanically tested. Boyce et al. [76] demonstrated how collecting large datasets of tensile data can reveal substantial variability within and in between builds. As a result, the data can be connected to rare defects. In their study, the occurrence of these defects was not directly correlated with powder change. However, their approach may help unravel the uncertainty of how the powder variation can affect the mechanical behavior of the printed parts after several reuses.

Microhardness data (Table 6.3) did not reveal changes among builds, as all the values reported were within the standard deviation range. The average values fluctuated from 222 HV (zero reuses) to 238 HV (20 reuses). To evaluate possible variability within the sample height, 300 indents were distributed along three locations, 100 at the bottom, 100 at the center, and 100 at the top. The average in each area was within the range mentioned above.
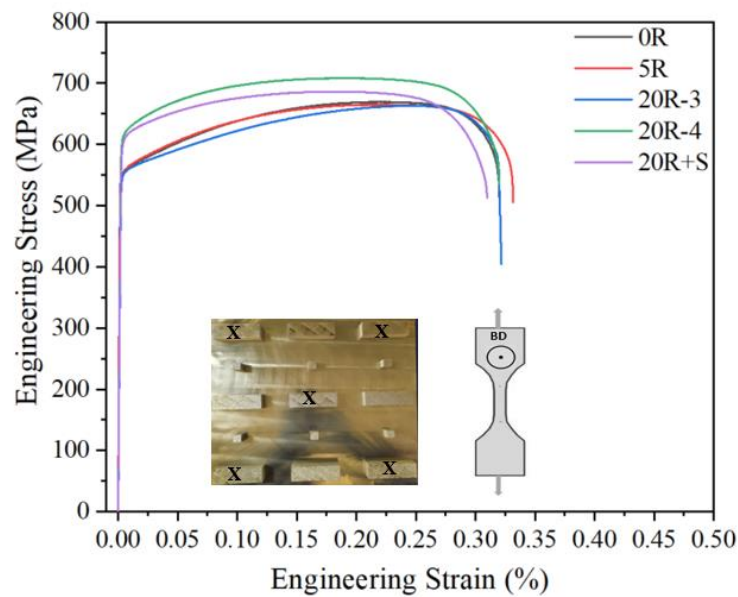

Figure 6.13 Differences in tensile properties of as-printed samples after reuse. Samples marked with the letter X correspond to where tensile specimens were cut.

Table 6.3 Mechanical properties of as-printed specimens after reuse. Values within parenthesis are standard deviations.

Mechanical Properties	0R	5R	20R-3	20R-4	R+S
UTS (MPa)	666.7 (6.8)	665.1 (4.7)	665.5 (3.1)	709.3 (3.1)	686.3 (2.7)
Yield Stress at 0.2% (MPa)	554.4 (2.9)	554.4 (10.1)	552.0 (6.6)	618.5 (6.5)	604.3 (3.4)
Uniform Elongation (%)	21.8 (1.3)	21.6 (1.2)	22.1 (1.4)	18.0 (0.6)	17.5 (0.4)
Microhardness along build direction (HV)	222 (8.6)	227 (9.5)	226 (6.9)	234 (7.5)	238 (6.3)

6.4.4   Strengthening effect

Dislocation and grain boundary strengthening have been commonly reported as the main contributors to the strengthening of PBF-LB 316L SS. However, due to the complexity of PBF-LB, the combined contribution of each mechanism is not well understood, as well as the quantitative relationship between each mechanism and the yield strength. To the best of the author's knowledge, powder reusability has not been contemplated for strengthening mechanisms in 316L SS. In this study, we identified that the increase in oxide precipitation, interstitial elements, dislocation density, and equiaxed grain formation are potential sources that could contribute to the strengthening. The following considerations were implemented for each strengthening mechanism according to the microstructural parameters and chemical composition obtained in the printed parts after zero and 20 reuses.

6.4.4.1   Particle strengthening

Despite the evidence for the negative influence of oxide inclusions in PFB-LB, researchers have also demonstrated that in-situ oxides formation induces strengthening effects in 316L AM [70]. Nano inclusions have a significant role in pinning dislocations to the cell walls, thereby contributing to a higher strengthening and dislocation nucleation rate. Therefore, the Orowan strengthening mechanism is considered as this method represents how dislocations interact with the precipitates. Orowan dislocation bypassing is used as the operative mechanism for all the precipitates regardless of the possible chemical composition and crystal structure changes. According to [30, 77], the Orowan equation is:

$$\sigma_p = M \frac{0.4Gb}{\pi\sqrt{1-\nu}} \frac{In\left(\frac{2\sqrt{\frac{2}{3}}r}{b}\right)}{\lambda_p} \tag{6.1}$$

Where M, G, b, r, λ_p, and ν are defined in Table 6.4 on page 127. The average particle spacing can be calculated as follows:

$$\lambda_p = 2\left(\sqrt{\frac{2}{3}}\ r\right)\left(\sqrt{\frac{\pi}{4f}}-1\right) \tag{6.2}$$

Where M is the mean orientation factor, G is the shear modulus, b is the burgers factor, ν is the Poisson ratio, r is the mean radius of the inclusion, and f is the volume fraction.

A yield strength contribution of 41 MPa and 38 MPa was obtained for samples with 0 and 20 reuses, respectively. The slight decrease in yield strength may be attributed to the increase in the mean radius and λ_p of the particles. Therefore, the increase in the volume fraction of oxides does not have a strong effect on the strengthening effect after a high number of reuses. Nevertheless, the inclusions' role in the increase in strength may be related to the formation of more equiaxed grains or the retention of dislocations inside the cell walls [78].

6.4.4.2 Solid solution strengthening

For compositional strengthening, only solid solution strengthening is considered as no microsegregation was observed in the TEM results. As previously reported, the difference in bulk composition after a high number of reuses was not significant, except for carbon and nitrogen content. Since no nitrides and carbides were detected, both elements were considered to be dissolved in the matrix. Both elements may contribute to the strengthening by accommodating the interstitial sites in the lattice. To evaluate the contribution of both elements, the following solid solution-strengthening mechanism is implemented [33,79]:

$$\sigma_{SS} = \sum_i K_i C_i \tag{6.3}$$

Where K_i is the strengthening coefficient of i-th alloying elements, C_i is the i-th alloying elemental concentration in wt. %. The values for K_i were taken from the literature reported by Chen et al. [33] and Yusuf et al. [80]. Based on the calculations, a minimal increment from 101 MPa to 106 MPa was

observed for the samples with 0R and 20R, respectively. Additional contributions of nitrogen in the increase in strength may be associated with its influence on grain refinement (Hall-Petch strengthening) [74,81] and possibly dispersion strengthening.

6.4.4.3   Grain boundary strengthening

Due to the complex microstructure obtained in PBF-LB, this mechanism is dominated by the interaction among dislocations, submicron cellular structures, grains, and subgrains. The approach taken to calculate this strengthening mechanism was reported by Sabzi et al. [29]. In contrast to the conventional Hall-Petch relationship that only considers high-angle grain boundaries as effective barriers [30, 82], they derived a relationship that contemplates low and high-grain boundaries. Samples printed by PBF-LB contain a significant fraction of LAGBs [29, 32, 78]. Subgrains surrounded by LAGBs have been attributed as essential strengthening sources for austenitic steels because they could carry high dislocation contents in their boundaries.

The Hall–Petch-type equation is given by:

$$\sigma_{GB} = 197.3 + \frac{1189}{\sqrt{d_{LAGB}}} \qquad (6.4)$$

Where 197.3 is the dislocation hardening term, and 1189 is the Hall–Petch coefficient. To determine the grain size with only LAGBs (d_{LAGB}), the following relationship was used:

$$d_{LAGB} = d_G \cdot [1 - X_{LAGB}] \qquad (6.5)$$

Where d_G is the actual grain size considering only HAGBs and X_{LAGB} is their fraction. The calculated values can be found in Table 6.4.

As observed in Figure 6.14, the fraction of LAGBs decreases by almost 50% after a high number of reuses. This difference resulted in a smaller contribution of the strength of 392 MPa after 20 reuses. The value reported after zero reuses was 415 MPa. The decrease in the volume fraction of LAGBs could be related to the increase in the volume fraction of inclusions. Since the nano inclusions were homogeneously distributed, grain boundary mitigation and coalescence may have been promoted by their wetting affinity with the surrounded matrix. In this scenario, the inclusions facilitate the growth of quasi-equiaxed grains, causing a reduction in the overall number of grain boundaries, including LAGBs. As the grains grow and coalesce, the LAGBs are consumed, resulting in a lower volume fraction in the final microstructure.

Even if the traditional Hall-Petch method is implemented, the value obtained after 20 reuses is still smaller due to the slight increase in grain size in the printed parts. These results show that the variation in grain size and subgrains does not justify the increase in yield strength we observed for samples 20R-4 and 20R+S. Li et al. [83] reported the same trend when the grain boundary strengthening was calculated for the as-printed parts with columnar and equiaxed grains. However, they confirmed the reason for strengthening the sample with equiaxed grains based on the dislocation strengthening mechanism. They reported that equiaxed regions presented a larger Taylor factor, suggesting that more energy is required to deform equiaxed grains than columnar grains.
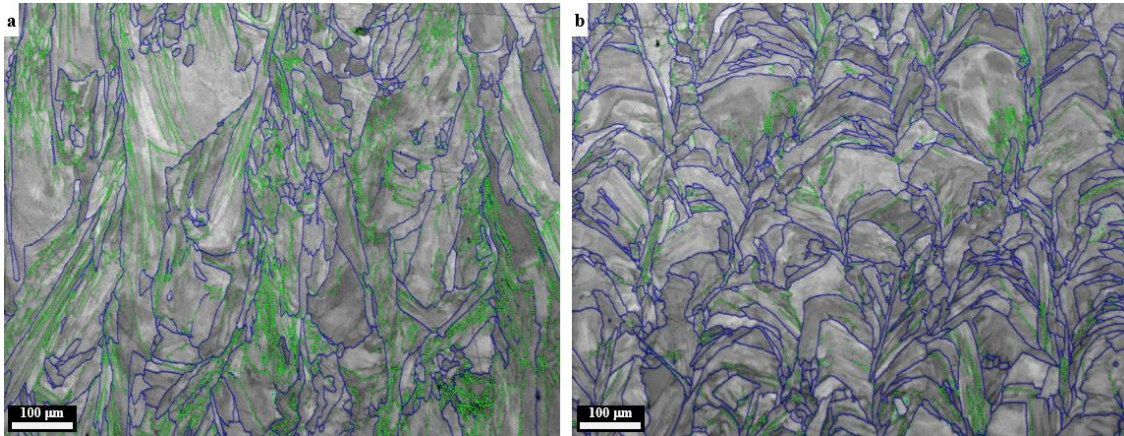
Figure 6.14 Grain boundary maps show more volume fraction of LAGBs (green boundaries) in samples after zero reuses (a) than after 20 reuses (b). HAGBs are indicated with blue boundaries.

6.4.4.4   Dislocation strengthening

Dislocations are normal features in as-built components which decorate the submicron cellular structures. Even though they are considered crystallographic defects, dislocations are a critical factor in determining the strength of AM 316L SS. The Taylor-strengthening relationship (equation 6.6) was used for this calculation to obtain the yield strength contribution [78, 80].

$$\sigma_\rho = M\alpha Gb\rho^{\frac{1}{2}} \tag{6.6}$$

The total dislocation density, ρ, is calculated using a modified Williamson-Hall (mW-H) method based on the XRD patterns. The mW-H analysis is able to deconvolute the contributions of crystallite size and crystallite strain to peak broadening of XRD peaks after adjusting for the contribution of instrument broadening. By accounting for strain anisotropy in a contrast factor term, $\overline{C}$, it is possible to determine the total strain contribution, β_{strain} and $\beta_{crystallite}$, dislocation density, and crystallite size, D, from each peak

125

reflection FWHM value. The dislocation density can be related to the contrast factor through the following equations [84,85].

$$\Delta K = \frac{0.9}{D} + \left(\frac{\pi M^2 b^2}{2}\right)^{\frac{1}{2}} + \rho^{\frac{1}{2}} + K\,\overline{C}^{\frac{1}{2}} \tag{6.7}$$

Where:

$$K = \frac{2\sin\theta_\beta}{\lambda} \tag{6.8}$$

$$\Delta K = \frac{\cos\theta_\beta(\beta_{strain} + \beta_{crystal})}{\lambda} \tag{6.9}$$

$$\overline{C} = \overline{C}_{h00}\left(1 - qH^2\right) \tag{6.10}$$

$$H^2 = \frac{\left(h^2k^2 + h^2l^2 + k^2l^2\right)}{\left(h^2 + k^2 + l^2\right)} \tag{6.11}$$

Where ΔK is a function of the cosine of the Bragg angle, θ_B, the wavelength of XRD radiation, λ, and the broadening contribution from the crystallite strain and the crystallite size, β_{strain}, and $\beta_{crystallite}$, respectively. K is related to the sine of the Bragg angle and the wavelength of XRD radiation. The contrast factor is related to q and $\overline{C}_{h00}$, which are constants dependent on dislocation character, and H is a function of the Miller indices of each peak reflection. M is a dimensionless value sensitive to dislocation parameters [85]. For this work, M was chosen to be 3. The symbol b is the magnitude of the Burgers vector; in this case, *b* is 0.254 nm for 316L. The calculated values can be found in Table 6.4.

With this mechanism, the difference in yield strength after reuse was more significant than the other strengthening mechanisms. The calculated contribution for yield strength after zero reuses was 361 MPa, while the sample after 20 reuses was 519 MPa. This suggests that dislocation density increases with the number of reuses and also as quasi-equiaxed grains surrounded by HAGBs are formed. In general, HAGBs tend to have more dislocation structures than LAGBs. This is because the presence of dislocations helps accommodate the misfit and strain across the boundary, reducing the overall energy associated with the grain boundary.

It is worth noting that this method has limitations in evaluating strain effects for 3D printed materials. Dislocation cells in as-printed parts are not traditionally deformation-induced dislocation walls [31]. Therefore, the dislocation arrangement into the dislocation boundaries with specific misorientations should be considered [33]. However, due to the complex microstructure of the printed parts, a statistically representative dislocation density is challenging to obtain by only using TEM analysis.

Table 6.4 Parameter values used in calculations for the strengthening mechanisms and their corresponding results.

Mechanism	Constant name	Symbol	Value	References	Final results (MPa)	
					0R	20R-4
Particle Strengthening	Mean Orientation factor	M	3	Chen et al. [33]		
	Shear modulus	G	78000 MPa	Chen et al. [33]		
	Burger's vector	b	0.26 nm	Chen et al. [33]		
	Poisson ratio	ν	0.3	Li et al. [31]		
	Mean radius of inclusions	r	0.04 µm (0R) 0.054 µm (20R-4)	This work (SEM)	41	38
	Volume fraction	f	0.19 (0R) 0.28 (20R-4)	This work (SEM)		
	Average particle spacing	λ_p	1.24 µm (0R) 1.39 µm (20R-4)	Zhang et al. [77]		
Solid solution strengthening	Strengthening coefficient	K_{Cr}	1	Eliasson et al. [86]	101	106
		K_{Ni}	5	Eliasson et al. [86]		
		K_{Si}	8.7	Mohd Yusuf et al. [80]		
		K_{Mn}	-1.5	Eliasson et al. [86]		
		K_{Cu}	-18	Mohd Yusuf et al. [80]		
		K_{Mo}	19.5	Mohd Yusuf et al. [80]		
		K_N	219.6	Chen et al. [33]		
		K_C	157.8	Chen et al. [33]		

Table 6.4 Continued

Grain boundary strengthening	Grain size only HAGBs	d_G	69.3 μm (0R) 52.5 μm (20R-4)	This work (EBSD)		
	Grain size only LAGBs	d_{LAGBs}	29.75 μm (0R) 37.2 μm (20R-4)	Sabzi et al. [29]	415	392
	LAGBs fraction	X_{LAGBs}	0.57 (0R) 0.29 (20R-4)	This work (EBSD)		
	HAGBs fraction	X_{HAGBs}	0.43 (0R) 0.71 (20R-4)	This work (EBSD)		
Dislocation strengthening	Lattice constant	α	0.24	Chen et al. [33]		
	Contrast factors	C	C_{11}, C_{12}, C_{44}	Voisin et al. [78]	361	519
	Dislocation density	ρ	6.31×10^{14} (0R) 1.31×10^{15} (20R-4)	This work (mW-H)		

6.5   Conclusions

This work provides new insights into possible changes in tensile properties of as-printed parts after several reuses. After 20 reuses, equivalent to 1000 hours of total printing time, the yield strength and UTS increased by 12 % and 6 %, respectively, while the uniform elongation decreased by 17%. With these results, it can be confirmed that the powder changes did not cause detrimental changes in the microstructure and mechanical performance after 20 reuses. Among the most relevant changes in the powder feedstock, we found that an increase in nitrogen and carbon stood out as a significant difference compared to the current literature on powder reusability for 316L SS. Contrary to what has been reported, the oxygen content was steady throughout all reuses. The same changes in chemistry were observed in the as-printed parts. Regardless of the low variability in oxygen level, an increase in nano-inclusions was observed in the microstructure. These inclusions may serve as the primary contributor to the formation of slightly finer and more quasi-equiaxed grains after 20 reuses. The changes in dislocation structures, grain boundaries, and subgrains due to the formation of quasi-equiaxed grains may explain the variation in yield strength. Additionally, the contribution of the dispersions of carbon and nitrogen as interstitials in the matrix may be potential sources of strengthening as well.

Based on the strengthening mechanisms, we found that grain boundary and dislocation strengthening were the predominant contributors to yield strength. Nonetheless, further comprehensive knowledge is needed to develop more accurate methods for the complex microstructures obtained in PBF-LB. Despite the improvement in strength after reuse, there are still other properties that are required to be tested, such as fatigue life, to have a better understanding of the effect of powder reusability. Anisotropy in properties that should be considered, as well as fatigue and corrosion performance.

6.6   References

1. Delacroix, T., Lomello, F., Schuster, F., Maskrot, H., & Garandet, J.-P. (2022). Influence of powder recycling on 316L stainless steel feedstocks and printed parts in laser powder bed fusion. Additive Manufacturing, 50, 102553

2. Heiden, M. J., Deibler, L. A., Rodelas, J. M., Koepke, J. R., et al. (2019). Evolution of 316L stainless steel feedstock due to laser powder bed fusion process. Additr, 25, 84–103.

3. Lu, C., Zhang, R., Xiao, M., Wei, X., Yin, Y., et al. (2022). A comprehensive characterization of virgin and recycled 316L powders during laser powder bed fusion. *Journal of Materials Research and Technology*, *18*, 2292–2309.

4. Gorji, N. E., O'connor, R., Mussatto, A., Snelgrove, M., Mani González, P. G., & Brabazon, D. (2019). Recyclability of stainless steel (316 L) powder within the additive manufacturing process. Materialia, 8, 100489. https://doi.org/10.1016/j.mtla.2019.100489

5. Sartin, B., Pond, T., Griffith, B., Everhart, W., Elder, L., Wenski, E., Cook, C., Wieliczka, D., King, W., Rubenchik, A., Wu, S., Brown, B., Johnson, C., & Crow, J. (2017). 316L Powder Reuse for Metal Additive Manufacturing. https://repositories.lib.utexas.edu/handle/2152/89828

6. Lhuissier, P., Hébrard, L., Bataillon, X., Lapouge, P.,et al. (2022). Miniature laser powder bed fusion system for *in situ* synchrotron x-ray micro-computed tomography experiments at the European Synchrotron Radiation Facility. *Review of Scientific Instruments*, 93,083701. https://doi.org/10.1063/5.0090623

7. Moghimian, P., Poirié, T., Habibnejad-Korayem, M., Zavala, J. A., et al. (2021). Metal powders in additive manufacturing: A review on reusability and recyclability of common titanium, nickel, and aluminum alloys. Additive Manufacturing, 43, 102017.

8. Le, P., Wang, X., Seita, M. (2022). An optical-based method to estimate the oxygen content in recycled metal powders for additive manufacturing. Additive Manufacturing, 59 Part A, 103127.

9. Spierings, A. B., Herres, N., & Levy, G. (2011). Influence of the particle size distribution on surface quality and mechanical properties in AM steel parts. Rapid Prototyping Journal, 17(3), 195–202. https://doi.org/10.1108/13552541111124770

10. Chen, H., Wei, Q., Zhang, Y., Chen, F., Shi, Y., & Yan, W. (2019). Powder-spreading mechanisms in powder-bed-based additive manufacturing: Experiments and computational modeling. Acta Materialia, 179, 158–171. https://doi.org/10.1016/j.actamat.2019.08.030

11. Cordova, L., Campos, M., & Tinga, T. (2019). Revealing the Effects of Powder Reuse for Selective Laser Melting by Powder Characterization. JOM, 71(3), 1062–1072. https://doi.org/10.1007/S11837-018-3305-2/FIGURES/7

12. Ahmed, F., Ali, U., Sarker, D., Marzbanrad, E., Choi, K., Mahmoodkhani, Y., & Toyserkani, E. (2020). Study of powder recycling and its effect on printed parts during laser powder-bed fusion of 17-4 PH stainless steel. Journal of Materials Processing Technology, 278, 116522. https://doi.org/10.1016/J.JMATPROTEC.2019.116522

13. Meier, C., Weissbach, R., Weinberg, J., Wall, W. A., & Hart, A. J. (2019). Critical influences of particle size and adhesion on the powder layer uniformity in metal additive manufacturing. Journal of Materials Processing Technology, 266(May 2018), 484–501. https://doi.org/10.1016/j.jmatprotec.2018.10.037

14. Rausch, A. M., Küng, V. E., Pobel, C., Markl, M., & Körner, C. (2017). Predictive Simulation of Process Windows for Powder Bed Fusion Additive Manufacturing: Influence of the Powder Bulk Density. Materials, 10(10). https://doi.org/10.3390/ma10101117

15. Xia, M., Gu, D., Yu, G., Dai, D., Chen, H., & Shi, Q. (2017). Porosity evolution and its thermodynamic mechanism of randomly packed powder-bed during selective laser melting of Inconel 718 alloy. International Journal of Machine Tools and Manufacture, 116, 96–106. https://doi.org/10.1016/j.ijmachtools.2017.01.005

16. Olakanmi, E. O., Dalgarno, K. W., & Cochrane, R. F. (2012). Laser sintering of blended Al-Si powders. Rapid Prototyping Journal, 18(2), 109–119. https://doi.org/10.1108/13552541211212096

17. Chia, H. Y., Wang, L., & Yan, W. (2023). Influence of oxygen content on melt pool dynamics in metal additive manufacturing: High-fidelity modeling with experimental validation. Acta Materialia, 249, 118824. https://doi.org/10.1016/J.ACTAMAT.2023.118824

18. Leung, C. L. A., Marussi, S., Towrie, M., Atwood, R. C., Withers, P. J., & Lee, P. D. (2019). The effect of powder oxidation on defect formation in laser additive manufacturing. Acta Materialia, 166, 294–305. https://doi.org/10.1016/j.actamat.2018.12.027

19. Galicki, D., List, F., Babu, S. S., Plotkowski, A., Meyer, H. M., Seals, R., & Hayes, C. (2019). Localized Changes of Stainless Steel Powder Characteristics During Selective Laser Melting Additive Manufacturing. Metallurgical and Materials Transactions A: Physical Metallurgy and Materials Science, 50(3), 1582–1605. https://doi.org/10.1007/s11661-018-5072-7

20. Gu, D., & Dai, D. (2016). Role of melt behavior in modifying oxidation distribution using an interface incorporated model in selective laser melting of aluminum-based material. Journal of Applied Physics, 120(8). https://doi.org/10.1063/1.4961410

21. Yang, X., Gao, F., Tang, F., Hao, X., & Li, Z. (2021). Effect of Surface Oxides on the Melting and Solidification of 316L Stainless Steel Powder for Additive Manufacturing. Metallurgical and Materials Transactions A: Physical Metallurgy and Materials Science, 52(10), 4518–4532. https://doi.org/10.1007/S11661-021-06405-3/FIGURES/14

22. Narasimharaju, S. R., Zeng, W., See, T. L., Zhu, Z., Scott, P., Jiang, X., & Lou, S. (2022). A comprehensive review on laser powder bed fusion of steels: Processing, microstructure, defects and control methods, mechanical properties, current challenges, and future trends. Journal of Manufacturing Processes, 75, 375–414. https://doi.org/10.1016/J.JMAPRO.2021.12.033

23. R. Li, J. Liu, Y. Shi, L. Wang, W. Jiang. (2012) Balling behavior of stainless steel and nickel powder during selective laser melting process. The International Journal of Advanced Manufacturing Technology, 59,1025–1035. https://doi.org/10.1007/s00170-011-3566-1

24. Yang, X., Tang, F., Hao, X., & Li, Z. (2021). Oxide Evolution During the Solidification of 316L Stainless Steel from Additive Manufacturing Powders with Different Oxygen Contents. Metallurgical and Materials Transactions B: Process Metallurgy and Materials Processing Science, 52(4), 2253–2262. https://doi.org/10.1007/S11663-021-02191-W/FIGURES/8

25. Simonelli, M., Tuck, C., Aboulkhair, N. T., Maskery, I., Ashcroft, I., Wildman, R. D., & Hague, R. (2015). A Study on the Laser Spatter and the Oxidation Reactions During Selective Laser Melting of 316L Stainless Steel, Al-Si10-Mg, and Ti-6Al-4V. Metallurgical and Materials Transactions A: Physical Metallurgy and Materials Science, 46(9), 3842–3851. https://doi.org/10.1007/S11661-015-2882-8/FIGURES/11

26. Soltani-Tehrani, A., Isaac, J., Tippur, H., Silva, D., et al. (2023). Ti-6Al-4V powder reuse in laser powder bed fusion (L-PBF): The effect on porosity, microstructure, and mechanical behavior. International Journal of Fatigue, 167, Part B, 107343. https://doi.org/10.1016/j.ijfatigue.2022.107343.

27. Liu, Y., Yang, Y., Mai, S., Wang, D., & Song, C. (2015). Investigation into spatter behavior during selective laser melting of AISI 316L stainless steel powder. JMADE, 87, 797–806. https://doi.org/10.1016/j.matdes.2015.08.086

131

28. Zhong, Y., Liu, L., Zou, J., Li, X., Cui, D., & Shen, Z. (2020). Oxide dispersion strengthened stainless steel 316L with superior strength and ductility by selective laser melting. Journal of Materials Science and Technology, 42, 97–105. https://doi.org/10.1016/j.jmst.2019.11.004

29. Sabzi, H. E., Hernandez-Nava, E., Li, X. H., Fu, H., San-Martín, D., & Rivera-Díaz-del-Castillo, P. E. J. (2021). Strengthening control in laser powder bed fusion of austenitic stainless steels via grain boundary engineering. Materials and Design, 212. https://doi.org/10.1016/j.matdes.2021.110246

30. Smith, T. R., Sugar, J. D., San Marchi, C., & Schoenung, J. M. (2019). Strengthening mechanisms in directed energy deposited austenitic stainless steel. Acta Materialia, 164, 728–740. https://doi.org/10.1016/j.actamat.2018.11.021

31. Li, Z., He, B., & Guo, Q. (2020). Strengthening and hardening mechanisms of additively manufactured stainless steels: The role of cell sizes. Scripta Materialia, 177, 17–21. https://doi.org/10.1016/j.scriptamat.2019.10.005

32. Wang, Y. M., Voisin, T., McKeown, J. T., Ye, J., Calta, N. P., Li, Z., Zeng, Z., Zhang, Y., Chen, W., Roehling, T. T., Ott, R. T., Santala, M. K., Depond, P. J., Matthews, M. J., Hamza, A. V., & Zhu, T. (2018). Additively manufactured hierarchical stainless steels with high strength and ductility. Nature Materials, 17(1), 63–70. https://doi.org/10.1038/NMAT5021

33. Chen, S., Ma, G., Wu, G., Godfrey, A., Huang, T., & Huang, X. (2022). Strengthening mechanisms in selective laser melted 316L stainless steel. Materials Science and Engineering A, 832(November 2021), 142434. https://doi.org/10.1016/j.msea.2021.142434

34. ASTM B822-20 (2006). Standard Test Method for Particle Size Distribution of Refractory Metal Powders and Related Compounds by Turbidimetry 1. 97(Reapproved), 1–5. https://doi.org/10.1520/B0822-20.2

35. ASTM E1019-18 (2018). Standard Test Methods for Determination of Carbon, Sulfur, Nitrogen, and Oxygen in Steel and in Steel, Iron, Nickel, and Cobalt Alloys by Various Combustion and Fusion Techniques. ASTM Book of Standards, 03.05, 22. https://doi.org/10.1520/E1019-18.2

36. ASTM E1086-14 (1999). Standard Test Method for Analysis of Carbon and Low-Alloy Steel by Spark Atomic. American Society for Testing and Materials, 1, 1–9. https://doi.org/10.1520/E1086-14.2

37. ASTM E8. (2010). ASTM E8/E8M standard test methods for tension testing of metallic materials 1. Annual Book of ASTM Standards 4, C, 1–27. https://doi.org/10.1520/E0008

38. Sutton, A. T., Kriewall, C. S., Karnati, S., Leu, M. C., & Newkirk, J. W. (2020). Characterization of AISI 304L stainless steel powder recycled in the laser powder-bed fusion process. Additive Manufacturing, 32(July 2019), 100981.

39. Saboori, A., Aversa, A., Bosio, F., Bassini, E., Librera, E., De Chirico, M., Biamino, S., Ugues, D., Fino, P., & Lombardi, M. (2019). An investigation on the effect of powder recycling on the microstructure and mechanical properties of AISI 316L produced by Directed Energy Deposition. Materials Science and Engineering: A, 766, 138360. https://doi.org/10.1016/J.MSEA.2019.13836

40. Quinn, P., O'Halloran, S., Lawlor, J., & Raghavendra, R. (2019). The effect of metal EOS 316L stainless steel additive manufacturing powder recycling on part characteristics and powder reusability.

Advances in Materials and Processing Technologies, 5(2), 348–359.
https://doi.org/10.1080/2374068X.2019.1594602

41. Yusuf, S. M., Choo, E., & Gao, N. (2020). Comparison between virgin and recycled 316l ss and alsi10mg powders used for laser powder bed fusion additive manufacturing. Metals, 10(12), 1–18. https://doi.org/10.3390/met10121625

42. Gasper, A. N. D., Szost, B., Wang, X., Johns, D., et al. (2018). Spatter and oxide formation in laser powder bed fusion of Inconel 718. Additive Manufacturing, 24, 446–456.

43. Pinto, F. C., Souza Filho, I. R., Sandim, M. J. R., & Sandim, H. R. Z. (2020). Defects in parts manufactured by selective laser melting caused by δ-ferrite in reused 316L steel powder feedstock. Additive Manufacturing, 31, 100979.

44. Mostafaei, A., Zhao, C., He, Y., Reza Ghiaasiaan, S., et al. (2022). Defects and anomalies in powder bed fusion metal additive manufacturing. In Current Opinion in Solid State and Materials Science (Vol. 26, Issue 2). Elsevier Ltd.

45. Taheri, M., Dehghani, R., & Karamooz-ravari, M. R. (2018). A study on the effect of energy input on spatter particles creation during selective laser melting process. Additive Manufacturing, 20, 33–43.

46. Santecchia, E., Spigarelli, S., & Cabibbo, M. (2020). Material reuse in laser powder bed fusion: Side effects of the laser—metal powder interaction. Metals, 10(3), 1–21.

47. Douglas, R., Lancaster, R., Jones, T., Barnard, N., & Adams, J. (2022). The Influence of Powder Reuse on the Properties of Laser Powder Bed-Fused Stainless Steel 316L: A Review. Advanced Engineering Materials, 2200596. https://doi.org/10.1002/ADEM.202200596

48. Derimow, N., Mansfield, E., Holm, J., Hrabe, N. (2023). Additive manufacturing titanium powder oxygen variation within a single powder bed due to differences in powder size and oxygen content. Additive Manufacturing Letters, 5, 100125, https://doi.org/10.1016/j.addlet.2023.100125

49. Vessels, O. P., Bars, S. S., Castings, R. A., Containing, M., Than, L., Percent, T., & Flowmeter, H. (n.d.). Standard Specification for Additive Manufacturing Stainless Steel Alloy (UNS S31603) with Powder Bed Fusion 1. i, 1–9. https://doi.org/10.1520/F3184

50. Vukkum, V.B., Christudasjustus, J., Darwish, A.A. et al. (2022). Enhanced corrosion resistance of additively manufactured stainless steel by modification of feedstock. Materials Degradation, **6**, 2. https://doi.org/10.1038/s41529-021-00215-z

51. Pauzon, C., Hryha, E., Forêt, P., & Nyborg, L. (2019). Effect of argon and nitrogen atmospheres on the properties of stainless steel 316 L parts produced by laser-powder bed fusion. Materials and Design, 179. https://doi.org/10.1016/j.matdes.2019.107873

52. Filimonov, AM., Rogozin, OA., Firsov, DG., Kuzminova, YO., et al. (2020). Hardening of Additive Manufactured 316L Stainless Steel by Using Bimodal Powder Containing Nanoscale Fraction. Materials (Basel), 14(1), 115. doi: 10.3390/ma14010115. PMID: 33383901; PMCID: PMC7794974.

53. Boes, J., Röttger, A., Becker, L., & Theisen, W. (2019). Processing of gas-nitrided AISI 316L steel powder by laser powder bed fusion – Microstructure and properties. Additive Manufacturing, 30(April), 100836. https://doi.org/10.1016/j.addma.2019.100836

54. Cui, C., Uhlenwinkel, V., Schulz, A., Zoch, H.-W. (2020). Austenitic Stainless Steel Powders with Increased Nitrogen Content for Laser Additive Manufacturing. *Metals*, *10*, 61. https://doi.org/10.3390/met10010061

55. Bertoli, U., Guss, G., Wu, S., Matthews, M.J., Schoenung, J.M. (2017) In-situ characterization of laser-powder interaction and cooling rates through high-speed imaging of powder bed fusion additive manufacturing, Materials Design,135, 385–396.

56. Kurzynowski, T., Gruber, K., Stopyra, W., Kuźnicka, B., & Chlebus, E. (2018). Correlation between process parameters, microstructure and properties of 316 L stainless steel processed by selective laser melting. Materials Science and Engineering A, 718(September 2017), 64–73. https://doi.org/10.1016/j.msea.2018.01.103

57. Zhongji, S., Tan, X., Beng Tor, S., Yee, W. (2016). Selective laser melting of stainless steel 316L with low porosity and high build rates. Materials & Design, 104, 197-204.

58. Astafurov, S., & Astafurova, E. (2021). Phase composition of austenitic stainless steels in additive manufacturing: A review. Metals, 11(7). https://doi.org/10.3390/met11071052

59. Zhang, X., Kenesei, P., Park, J.S., Almer, J., Li, M. (2021). In situ high-energy X-ray study of deformation mechanisms in additively manufactured 316L stainless steel. Journal of Nuclear Materials, 549, 152874. https://doi.org/10.1016/j.jnucmat.2021.152874.

60. Bahl, S., Mishra, S., Yazar, K.U. Kola, I., Chatterjee, K.,Suwas, S. (2019). Non-equilibrium microstructure, crystallographic texture and morphological texture synergistically result in unusual mechanical properties of 3D printed 316L stainless steel. Additive Manufacturing, 28, 65-77. https://doi.org/10.1016/j.addma.2019.04.016.

61. Chen, X., Li, J., Cheng, X., Wang, H., Huang, Z. (2018). Effect of heat treatment on microstructure, mechanical and corrosion properties of austenitic stainless steel 316L using arc additive manufacturing. Materials Science and Engineering. A, 715, 307–314.

62. Escano, L.I., Parab, N.D., Xiong, L. et al. (2018) Revealing particle-scale powder spreading dynamics in powder-bed-based additive manufacturing process by high-speed x-ray imaging. Scientific Reports, **8**, 15079. https://doi.org/10.1038/s41598-018-33376-0

63. Collins, P. C., Brice, D. A., Samimi, P., Ghamarian, I., & Fraser, H. L. (2016). Microstructural Control of Additively Manufactured Metallic Materials. Annual Review of Materials Research, 46(1), 63–91. https://doi.org/10.1146/annurev-matsci-070115-031816

64. Khairallah, S. A., Anderson, A. T., Rubenchik, A., & King, W. E. (2016). Laser powder-bed fusion additive manufacturing: Physics of complex melt flow and formation mechanisms of pores, spatter, and denudation zones. Acta Materialia, 108, 36–45.

65. Gordon, J., Narra, S., Cunningham, R., Liu, H., Chen, H., Suter, R., et al. (2020). Defect structure process maps for laser powder bed fusion additive manufacturing. Additive Manufacturing, 36, 101552. https://doi.org/10.1016/j.addma.2020.101552.

66. Leung, C. L. A., Marussi, S., Atwood, R. C., Towrie, M., Withers, P. J., & Lee, P. D. (2018). In situ X-ray imaging of defect and molten pool dynamics in laser additive manufacturing. Nature Communications, 9(1), 1–9. https://doi.org/10.1038/s41467-018-03734-7

67. Deng, P., Karadge, M., Rebak, R. B., Gupta, V. K., Prorok, B. C., & Lou, X. (2020). The origin and formation of oxygen inclusions in austenitic stainless steels manufactured by laser powder bed fusion. Additive Manufacturing, 35(December 2019), 101334.

68. Tan, J., Wong, W., Dalgarno, K. (2017). An overview of powder granulometry on feedstock and part performance in the selective laser melting process. Additive Manufacturing, 18, 228-255. https://doi.org/10.1016/j.addma.2017.10.011.

69. Martin, J. H., Yahata, B. D., Hundley, J. M., Mayer, J. A., Schaedler, T. A., & Pollock, T. M. (2017). 3D printing of high-strength aluminium alloys. Nature, 549(7672), 365–369.

70. Yan, F., Xiong, W., Faierson, E., & Olson, G. B. (2018). Characterization of nano-scale oxides in austenitic stainless steel processed by powder bed fusion. Scripta Materialia, 155, 104–108. https://doi.org/10.1016/J.SCRIPTAMAT.2018.06.011

71. Yin, Y. J., Sun, J. Q., Guo, J., Kan, X. F., & Yang, D. C. (2019). Mechanism of high yield strength and yield ratio of 316 L stainless steel by additive manufacturing. Materials Science and Engineering A, 744(November 2018), 773–777. https://doi.org/10.1016/j.msea.2018.12.092

72. Barkia, B., Aubry, P., Haghi-Ashtiani, P., Auger, T., Gosmain, L., Schuster, F. et al. (2020). On the origin of the high tensile strength and ductility of additively manufactured 316L stainless steel: Multiscale investigation. Journal of Materials Science & Technology, 41, 209-218. https://doi.org/10.1016/j.jmst.2019.09.017.

73. Byrnes, M. L. G., Grujicic, M., & Owen, W. S. (1987). Nitrogen Strengthening of a Stable. Acta Metall, 35(7), 1853–1862.

74. Simmons, J.W. (1996). Overview: high-nitrogen alloying of stainless steels. Materials Science and Engineering: A, 207, 159-169. https://doi.org/10.1016/0921-5093(95)09991-3.

75. Derimow, N., Romero, A., Rubio, A., Terrazas, C., Medina, F., Wicker, R., Hrabe, N. (2021). Sintered powder oxidation variation as a function of build height for titanium alloy produced by electron beam powder-bed fusion. Additive Manufacturing Letter, 1, 100023.

76. Boyce, B. L., Salzbrenner, B. C., Rodelas, J. M., Swiler, L. P., et al. (2017). Extreme-Value Statistics Reveal Rare Failure-Critical Defects in Additive Manufacturing. Advanced Engineering Materials, 19(8), 1700102.

77. Ma, K., Wen, H., Hu, T., Topping, T. D., Isheim, D., Seidman, D. N., Lavernia, E. J., & Schoenung, J. M. (2014). Mechanical behavior and strengthening mechanisms in ultrafine grain precipitation-strengthened aluminum alloy. Acta Materialia, 62(1), 141–155.

78. Voisin, T., Forien, J. B., Perron, A., Aubry, S., Bertin, N., Samanta, A., Baker, A., & Wang, Y. M. (2021). New insights on cellular structures strengthening mechanisms and thermal stability of an austenitic stainless steel fabricated by laser powder-bed-fusion. Acta Materialia, 203.

79. Schmauder, S., Kohler, C. (2011). Atomistic simulations of solid solution strengthening of α-iron. Computational Materials Science, 50, 1238–1243

80. Mohd Yusuf, S., Chen, Y., Yang, S., & Gao, N. (2020). Microstructural evolution and strengthening of selective laser melted 316L stainless steel processed by high-pressure torsion. Materials Characterization, 159(July), 110012. https://doi.org/10.1016/j.matchar.2019.110012

81. Luo, X., Lou, J., He, H., Wu, C., Huang, Y., Su, N., Li, S. (2023). Effects of Carbon Content on the Properties of Novel Nitrogen-Free Austenitic Stainless Steel with High Hardness Prepared via Metal Injection Molding. Metals, 13, 403. https://doi.org/ 10.3390/met13020403

82. Hu, Z. Y., Cheng, X. W., Zhang, Z. H., Wang, H., Li, S. L., Korznikova, G. F., Gunderov, D. V., & Wang, F. C. (2017). The influence of defect structures on the mechanical properties of Ti-6Al-4V alloys deformed by high-pressure torsion at ambient temperature. Materials Science and Engineering A, 684, 1–13. https://doi.org/10.1016/j.msea.2016.12.033

83. Li, S., Li, J.Y., Jiang, Z.W., Cheng, Y., Li, Y.Z., Tang, S., Leng, J.Z., et al. (2022). Controlling the columnar-to-equiaxed transition during Directed Energy Deposition of Inconel 625. Additive Manufacturing, 57, 102958. https://doi.org/10.1016/j.addma.2022.102958.

84. Ungár, T., & Borbély, A. (1996). The effect of dislocation contrast on x-ray line broadening: A new approach to line profile analysis. Applied Physics Letters, 69(21), 3173–3175. https://doi.org/10.1063/1.117951

85. Shamsujjoha, M.D., Agnew, S.R., Fitz-Gerald, J.M., Moore, W.R., Newman, T.A. (2018). Metallurgical & Materials Transactions A, 49, 3011-3027.

86. Eliasson, J., Sandström, R. (2000). Proof strength values for austenitic stainless steels at elevated temperatures. Steel Research International, 71, 249–254. https://doi.org/10.1002/ srin.200001224

CHAPTER 7   SUMMARY AND CONCLUSIONS

The objective of this study was to establish processing-properties-performance-structure relationships of three non-equilibrium processes (mechanical alloying, laser ablation, and laser melting) for various material systems, MoC-graphite composite, CoCr-based alloy, and 316L stainless steel. This work also aimed to develop further comprehensive knowledge to address the operational mechanisms and the effect of the process parameters for each technique. To accomplish this, each material was characterized thoroughly to unravel the process-structure relationships necessary to explain their formation mechanisms. The versatility of these processes was demonstrated by showing the control and optimization of materials properties such as composition, microstructure, phase transformations, and performance. Despite the complexity of these processes, it was also proved that they possess extraordinary processing flexibility to adjust to any material and production scale.

Based on the specific objectives of this work, the following section briefly summarizes the most important results achieved in each study.

MoC@C core-shell nanoparticles synthesized by laser ablation in liquid.

For laser ablation, the operational mechanism was described in terms of the steps responsible for producing MoC core and OLC shell structures. In this process, the high temperatures and pressures are responsible for taking the material out of equilibrium. As a result, a plasma plume is induced, which ionizes the solvent and generates C species (atoms, ions, clusters, etc.) that react with the Mo species. Several chemical reactions and nucleating of NPs occur during the adiabatic expansion of the plasma plume. During the plasma cooling down, the NPs are rapidly quenched; this means the material is returned to equilibrium. This allows all the carbon reacts to form the graphite coating, forming core/shell NPs in an amorphous carbon matrix.

Significant differences in the carbon structures were obtained when using short and ultra-short pulsed lasers. It was confirmed that the pulse duration affects the size distribution, morphology, and composition of the NPs. The thickness of the carbon coating was also affected. However, despite the laser source utilized, the number of OLC structures in both systems only represented some of the carbon structures formed. The reason behind this phenomenon was not addressed in this study. However, the presence of various carbon sources, H, OH molecules, and multistep ablation can affect the formation of OLC structures. It was confirmed that the ablation threshold was lower with short pulses as a thicker carbon matrix was observed. This means that more carbon was ablated, and therefore, more carbon was segregated.

Due to the simplicity of the methodology, this procedure could be applied to synthesize metal-graphite or carbides-graphite core-shell NPs of various metals to control their agglomeration and size distribution and possibly prevent their oxidation. This study could provide further insight into the purity of the NPs and the phase transformations due to the reheating of the NPs already synthesized. Further investigations are needed to evaluate the total irradiation time of the target to estimate the volume of material removed and the ablation quality.

Effect of processing, chemical composition, and annealing temperature on the mechanochemical synthesis of Mo$_x$C-graphite composite.

A family of Mo-C composites was successfully developed by mechanical alloying. The production parameters and the underlying physical mechanisms have been studied. When the MoC-graphite was synthesized by mechanical alloying, it was observed that ball milling was insufficient to obtain a homogeneous microstructure. However, by implementing annealing of the as-milled powders at low temperatures for 1 hour, the microstructure could be controlled to obtained the α-Mo$_2$C phase. During ball milling, the plastic deformation resulting from the repetitive fracture and cold welding brought the material out of equilibrium. As a result, the increment in defect density increased the grain boundary area, thus reducing the diffusion distances between C and Mo to form heterostructures of MoC and metastable phases. The subsequent annealing led to the decomposition of the metastable phases and brought the system back to equilibrium by stabilizing the α-Mo$_2$C phase. These steps can be summarized with the following steps:

1. Mo + C (graphite, coal, amorphous C) → mechanical activation → Mo$_x$C$_y$ (metastable compound)

2. Mo$_x$C$_y$ → annealing → Mo$_2$C + Polyaromatic carbon

Further characterization is necessary to confirm the exact composition of the excess carbon and its properties as a reinforcement. For example, TEM characterization is required to analyze the dispersion of carbon structures in the matrix. It has been proved in Chapter 3 and discussed in the background section that graphite tends to encapsulate the carbide and form a matrix of amorphous carbon. Therefore, similar results might be possible in this composite.

The most significant contribution of this study was to show a practical and simple methodology to synthesize a carbide that tends to be challenging and costly to produce by conventional methods. Although the properties of this material were not evaluated, this powder has the potential to be used for catalysis applications. This method produced a compatible size distribution for catalysis purposes, and it also has the option to synthesize more heterophase useful in this field, such as MoC/Mo$_2$C, δ-MoC, and MoC.

CoCr alloy processed by selective laser melting: comparison of atomized and milled powder feedstocks.

This study explored using as-milled powder as powder feedstock for SLM processes and implemented various custom-made and industrial laser equipment. All the experiments were compared with a commercial atomized CoCr alloy. The effects of continuous and pulsed lasers on the melting behavior were studied. Important laser-matter interactions were discussed, providing information about rapid solidification, thermalization effects, and phase transformations.

Various challenges were reported regarding the complications of developing SLM at a low scale (using ~100g of powder). Consequently, the femtosecond laser and the PBF-LB Pro-X DMP 200 were not successful in printing the parts. However, a DED custom-made set-up with a blue laser was developed to eliminate the technical problems. Due to the high energy of this laser, i.e., because of a smaller wavelength (450 nm), the milled and atomized powders were successfully melted. The samples obtained with this equipment were used to evaluate the feasibility of obtaining equiaxed grain growth from introducing SiC nanoparticles in the powder feedstock. We observed that when using as-milled powder, more equiaxed grains were obtained. This was possible not only because of the addition of the NPs but also due to the combination of the continuous re-heat and re-melt of each layer. These particles control the solidification microstructure by developing a larger constitutional supercooling zone ahead of the S/L interface, causing a high density of heterogeneous nucleation sites, which induces near equiaxed grain formation.

Further studies are needed to investigate the nucleation potency of the NPs and optimize the composition of the milled powder to obtain a homogeneous composition. Other compositions of NPs (other carbides and oxides) might be implemented to improve the lattice mismatch and increase the growth restriction and chemical stability. However, despite the challenges encountered, this study provided a foundation to improve the microstructure of CoCr alloys to avoid their columnar grain growth. This is advantageous as no literature articles have reported this alternative to avoid anisotropy and improve mechanical properties. Another significant contribution of this work was obtaining of the ε-Co HCP as the predominant phase. Compared to the FCC phase (most commonly reported as the principal phase for this alloy), the HCP phase has higher wear resistance, strength, and excellent ductility.

Elucidating the effect of powder reusability of 316L stainless steel on the as-printed parts for laser.

In-depth understanding of powder reuse studies reported in the literature, it can be confirmed that powder degradation mechanisms are not well understood. There are still no standardized powder reuse methods for the most used alloys in PBF-LB, and limited insight is available regarding the reused powder properties–part properties relationships. Based on these knowledge gaps, this study aimed to explore in

detail all the aspects of powder reusability, including the process, powder degradation, the evolution of the microstructure of the printed parts, and mechanical testing.

In this study, the mechanisms of powder degradation were discussed based on the laser-matter interaction properties. The powder group that suffers from more changes is the one in direct contact with the laser beam. This group is classified as spatter. The impact of these unwanted particles on the microstructure was provided by correlating their effect with factors that cause melt pool instabilities. Key aspects of the melt pool behavior were also linked to the defect formation.

It was observed that the as-printed parts did not present detrimental defects in their microstructure; thus, no early failures after tensile testing were reported. We found that changes in chemical composition may be one property in the powder that can lead to further fluctuations in the chemical composition of the printed parts. Such changes were observed by the increase in nano-oxide inclusions, carbon, and nitrogen content in the as-printed parts. We found that after 20 reuses, the yield strength and hardness of the printed parts increased. Due to these findings, strengthening mechanisms were studied to develop correlations between the microstructure and performance of the as-printed parts. It was found that grain boundary and dislocation strengthening were the predominant contributors to yield strength. A complete understanding of these mechanisms is highly challenging due to the complex microstructure of the 3D-printed parts. Therefore, this study indicated areas that need further development in this field to improve the accuracy of the calculation of the strengthening methods.

Despite multiple investigations in powder reuse, many unknowns exist in defining powder's end of life (EoL). This study did not provide quantitative data about this aspect. However, based on the reused powder's PSD, phase fraction, and microstructure, the powder might still be acceptable for printing purposes. Further testing, including fatigue, creep, anisotropy, and heat treatment studies, is required to obtain more substantial data related to the EoL of powder. It is important to highlight that these studies will depend on the laser technique, parameters, reuse methods, and dimensions of printed parts.

The copyright permissions to include Figures 2.2, 2.3, 2.4, 2.5, 2.7, 2.11, 3.3, 3.4, 3.6, and 3.7 can be found below.

1) Figure 2.2 is reprinted with permission from Springer Nature and Copyright Clearance Center, Inc. Laser Processing of Materials. Springer Series in Materials Science, "Fundamentals of Laser-Material Interactions", Carpene E, Höche D, Schaaf P, vol. 139, 2010. Used with the following permission from the publisher:

SPRINGER NATURE LICENSE
TERMS AND CONDITIONS

May 29, 2023

This Agreement between Colorado School of Mines -- Madelyn Madrigal Camacho ("You") and Springer Nature ("Springer Nature") consists of your license details and the terms and conditions provided by Springer Nature and Copyright Clearance Center.

License Number	5558290069119
License date	May 29, 2023
Licensed Content Publisher	Springer Nature
Licensed Content Publication	Springer eBook
Licensed Content Title	Fundamentals of Laser-Material Interactions
Licensed Content Author	Ettore Carpene, Daniel Höche, Peter Schaaf
Licensed Content Date	Jan 1, 2010
Type of Use	Thesis/Dissertation
Requestor type	academic/university or research institute
Format	electronic
Portion	figures/tables/illustrations
Number of figures/tables/illustrations	1
Will you be translating?	no
Circulation/distribution	1 - 29
Author of this Springer Nature content	no
Title	Chapter disseration: MoC@C core-shell nanoparticles synthesized by laser ablation in liquid

Institution name	Colorado School of Mines
Expected presentation date	Jun 2023
Portions	Fig. 3.1 page 26

	Colorado School of Mines
	1500 Illinois St
Requestor Location	
	GOLDEN, CO 80401
	United States
	Attn: Colorado School of Mines

Total	0.00 USD

Terms and Conditions

The Licensor grants you a personal, non-exclusive, non-transferable, non-sublicensable, revocable, world-wide License to reproduce, distribute, communicate to the public, make available, broadcast, electronically transmit or create derivative works using the Licensed Material for the purpose(s) specified in your RightsLink Licence Details only.

2) Figure 2.3 is reprinted with permission from Springer Nature and Copyright Clearance Center, Inc. Handbook of Nanoparticles. Springer, Cham, "Nanoparticles by Laser Ablation of Bulk Target Materials in Liquids", Semaltianos, N.G., 2016. Used with the following permission from the publisher:

SPRINGER NATURE LICENSE
TERMS AND CONDITIONS

May 29, 2023

This Agreement between Colorado School of Mines -- Madelyn Madrigal Camacho ("You") and Springer Nature ("Springer Nature") consists of your license details and the terms and conditions provided by Springer Nature and Copyright Clearance Center.

License Number	5558291071481
License date	May 29, 2023
Licensed Content Publisher	Springer Nature
Licensed Content Publication	Springer eBook
Licensed Content Title	Nanoparticles by Laser Ablation of Bulk Target Materials in Liquids
Licensed Content Author	N. G. Semaltianos
Licensed Content Date	Jan 1, 2016
Type of Use	Thesis/Dissertation

Requestor type	academic/university or research institute
Format	electronic
Portion	figures/tables/illustrations
Number of figures/tables/illustrations	1
Will you be translating?	no
Circulation/distribution	1 - 29
Author of this Springer Nature content	no
Title	Chapter disseration: MoC@C core-shell nanoparticles synthesized by laser ablation in liquid
Institution name	Colorado School of Mines
Expected presentation date	Jun 2023
Portions	Figure 3, page 71
Requestor Location	Colorado School of Mines 1500 Illinois St GOLDEN, CO 80401 United States Attn: Colorado School of Mines
Total	0.00 USD

Terms and Conditions

The Licensor grants you a personal, non-exclusive, non-transferable, non-sublicensable, revocable, world-wide License to reproduce, distribute, communicate to the public, make available, broadcast, electronically transmit or create derivative works using the Licensed Material for the purpose(s) specified in your RightsLink Licence Details only.

3) Figure 2.4 is reprinted with permission from Elsevier and Copyright Clearance Center, Inc. Journal of Materials Processing Technology, "Theoretical and experimental investigations of ultra-short pulse laser interaction on Ti6Al4V alloy", Kiran K, Samuel G.L, and Shunmugam M.S., vol. 263, 2019. Used with the following permission from the publisher:

ELSEVIER LICENSE
TERMS AND CONDITIONS

May 29, 2023

This Agreement between Colorado School of Mines -- Madelyn Madrigal Camacho ("You") and Elsevier ("Elsevier") consists of your license details and the terms and conditions provided by Elsevier and Copyright Clearance Center.

License Number	5558380528243
License date	May 29, 2023
Licensed Content Publisher	Elsevier
Licensed Content Publication	Journal of Materials Processing Technology
Licensed Content Title	Theoretical and experimental investigations of ultra-short pulse laser interaction on Ti6Al4V alloy
Licensed Content Author	K. Kiran Kumar,G.L. Samuel,M.S. Shunmugam
Licensed Content Date	Jan 1, 2019
Licensed Content Volume	263
Licensed Content Issue	n/a
Licensed Content Pages	10
Start Page	266
End Page	275
Type of Use	reuse in a thesis/dissertation
Portion	figures/tables/illustrations
Number of figures/tables/illustrations	1
Format	electronic
Are you the author of this Elsevier article?	No
Will you be translating?	No
Title	Dissertation chapter: 2.1.3.1. Laser melting mechanism using ultra-short pulse laser
Institution name	Colorado School of Mines
Expected presentation date	Jun 2023
Portions	Figure 1. Schematic diagram of Ultra-short pulse laser-matter interaction mechanism. Page 6
Requestor Location	Colorado School of Mines 1500 Illinois St GOLDEN, CO 80401

4) Figure 2.5 is reprinted with permission from Elsevier and Copyright Clearance Center, Inc. Journal
of Manufacturing Processes, "A comprehensive review on laser powder bed fusion of steels: Processing,
microstructure, defects and control methods, mechanical properties, current challenges, and future
trends", Narasimharaju S.R, Zeng W, See T.L, Zhu Z, Scott P, Jiang X, and Lou S, vol. 75, 2022. Used
with the following permission from the publisher:

5) Figure 2.7 is reprinted with permission from Springer Nature and Copyright Clearance Center, Inc.
Nature, "3D printing of high-strength aluminium alloys", Martin J, Yahata B, Hundley J, Yahata B.,
Hundley J, Mayer J, Schaedler T, and Pollock T, vol 549, 2017. Used with the following permission from
the publisher:

License Number	5558420938768
License date	May 29, 2023
Licensed Content Publisher	Springer Nature
Licensed Content Publication	Nature
Licensed Content Title	3D printing of high-strength aluminium alloys
Licensed Content Author	John H. Martin et al
Licensed Content Date	Sep 21, 2017
Type of Use	Thesis/Dissertation
Requestor type	academic/university or research institute
Format	electronic
Portion	figures/tables/illustrations
Number of figures/tables/illustrations	1
Would you like a high resolution image with your order?	no
Will you be translating?	no
Circulation/distribution	1 - 29
Author of this Springer Nature content	no
Title	Chapter Dissertation: Formation of finer-equiaxed grains during selective laser additive manufacturing
Institution name	Colorado School of Mines
Expected presentation date	Jun 2023
Portions	Figure 1. page 366
Requestor Location	Colorado School of Mines 1500 Illinois St GOLDEN, CO 80401 United States Attn: Colorado School of Mines
Total	0.00 USD

Terms and Conditions

The Licensor grants you a personal, non-exclusive, non-transferable, non-sublicensable, revocable, world-wide License to reproduce, distribute, communicate to the public, make available, broadcast, electronically transmit or create derivative works using the Licensed Material for the purpose(s) specified in your RightsLink Licence Details only.

6) Figure 2.11 is reprinted with permission from Elsevier and Copyright Clearance Center, Inc.

Additive Manufacturing, "Evolution of 316L stainless steel feedstock due to laser powder bed fusion

process", Heiden M.J, Deibler L.A, Rodelas J.M, Koepke J.R, Tung D.J, Saiz D.J, and Jared B.H, vol. 25,

2019. Used with the following permission from the publisher:

Number of figures/tables/illustrations	1
Format	electronic
Are you the author of this Elsevier article?	No
Will you be translating?	No
Title	Chapter Dissertation: Laser powder bed fusion of 316L stainless steel
Institution name	Colorado School of Mines
Expected presentation date	Jun 2023
Portions	Figure 23, page 102
Requestor Location	Colorado School of Mines 1500 Illinois St GOLDEN, CO 80401 United States Attn: Colorado School of Mines
Publisher Tax ID	98-0397604
Total	0.00 USD

Terms and Conditions

Elsevier hereby grants you permission to reproduce the aforementioned material subject to the terms and conditions indicated.

7) Figures 3.3, 3.6, and 3.7 are reprinted with permission from Elsevier and Copyright Clearance Center, Inc. Diamond and Related Materials, "Synthesis of MoC@Graphite NPs by short and ultra-short pulses laser ablation in toluene under N2 atmosphere", Madrigal-Camacho M, Vilchis-Nestor A.R, Camacho-López M, Camacho-López M.A, vol. 82, 2018. Used with the following permission from the publisher:

CCC | RightsLink

Synthesis of MoC@Graphite NPs by short and ultra-short pulses laser ablation in toluene under N2 atmosphere

Author: Madelyn Madrigal-Camacho,Alfredo Rafael Vilchis-Nestor,Marco Camacho-López,Miguel A. Camacho-López

Publication: Diamond and Related Materials

Publisher: Elsevier

Date: February 2018

Journal Author Rights

BACK

CLOSE WINDOW